LEABHARLANN CHOLÁISTE NA TRÍONÓIDE, BAILE ÁTHA CLIATH | TRINITY COLLEGE LIBRARY DUBLIN
Ollscoil Átha Cliath | The University of Dublin

Terms and Conditions of Use of Digitised Theses from Trinity College Library Dublin

Copyright statement

All material supplied by Trinity College Library is protected by copyright (under the Copyright and Related Rights Act, 2000 as amended) and other relevant Intellectual Property Rights. By accessing and using a Digitised Thesis from Trinity College Library you acknowledge that all Intellectual Property Rights in any Works supplied are the sole and exclusive property of the copyright and/or other IPR holder. Specific copyright holders may not be explicitly identified. Use of materials from other sources within a thesis should not be construed as a claim over them.

A non-exclusive, non-transferable licence is hereby granted to those using or reproducing, in whole or in part, the material for valid purposes, providing the copyright owners are acknowledged using the normal conventions. Where specific permission to use material is required, this is identified and such permission must be sought from the copyright holder or agency cited.

Liability statement

By using a Digitised Thesis, I accept that Trinity College Dublin bears no legal responsibility for the accuracy, legality or comprehensiveness of materials contained within the thesis, and that Trinity College Dublin accepts no liability for indirect, consequential, or incidental, damages or losses arising from use of the thesis for whatever reason. Information located in a thesis may be subject to specific use constraints, details of which may not be explicitly described. It is the responsibility of potential and actual users to be aware of such constraints and to abide by them. By making use of material from a digitised thesis, you accept these copyright and disclaimer provisions. Where it is brought to the attention of Trinity College Library that there may be a breach of copyright or other restraint, it is the policy to withdraw or take down access to a thesis while the issue is being resolved.

Access Agreement

By using a Digitised Thesis from Trinity College Library you are bound by the following Terms & Conditions. Please read them carefully.

I have read and I understand the following statement: All material supplied via a Digitised Thesis from Trinity College Library is protected by copyright and other intellectual property rights, and duplication or sale of all or part of any of a thesis is not permitted, except that material may be duplicated by you for your research use or for educational purposes in electronic or print form providing the copyright owners are acknowledged using the normal conventions. You must obtain permission for any other use. Electronic or print copies may not be offered, whether for sale or otherwise to anyone. This copy has been supplied on the understanding that it is copyright material and that no quotation from the thesis may be published without proper acknowledgement.

The Electromechanical Properties of Individual Nanowires

A thesis presented to the University of Dublin, Trinity College for the degree of

Doctor of Philosophy in Chemistry

2014

Eoin K. McCarthy

Under the supervision of Prof. John J. Boland

School of Chemistry & CRANN

Trinity College Dublin

Table of Contents

Acknowledgement i

Declaration ii

Permission to Lend and/or Copy iii

Summary iv

List of Abbreviations vi

Chapter 1: Introduction 1

1.1 Mechanical properties 3

1.1.1 Young's modulus; double clamped beam 8

1.1.2 Maximal Tensile Stress 10

1.2 Electrical Properties 10

1.3 Techniques to measure Nanoelectromechanical properties at the nanoscale 17

1.3.1 Zero- Dimensional (0D) electromechanical measurement nanoparticles 17

1.3.2 2- Dimensional (2D) electromechanical measurement – thin films 22

1.3.3 1- Dimensional (1D) electromechanical measurement – nanowires 27

1.3.3.1 EM based techniques 28

1.3.3.2 AFM based techniques 32

1.3.3.2.1 Piezoresponse Force Microscopy 32

1.3.3.2.2 AFM lateral bending 36

1.4 Conclusion 40

1.5 References 40

Chapter 2: Equipment and Methods 46

2.1. Electron microscopy 46

2.1.1. Scanning Electron Microscope 46

TRINITY COLLEGE
5 JAN 2015
LIBRARY DUBLIN

Thesis 10453

2.1.2. Transmission Electron Microscope (TEM) 50

2.2. Electron Beam Lithography (EBL) 54

2.3. Atomic Force Microscope 57

2.3.1. Working Principal 57

2.3.2. Scanners 59

2.3.3. Probes 60

2.4. Electromechanical 63

2.4.1. Mechanical measurement 63

2.4.1.1. Substrate processing for mechanical, electrical, and electromechanical measurements 64

2.4.1.2. NW placement and contacting protocol for electrical and electromechanical measurements 66

2.4.1.3. AFM calibration and operation for mechanical measurements on individual nanowires 68

2.4.2. Electrical measurement 73

2.4.3. Electromechanical measurement 75

2.5. Conclusion 77

2.6 References 77

Chapter 3: Mechanical and Electromechanical Properties of Germanium Nanowires 80

3.1 Motivation 80

3.2 Germanium nanowire synthesis and structure 86

3.3 Mechanical Properties of Germanium Nanowires (GeNW) 87

3.3.1 Experimental approach 87

3.3.2 Mechanical properties of GeNWs between 10-80 nm diameter using the lateral AFM 3-point bending technique 88

3.3.3 An improved TEM/AFM based mechanical characterisation technique 90

3.3.4 Uniaxial lateral-AFM measurement technique; Germanium nanowire "pulley system" 94

3.4 Electromechanical measurements on Germanium nanowires: Challenges with semiconducting nanowires 99

3.5 Conclusion 102

3.6 References 103

Chapter 4: The strain dependent Electrical Properties of Silver and Nickel Nanowires 105

4.1. Motivation 105

4.2. Nanowire Synthesis and Structure 108

4.2.1. Silver nanowire synthesis and structure 108

4.2.2. Nickel nanowire synthesis and structure 110

4.3. Results 112

4.3.1. Mechanical and Electrical properties of individual Ag NW 112

4.3.2. Mechanical and Electrical properties of individual Ni NW 113

4.3.3. Strain dependent resistance, Poisson's ratio and Gauge factor for AgNW and NiNW 118

4.4. Conclusion 128

4.5. References 128

Chapter 5: Current Induced Stiffening of Individual Silver Nanowires and Nickel Nanowires 132

5.1 Motivation 132

5.2 Current Induced Stiffening in Silver Nanowires 134

5.2.1 The dependence of Young's modulus on current load: Repeatedly loading a Silver nanowire at its centre point under a single current load. 134

5.2.2 The dependence of Young's modulus on increasing current density for individual AgNWs, comparing the result with NiNWs. 137

5.3 Conclusion 142

5.4 References 143

Chapter 6: Conclusion and Future Work 145

List of publications 149

Appendices 150

Acknowledgements

First and foremost, I would like to thank my supervisor Prof. John J. Boland for his guidance and support throughout, as well as SFI for funding my studies. I would also like to thank Prof. John E. Sader for assisting us throughout. I would especially like to thank John for his hilarious comments and anecdotes at many of our group meetings, I feel somewhat jealous of the new group members that will experience this after I depart.

I would like to take this opportunity to show my appreciation and eternal gratitude to the love and support from my parents, Breda and Kieran. Neither myself nor Joe would have accomplished a millionth of what we have without your support over the years. To my big bro Joe, your support and advice (.... and mental and physical torture!!) has been invaluable over the years. I especially appreciate the support from my wonderful girlfriend Sinead, I'm looking forward to our future together.

I couldn't have survived the past few years without the rowing fraternity. As a sport, it's kept me sane, and as for the bonds it forms between people, well only we know what that means. Thanks to the guys from DUBC and Neptune, especially Dave.

Thank you to all the group members, past and present, of the John Boland family especially Dorothee, Alan, David, Mary, Curtis, Allen, Ronan, Peter Nirmalraj and Peter Gleeson. Also thank you to those outside the Boland clan, especially our friends in the AML, who have made the PhD experience all the more enjoyable and productive.

Declaration

I, the undersigned, declare that this work has not previously been submitted as an exercise for a degree at this, or any other University, and that unless otherwise stated, is my own work.

28/02/2014 — Date

Eoin K. McCarthy — Eoin K. McCarthy

Permission to Lend and/or Copy

I, the undersigned, declare that this work has not previously been submitted as an exercise for a degree at this, or any other University, and that unless otherwise stated, is my own work.

28/02/2014
Date

Eoin K. McCarthy

DECLARATION

I declare that this thesis has not been submitted as an exercise for a degree at this or any other university and it is entirely my own work.

I agree to deposit this thesis in the University's open access institutional repository or allow the library to do so on my behalf, subject to Irish Copyright Legislation and Trinity College Library conditions of use and acknowledgement.

Signed: 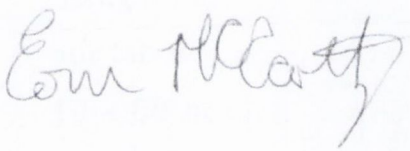

Summary

The measurement of the mechanical and electrical properties of individual nanowires and nanowire systems is of paramount importance for their future incorporation into functional devices. An equally important property that is not generally understood, due to the difficulty in its measurement, is the effect of a mechanical load on the electrical transport, namely the electromechanical effect, of individual nanowires. The methods used to measure the electromechanical properties of nanoscale systems are discussed with particular emphasis on one-dimensional materials.

Using a mechanical, atomic force microscope (AFM) based, technique developed in our lab we measured the mechanical properties of germanium nanowires between 10 – 80 *nm* in diameter finding the Young's modulus and strength to be 135 *GPa* and 17 *GPa* respectively, with increased scatter in the data for nanowires >22 *nm* in diameter. The scatter is due to imperfections in the nanowire crystal structure, such as twinned planes, and surface oxide thickness deviations, and resulted in the development of an improved transmission electron microscope (TEM)/AFM based technique to directly correlate crystal structure with mechanical performance. We describe the success and limitations of the TEM/AFM technique and introduce a uniaxial nanowire loading system, known as the "pulley system". The latter involves mechanical and electromechanical measurements and the limitations of this approach are discussed. These initial results and experiments on germanium nanowires led to the development of a new experimental procedure to measure the electromechanical properties of metallic nanowires.

This novel technique combining lateral atomic force microscopy, for mechanical measurement, and the four-point electrical technique, for accurate resistance measurement, has been developed to measure the strain dependent electrical properties and current dependent Young's modulus of silver and nickel nanowires. In this technique the nanowire of choice is placed across a trench and electrically contacted in a four-point geometry. Subsequently, the AFM tip laterally loads the

nanowire while the four-point resistance is measured as a function of the nanowire displacement. The resulting force-displacement curve and resistance-displacement curve allows the change in resistance as a function of strain to be studied, as well as, the change in Young's modulus as a function of current density. We have developed a generalised model to relate the change in resistivity and resistance in terms of the nanowire displacement, and used it to extrapolate fundamental mechanical and electromechanical parameters such as the Poisson's ratio and the gauge factor. We show the importance of measuring such parameters for individual nanowires as their values deviate substantially from the bulk value, an important result as the value of Poisson's ratio and the gauge factor for nanowires are generally assumed to be that of bulk.

We have discovered a surprising new phenomenon in which the Young's modulus of single crystal pentagonally twinned silver nanowires can be controlled by the amount of current passed through the nanowire. The Young's modulus was found to have a square dependence on the current density and was found to increase by greater than 100% at current density loads > 10^9 A/m^2. The results are compared to the same measurement on polycrystalline nickel nanowires in which no current induced stiffening was observed. Currently, these results are of great interest in terms of patenting opportunities as well as the ability to construct new multifunctional devices. Further computational and experimental analysis is required and will be addressed in future work.

List of Abbreviations

AFM	-	Atomic Force Microscope
C-AFM	-	Conductive Atomic Force Microscope
EM	-	Electron Microscopy
TEM	-	Transmission Electron Microscope
STEM	-	Scanning Transmission Electron Microscope
HRTEM	-	High Resolution Transmission Electron Microscope
SEM	-	Scanning Electron Microscope
NP	-	Nanoparticle
NW	-	Nanowire
GeNW	-	Germanium Nanowire
AgNW	-	Silver Nanowire
NiNW	-	Nickel Nanowire
CNT	-	Carbon Nanotube
SWCNT	-	Single Wall Carbon Nanotube
PDMS	-	Poly-Dimethyl-Siloxane
FIB	-	Focused Ion Beam
UV	-	Ultra Violet
EBL	-	Electron Beam Lithography
EBID	-	Electron Beam Induced Deposition
V_m	-	Measured Voltage
I_m	-	Measured Current
V_s	-	Source Voltage
Δz	-	Centre displacement
NEMS	-	Nano-Electromechanical Systems
MEMS	-	Micro-Electromechanical Systems

PFM	-	Piezo Force Microscopy
AC	-	Alternating Current
VLS	-	Vapour-Liquid-Solid
SCF	-	Super-Critical-Fluid
MBE	-	Molecular Beam Epitaxy
FEG	-	Field Emission Gun
BSE	-	Backscattered Electron
SE	-	Secondary Electron
VB	-	Valence Band
IV	-	Current-Voltage
PMMA	-	Poly-methyl-methacrylate
MMA	-	Methyl-methacrylate
HMDS	-	Hexamethyldisilzane
SPM	-	Scanning Probe Microscopy
STM	-	Scanning Tunnelling Microscope
PD	-	Photo-Detector
RIE	-	Reactive Ion Etching
IPA	-	Isopropanol
AAO	-	Anodised Aluminium Oxide
MIBK	-	Methyl Isobutyl Ketone
FFT	-	Fast Fourier Transform
PVP	-	Poly-Vinyl-Pyrrolidone
DFT	-	Density Function Theory

Chapter 1: Introduction

"I would like to describe a field, in which little has been done, but in which an enormous amount can be done in principle. [...] it would have an enormous number of technical applications. What I want to talk about is the problem of manipulating and controlling things on the small scale" Richard P. Feynman, 1959[1].

At the 1959 meeting of the American Physical Society, Richard Feynman challenged the scientific community to look beyond the apparent limits and to drive toward manipulating and controlling nature on a small scale, the nanoscale. Many of the challenges and questions raised by Feynman are at the forefront of technological research today. Moore's law predicts a decrease in feature size of ~0.7 every 3 years, which doubles the numbers of transistors on a chip every ~2 years[2]. With increased transistor performance computing power essentially doubles every 18 months. However there is a physical limit to Moore's law. In fact, we've already seen a slowdown in Moore's law and, indeed, some theoreticians have predicted the complete breakdown of Moore's law within the next 10 years. The international Technology Roadmap for Semiconductors (ITRS) 2009[3] report highlights the difficulty of going beyond the 22 *nm* node. However with improved device architecture silicon technology is being pushed to maintain Moore's law.

As well as a concerted drive to "more Moore" i.e. the continued miniaturisation of the metal-oxide-semiconductor-field-effect-transistor (MOSFET), research emphasises have diversified to devices that may give us more flexibility in terms of scaling. This area has been coined "more than Moore" (MtM). Figure 1 shows the dual trend in pushing Moore's law and MtM technology. MtM was first discussed in the ITRS report 2005[4] and has since become more significant, with the 2012 report highlighting the importance of including MtM technologies on the mainstream roadmap[5].

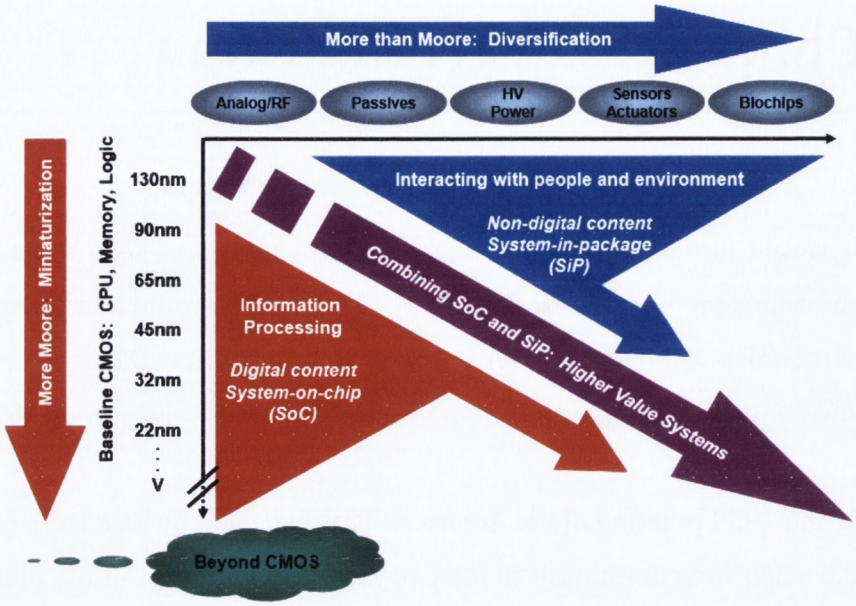

Figure 1: Moore's Law and more[7]

In the long term, top down wafer fabricated silicon MOSFETS are unlikely to meet the ITRS requirements. Bottom-up techniques are more likely to achieve these goals. Metallic and semiconducting (SC) nanowires are prime candidates for these building blocks, with planar devices moving towards nanowire devices, with "gate-all-round" configurations. Nanowires exhibit interesting electronic and mechanical properties making them an attractive option for transistors, interconnects, actuators and Nanoelectromechanical systems (NEMS). NEMS are envisaged to play an important role in future electronics[6]. They are dynamic devices where one, or more, components are electrostatically or physically strained to bend toward a target electrode through which the device can be turned on, or off. Hence, it is important to understand how electrical and mechanical properties depend on each other in nanoscale materials, namely the electromechanical effect.

In this thesis we focus on the electromechanical properties of Germanium, silver and nickel nanowires. We have developed an AFM based technique to measure the electromechanical properties of nanowires as small as 20 *nm* is diameter. This technique uses an Atomic Force Microscope (AFM) tip to laterally load the nanowire[7] while a home built 4-point electrical probe station, built around the AFM, measures the electrical properties. In addition, a generalised model was developed to extract the resistance and possible resistivity changes as a function of lateral strain. Also,

the generalised model allowed us to extrapolate Poisson's ratio for individual nanowires, a challenging property to measure, which has to this point, generally been assumed to be equal to the bulk value for nanoscale systems. Estimates of the Young's modulus and the ultimate strength were extracted by a previously reported model[8].

Here, in chapter 1 we present a general introduction to mechanical and electrical properties. We then present an extensive literature review on techniques to measure the electromechanical properties of 0D, 2D and 1D nano-materials. In chapter 2 we describe the equipment and methods used throughout this work, including a description of the mechanical and electromechanical approach. In chapter 3 the results and limitations of the measurement for the mechanical and electromechanical properties of germanium nanowires are presented. In chapter 4 we present the strain dependent resistance and resistivity of silver nanowires, directly comparing the result to another metallic system, nickel nanowires. In chapter 5 we show the current density dependant elasticity in silver nanowires, comparing the results with nickel nanowires. The thesis is concluded and final remarks are presented in chapter 6.

1.1 Mechanical properties

To incorporate nanomaterials into functional devices we need to fully understand the materials characteristics. This includes thermal, optical, electrical, mechanical and electromechanical properties. The most common method to probe mechanical properties is through tensile testing, which allows us to study both elastic properties and plastic deformation.

The fundamental parameters that describe the mechanical properties of a material are: stress, strain and strength [9].

- Stress is the ratio of the applied load divided by the initial cross sectional area.
- Strain is the ratio of the change in length over the initial length.
- Strength is a property of a material that enables it to resist deformation on an applied load. Materials strength has three definitions;

- Yield strength - stress level related to the onset of irreversible plastic deformation.
- Ultimate tensile strength - maximum load divided by the initial cross sectional area.
- True fracture strength - load at fracture divided by final actual cross sectional area *A*.

Materials can be deformed and fractured in different ways. Deformation can be elastic or plastic in nature. The former being the ability of the material to relax to its original state upon unloading of the given stress, and the latter being the permanent deformation of the material without fracture. Fracture may occur by brittle or ductile failure. Brittle failure occurs when the material fails before any plastic deformation occurs, ductile failure occurs whenever the material has the ability to become significantly deformed before failure [9].

The degree to which a structure deforms, or strains, depends on the magnitude of the applied stress [10]. If the response is completely elastic it is described by Hooke's law, equation (1);

$$\sigma = E\varepsilon \qquad (1)$$

Where σ is the applied stress, ε is the induced strain and E is the proportionality constant, known as Young's modulus. Young's modulus may be thought of as a materials stiffness or resistance to elastic deformation. On an atomic scale, macroscopic elastic strain manifests itself as small changes in the interatomic spacing by the stretching or compression of bonds. Consequently, the magnitude of Young's modulus is a measure of the resistance to separation of adjacent atoms i.e. interatomic bonding forces.

This view of material deformation is quite simplistic. It is important to note that stress in one direction causes strain in the two orthogonal directions, see figure 2.

The shear modulus, G, accounts for this;

$$\tau_{xz} = G\gamma_{xz} \qquad (2)$$

where τ_{xz} is the stress applied on the *x*-plane in the *z*-direction and γ_{xz} is the corresponding shear strain. Poisson's ratio, ν, is an important elastic constant that accounts for the anisotropic nature of mechanical deformation. It gives a measure of how much the material is deformed orthogonal to the applied stress. It is defined as;

$$\nu = -\frac{\varepsilon_{xx}}{\varepsilon_{yy}} \tag{3}$$

For isotropic materials, there is a simple relationship between *E*, *G* and ν; $E=2G(1+\nu)$[10]. It is important to note that crystallographic materials display different moduli depending on the crystal orientation [11].

Figure 2: Two dimensional representation of an applied force to the long axis causing contraction in the orthogonal plane. The ratio of axial extension to orthogonal contraction is known as Poisson's ratio

Measuring mechanical properties in the bulk is relatively straight forward [12], however, measuring one-dimensional systems on the nanoscale is decidedly more difficult due to their small size, usually less than 100 nm. This has been overcome using two techniques; *in-situ* Electron Microscopy (EM) and Atomic Force Microscopy (AFM). EM based mechanical measurements were pioneered in the mid-90s by Treacy *et al*[13]. In this work individual CNTs were thermally oscillated whilst measuring the amplitude using a TEM, with mechanical properties of the CNT extracted as a function of temperature[13]. This was later extended to tensile testing by Yu *et al*[14] in 2000. EM methods are two-fold; 1. Thermal and voltage induced nanowire oscillations, figure 3 (a, b); and 2. *in-situ* tensile measurements, figure 3 (c, d) [15, 16].

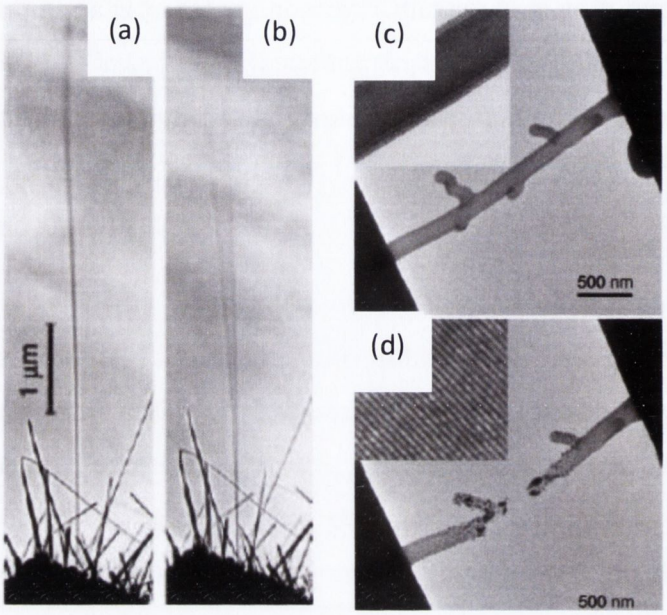

Figure 3: (a, b) EM measurement of Young's modulus using voltage vibration of carbon nanotubes[15]. The vibrational frequency was measured by the CNT displacement from its centre point using TEM. (c, d) Tensile measurement of MWCNT in a TEM[16]. The MWCNT was clamped at either side of two shuttles. The mechanical properties were measured by tensile deformation until fracture.

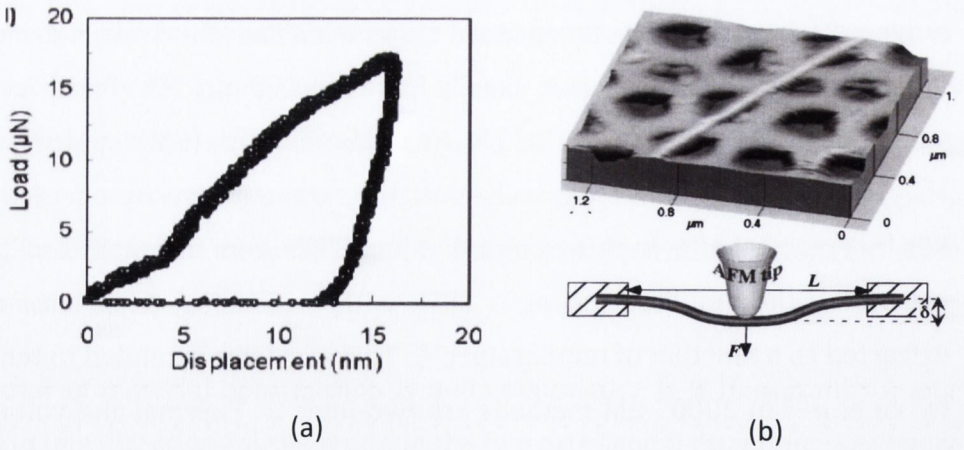

(a) (b)

Figure 4: (a) Typical F-d curve for an Ag NW under nanoindentation type load[17] (b) AFM image of SWCNT rope lying across pores and three point bend test schematic[18]. The rope was vertically loaded in a nanoindentation type technique. The 3-point bending is a result of the surface adhesion outside the pore acting to clamp the rope in place, avoiding slip events.

Table 1: The advantages and disadvantages of electron microscopy (EM) and atomic force microscope (AFM) based mechanical measurements.

	Advantages	***Disadvantages***
EM methods	- Atomic resolution imaging. - High-speed image acquisition. - Crystallographic information through diffraction. - Real time atomic resolution imaging during the deformation process.	- Currently limited to nanostructures >100 *nm* in diameter. - Tensile deformation only. - Electron beam irradiation/damage to the specimen. - Low sample throughput. - Extremely expensive and cumbersome equipment. - Extremely complex specimen preparation.
AFM methods		
- ***Nanoindentation***	- Extremely accurate (*pN*) mechanical sensitivity - Accurate spatial and depth resolution. - High sample throughput. - Ability to measure thin films, nanoparticles and nanowires <20 *nm* in diameter. - No damage to the specimen during imaging. - Limited interaction with specimen during sample preparation.	- Lateral tip slippage during force measurement. - Support substrate contributions. - Tip calibration required. - Slow image acquisition times. - Unable to visualise specimen deformation in real time.
- ***Lateral***	- Extremely accurate (*pN*) mechanical sensitivity. - Superior control over the tip-sample interaction volume. - High sample throughput. - The ability to measure nanowires <20 *nm* in diameter. - No damage to the specimen during imaging. - Limited interaction with specimen during sample preparation.	- Complex substrate fabrication required. - Cumbersome tip calibration required. - Slow image acquisition times. - Unable to visualise specimen deformation in real time.

EM mechanical methods are limited by the dimensions of the specimen that can be accurately measured, usually not less than 100 *nm*. *AFM* based techniques have less stringent limits on the specimen dimensions that can be accurately measured, mainly due to the sample preparation procedure. There are two basic types of *AFM* based mechanical measurements; nanoindentation and bending techniques. Nanoindentation is where a tip of a specific geometry is driven into the surface and resultant force displacement (f-d) curve is recorded. The advantage of using the *AFM* is that both imaging and measurement of the materials properties can be carried out by a single tool. In 2003, Li *et al* demonstrated this technique using silver nanowire (Ag NW) [17], figure 4 (a). Bending or tensile measurements can be vertical or lateral in nature. Vertical measurements were shown by Salvetat *et al* in 1999 [18]. This consisted of a three point bending measurement using SWCNT rope, figure 4 (b). Table 1 outlines the advantages and disadvantages of *EM* and *AFM* based mechanical measurements.

In 2005, Wu *et al* developed a technique by which an *AFM* tip laterally manipulates a single NW spanning over a trench [7]. This technique was used throughout this thesis and is discussed in greater detail later. In the next section the model to extrapolate the mechanical properties from lateral-beam-bending using AFM is described.

1.1.1 Young's modulus; double clamped beam

The Young's modulus (E) is a measure of the stiffness of a material; it is the ratio of stress over strain. Experimentally, to obtain E, the curve resulting from applied load versus displacement, known as the force-displacement curve, is fit to the following equation for a double clamped beam:

$$F_{center} = \frac{192EI}{L^3} \Delta z_{center} \qquad (4)$$

where F_{center} is the load applied to the centre of the beam, Δz_{center} the resulting displacement at the load point, E is the Young's modulus, I is the moment of inertia and L is the length of the beam [8].

Importantly, this equation predicts a linear relationship between the applied load and the resulting displacement and thus requires that the measured force-

displacement curve also exhibit this property. This approach is only valid for small deflections corresponding to bending of the beam. However, as the beam is displaced beyond bending, an in-plane tensile force is inherently induced due to the stretching of the beam. This force affects the total stress experienced by the beam, leading to an enhancement of its rigidity. An additional parameter, *f(α)*, which is a function of the wire dimensions, must be included to account for this effect, equation 5.

$$F_{center} = \frac{192EI}{L^3} f(\alpha) \Delta z_{center} \qquad (5)$$

where,

$$f(\alpha) = \frac{\alpha}{48 - \dfrac{192 \tanh(\sqrt{\alpha}/4)}{\sqrt{\alpha}}}$$

The α term is given by;

$$\alpha = \frac{6\varepsilon(140+\varepsilon)}{350+3\varepsilon}, \quad \left[\varepsilon = \Delta z_{center}^2 \left(\frac{A}{I}\right)\right]$$

Effectively at large deformations (i.e. deformation greater than one radius) the *f(α)* term transforms equation (5) into the form;

$$F = \frac{192EI}{L^3} \Delta z_{center} \left(1 + \frac{A}{24I} \Delta z_{center}^2\right)$$

This equation accounts for both linear bending components and cubic tensile components. The addition of the *f(α)* term is extremely important as it describes the non-linear force-displacement behavior observed in single nanowire mechanics. Equation (5) describes how the force-displacement data and the NW dimensions can give an estimate of the Young's modulus, *E*. The maximal tensile stress is also important in order to study the ultimate strength of the NW.

1.1.2 Maximal Tensile Stress

The maximum tensile stress in the linear displacement region due to bending only is given by

$$\sigma_{\max}^{(0)} = \frac{F_{center} Lc}{8I} \tag{6}$$

where F_{center} is the load applied to the center of the beam, c is the distance from the surface to the neutral axis of the beam (typically half the diameter), L is the beam length and I is the areal moment of inertia. This formula implicitly assumes that only bending is present. Again, for the same reasons as discussed above, there is an additional parameter, $g(\alpha)$, that must be incorporated into equation (6) in order to account for tension induced stretching.

$$\sigma_{\max} = \frac{F_{center} Lc}{8I} g(\alpha) \tag{7}$$

The full mathematical derivation for the extrapolation of E can be found in the appendix.

1.2 Electrical Properties

In material science, electrical properties play an important role. Before a material can be implemented into a functional device it is essential that the electrical properties are well understood. Some properties are intrinsic to the material, while others depend on how the material is treated. For example, semiconducting materials can be doped with foreign atoms to alter the materials resistivity. Straining a material can also be used to produce desired enhancements in the electrical characteristics, a practice that is commonly used in transistor fabrication[19]. The most common method for electrical characterisation is current-voltage (IV) analyses. Generally, this involves sweeping the voltage and measuring the current, or vice versa. IV characterisation provides a wealth of information, such as; Resistance (R), resistivity (ρ), current density (j) and conductivity (σ). These four parameters fundamentally characterise a material in a particular state under particular conditions. In addition, more advanced information can be gathered from IV characterisation such as doping profiles[20].

Electrical current is the amount of charge that passes through a given area per unit time[21] given by,

$$I = \frac{dQ}{dt} \tag{8}$$

where I is current, Q is charge and t is time, hence the units are coulomb/second (C/s) or Amperes (A). Materials can be divided into four categories depending on how easily charge flows through them;

- Conductors: where charge easily flows through the material, hence the material has a low resistance to current flow. Metals are a good example of conductors.
- Insulators: where charge does not flow easily through a material. Hence they have a very high resistance. Most polymers are insulators.
- Semiconductors: have intermediate characteristics between a conductor and insulator. Silicon and Germanium are semiconducting materials. This type of material is interesting because their conductivity can be altered by doping.
- Superconductors: have no resistance under certain conditions, in particular extremely low temperatures. In this type of material the resistance is zero in the superconductive state.

Material electrical properties are governed by electronic structure, known as band structure, figure 5. The curvature of the conduction and valence bands control the mobility characteristics of an electron residing in that state, depending on which band the electron resides in. The valence band (VB) describes the energy states by which the electrons are bound. The VB is typically filled with the majority of electrons used for bonding. Conversely, electrons in the conduction band have a higher energy and are not strongly bound to the atom allowing them to move under an external bias. The highest occupied energy level is denoted the 'Fermi level'. Figure 5 shows a schematic of the band structure for metals, semiconductors and insulators. In a metal, the conduction and valence bands overlap meaning the Fermi level is within the conduction band, hence, electrons can easily move through a metal. Therefore, metals are good conductors. In a semiconductor the conduction

and valence bands are separated by a small gap (0.14 – 4 *eV*), known as the bandgap. The Fermi level lies within the gap. The gap means electrons cannot easily move to the conduction band. However, electrons can hop to the conduction band if they gain enough energy, be it thermal or electrostatic. Insulators have a large bandgap (>5 *eV*) with the Fermi level situated in the gap. Insulators do not conduct charge as the charge carriers cannot gain enough energy to move from the valence to conduction band.

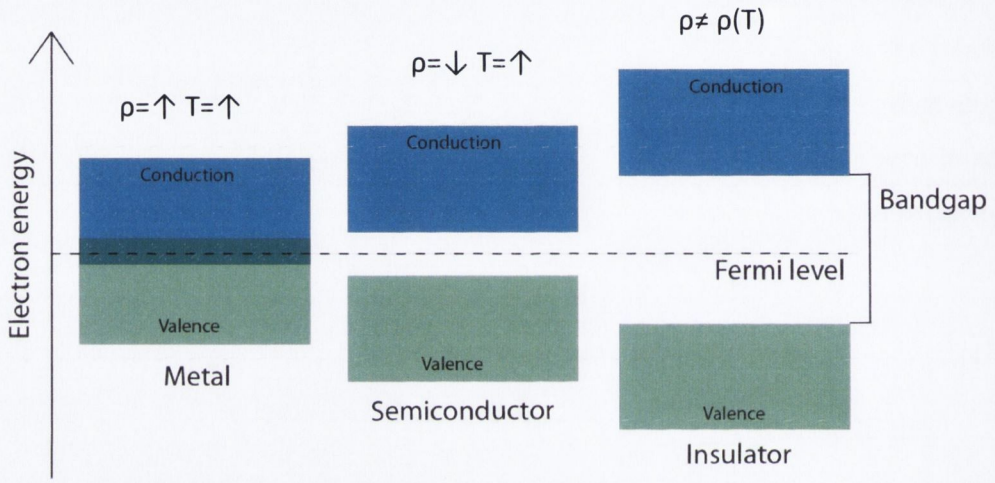

Figure 5: Schematic diagram of band structure and Fermi level in metals, semiconductors and insulators

A current flows when an electric field is applied to a conductor. The amount of current that flows through a material for a given potential difference across that material depends on the materials properties and geometry. The electrical resistance, *R*, is a measure of how easily charge flows within a material. Resistance is given by Ohms law;

$$R = \frac{V}{I} \tag{9}$$

Where *V* is the applied voltage and *I* is the current. The units are Volts/Ampere or the Ohm (Ω). Ohms law predicts a linear relationship between Voltage and Current, which is generally the case in metals. However, it is important to note that Ohms law is actually an empirical observation as many materials (semiconductors for example) do not obey Ohms law and show non-linear IV behaviour. Figure 6 is a schematic of an Ohmic, (a), and non-Ohmic, (b), device.

Resistance varies with dimensions and geometry of the specimen, therefore it is important to account for this in electrical measurements. For example, if resistance results from charge carrier collisions with atoms in the lattice, then doubling the length of that material will double the number of collisions, hence increasing the resistance. Thus, the resistance is proportional to length. The same can also be said for the cross sectional area. This geometry dependence is accounted for in the resistivity, ρ. Resistivity is given by;

$$\rho = R\frac{A}{L} \qquad (10)$$

where R is resistance, A is the cross sectional area and L is the length. ρ does not depend on the dimensions of the material, allowing materials of all dimensions and types to be compared under a normalised condition. Table 2 displays typical resistivity values found for conductors, semiconductors and insulators[22].

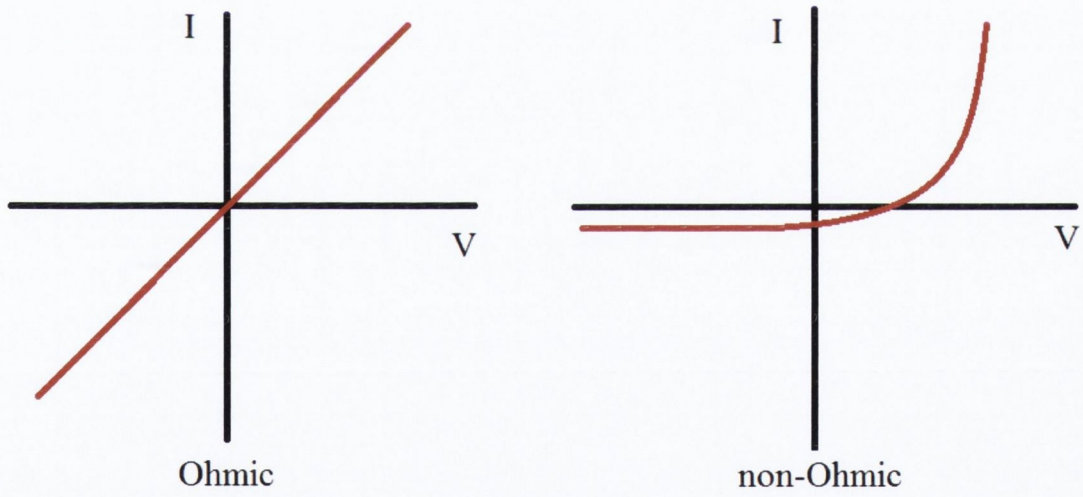

Figure 6: IV characteristics (a) ohmic and (b) non-linear non-ohmic behaviour

Table 2: Example resistivity values for conductors, semiconductors and insulators

Material	***Resistivity (Ω m)***
Conductors	
Aluminium	2.82×10^{-8}
Silver	1.59×10^{-8}
Copper	1.72×10^{-8}

Semiconductors	
Germanium (pure)	0. 46
Silicon (pure)	640
Insulators	
Glass	10^{10} - 10^{14}
Teflon	10^{14}

Conductivity, σ, is defined as the reciprocal of resistivity;

$$\sigma = \frac{1}{\rho} \tag{11}$$

Current density, *j*, is the rate of charge flow per unit area. It is a useful quantity because it allows us to calculate the electric field, E_{field}, where $j = E_{field}/\rho$. Current density is given by;

$$j = \frac{I}{A} = \frac{V}{L\rho} = \frac{E_{field}}{\rho} \tag{12}$$

where *I* is the current and *A* is the cross sectional area as before. Another important quantity to consider is how much power a device uses. Power, *P*, is given by the rate at which energy is expended by the force that pushes the charge i. e. the work done per unit time;

$$P = \frac{dW}{dt} = V\frac{dq}{dt} \tag{13}$$

where *W* is the work done, *t* is time and *q* is charge. But *dq/dt* is also the current *I*.

Therefore;

$$P = VI \tag{14}$$

It can also be seen that $P = VI = (IR)I = I^2R$. Either equation can be applied depending on what is known about the material. $P = I^2R$ is generally used for resistive materials, that do not display ohmic *IV* behaviour.

In terms of nanostructures there are generally two methods used to measure electrical properties; 2-point and 4-point measurement (also known as the Kelvin measurement). In the former case, there are only two connection leads probing and measuring the device i.e. voltage is sourced and current is measured across the same two leads, introducing significant errors in the observed resistance. The error is due to contact resistance between the electrical leads and the nanostructure, which can often be orders of magnitude greater than the resistance of the specimen itself. The latter, however, gives a true reading of the specimen resistance. This is achieved by sourcing the voltage and measuring the current across two leads and independently measuring the voltage drop across the sample with two separate leads and a voltmeter. As the voltmeter is a high impedance device minimal current flows through it, hence contact resistance is eliminated through the measurement technique. Figure 7 shows a schematic of a 4-point electrical measurement. The current remains constant across the circuit because it is a series loop. Voltage drop across the subject is measured using an independent voltmeter.

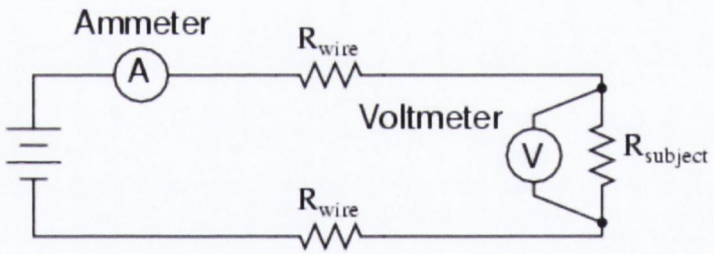

Figure 7: Schematic circuit of 4-point Kelvin measurement

Measuring electrical properties at the nanoscale is not trivial. This process involves multiple fabrication steps involved to make the sample and construct probes that contact the specimen. The measurement itself is also non-trivial as sample orientation and probing materials (materials the contact leads are made of) become more and more important. Niemann[23] described the general considerations for nanoscale electrical measurement;

1. Nanoscale materials will not support the magnitude of currents that a macroscopic device can carry (unless they are super-conducting). This means that, when a device is interrogated, the magnitude of a current stimulus must be carefully controlled.

2. Nanoscale materials will not hold off as much voltage from adjacent devices as a conventional electronic component or material. This is due to the fact that smaller devices can and are placed closer together. Smaller devices have less mass, and they may be affected by the forces associated with large fields. In addition, internal electric fields associated with nanoscale objects can be very high, requiring careful attention to applied voltages.
3. Since nanodevices are small, they typically have lower parasitic inductance and capacitance. This is especially useful when they are used in an electronic circuit, enabling faster switching speeds and lower power consumption than comparable macroscopic devices. However, this also means that instrumentation for characterizing their I-V curves must measure low currents while tracking the short reaction time.

Mechanical and electrical properties are fundamental properties of all materials. Nanoscale mechanical and electrical properties have been widely studied in the literature and are still topics of intense interest. A massive area of research has focused on nanowires for their potential application as fundamental building blocks of future electronics. There remains an extremely important material property, the nanoelectromechanical effect, that has not been widely studied primarily due to the difficulty in the measurement. This involves measuring the change in transport as a function of applied strain on individual nanoentities, and, the change in mechanical properties as a function of current load. Nanoelectromechanical properties of nanowires is an important area of research as both mechanical and electrical properties change at the nanoscale, due to increased surface atom to bulk ratio. The next section outlines the methods and techniques to measure nanoelectromechanical properties of nanoparticle (0D), thin films (2D) and nanowires (1D). Nanowires are the focus of this thesis and will be discussed in greatest detail.

1.3 *Techniques to measure Nanoelectromechanical properties at the nanoscale*

1.3.1 *Zero- Dimensional (0D) electromechanical measurement - nanoparticles*

Nanoparticles and nanospheres are of particular interest in areas such as fluidics[24], catalysis[25], synthesis[26], polymer composites[27] and sensors[28]. Nanoparticles are said to be 0-D in nature because they exhibit electron confinement in all 3-dimensions. Their small contained volume makes them an attractive system for strain and electrical measurements. In addition, the small number of atoms allows for very accurate modelling enabling an accurate description of the real system. Comparison of simulation and experiment can lead to improvements in both. Nanoparticles are difficult materials to characterise and hence there are few publications on techniques to measure their electromechanical properties.

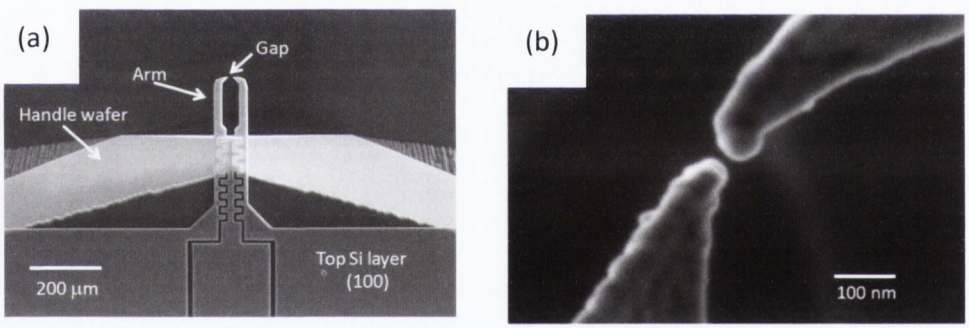

Figure 8: Free standing nanogap (a) overview of the nanogap device. The top Si layer is electrically isolated from the handle wafer by buried oxide (b) close up image of a ~17 nm *nanagap*[29].

In 2011, Han *et al*[29] reported on an electromechanical zero-dimensional freestanding nanogap actuator. Using a combination of optical lithography and wet etching the authors were able to fabricate a zero-dimensional actuator. The device consists of two arms with nanoscale sharp tips and an electrostatic or piezoelectric actuator. Figure 8 (a) shows a SEM image of the device. The nanogap can be opened and closed by a piezo actuator or electro-statically. Gap sizes fabricated were as small as 17 *nm* wide with smaller gaps achieved using actuation, figure 8 (b). The actuators were fabricated on Silicon-On-Insulator (SOI) substrates to isolate the device from handling. The entire device was also metallised to allow for electrical and optical measurements. The authors did not discuss mechanical or electromechanical

measurements, however the actuator has the ability to measure mechanical properties through the resonant frequency of the arms[29]. Although there has been a lack of published results on the electromechanical properties of NPs such a device shows the potential to measure the electromechanical properties of 0D objects. Currently, the field is dominated by NP film publications, mainly due to the difficulty in measuring a single NP. The following paragraphs discuss the latest attempts to probe the electromechanical properties of NP conglomerates.

In 2013, Moreira *et al*[30] studied electron transport in gold colloidal nanoparticles (Au NP) based strain gauges. In this paper, 14 *nm* Au NP coated in various surfactant molecules were assembled in a wire like geometry using convective self-assembly (CSA) and the resistance change with strain measured from 0% to 1% strain. Figure 9 (a) shows a schematic of multiple NP wires on a flexible substrate. The electrical characterisation technique is also indicated.

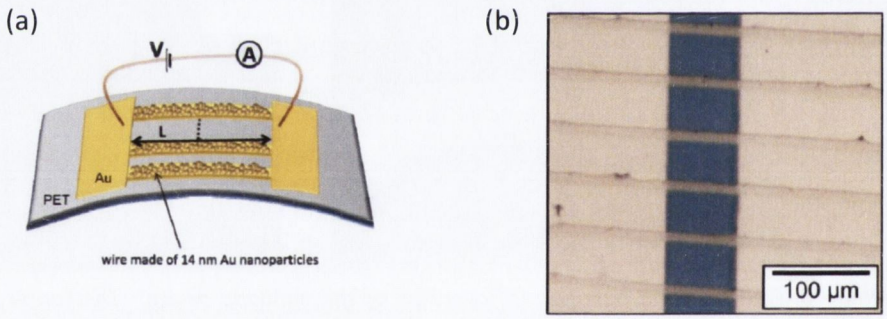

Figure 9: (a) schematic of a NP-based strain gauge and (b) Optical image of the active area of the strain guage consisting of 14 nm *Gold nanoparticles*[30].

Figure 9 (b) shows multiple Au NP wires fabricated in parallel on a Polyethylene Terephthalate (PET) flexible substrate. The performance of the nanoparticle based strain gauges were evaluated by monitoring the variation of their electrical resistance during bending of the flexible substrate at a constant source voltage of 0.5 *V*. The sensors were strained by bending them over the surface of cylindrical tubes of different diameters. The strain induced on the NP wires was determined by the relation $\varepsilon = \pm((e/d \pm e))$, where ε is the applied strain, *d* the tube diameter and *e* the substrate thickness. Figure 10 shows the effective resistance change with applied strain. Resistance changes of up to 38% were observed at 0.8% strain. A linear trend

between strain and resistance change was observed. Wire resistance was found to increase under tensile deformation and decrease under compression. The exact mechanism for an increase or decrease in resistance was not elucidated, although it is likely due to strain on the surfactant molecules altering the hoping distance and not strain on the Au NP themselves. A temperature dependent study would resolve this mechanism. However, the authors did tackle the issue of differing local strain effects between nanoparticles and the macro strain applied to the PET substrate. Although local strain effects were not accounted for their experimental results agreed with theoretical calculations [31].

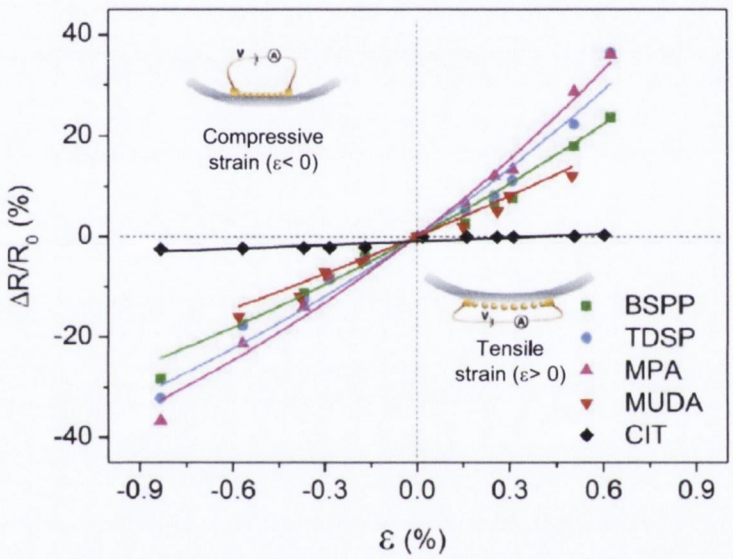

Figure 10: Relative resistance change, ΔR/R, as a function of strain, ε[29].

Rather importantly resistivity or resistance change was not discussed in detail. This is mainly due to difficulty in establishing the cross sectional area of the NP wire. Gold nanoparticle strain gauges have been reported elsewhere with resistance changes of up to 105% at 0.5% strain[32] and 50% resistance increase at 0.3% strain, due to NP-NP distance change increasing the tunnelling length[33]. Yin *et al*[34] also reported on Au NP thin film strain gauges finding up to 200% increases in resistance.

Another interesting system measured by an AFM/DNA tweezers technique shown by Hosogi *et al* [35] in 2007, was the electromechanical measurement of lambda DNA wires coated with palladium nanoparticles (Pd NP). In this paper the authors measured the conductivity of Pd NP coated DNA wires using a micromachined tweezers. In their experiment, an AFM was configured to electrical measurement of

bridged nanowires between the tweezers probes. A special knife-wedge shaped AFM tip was utilised to apply the loading force to the wire.

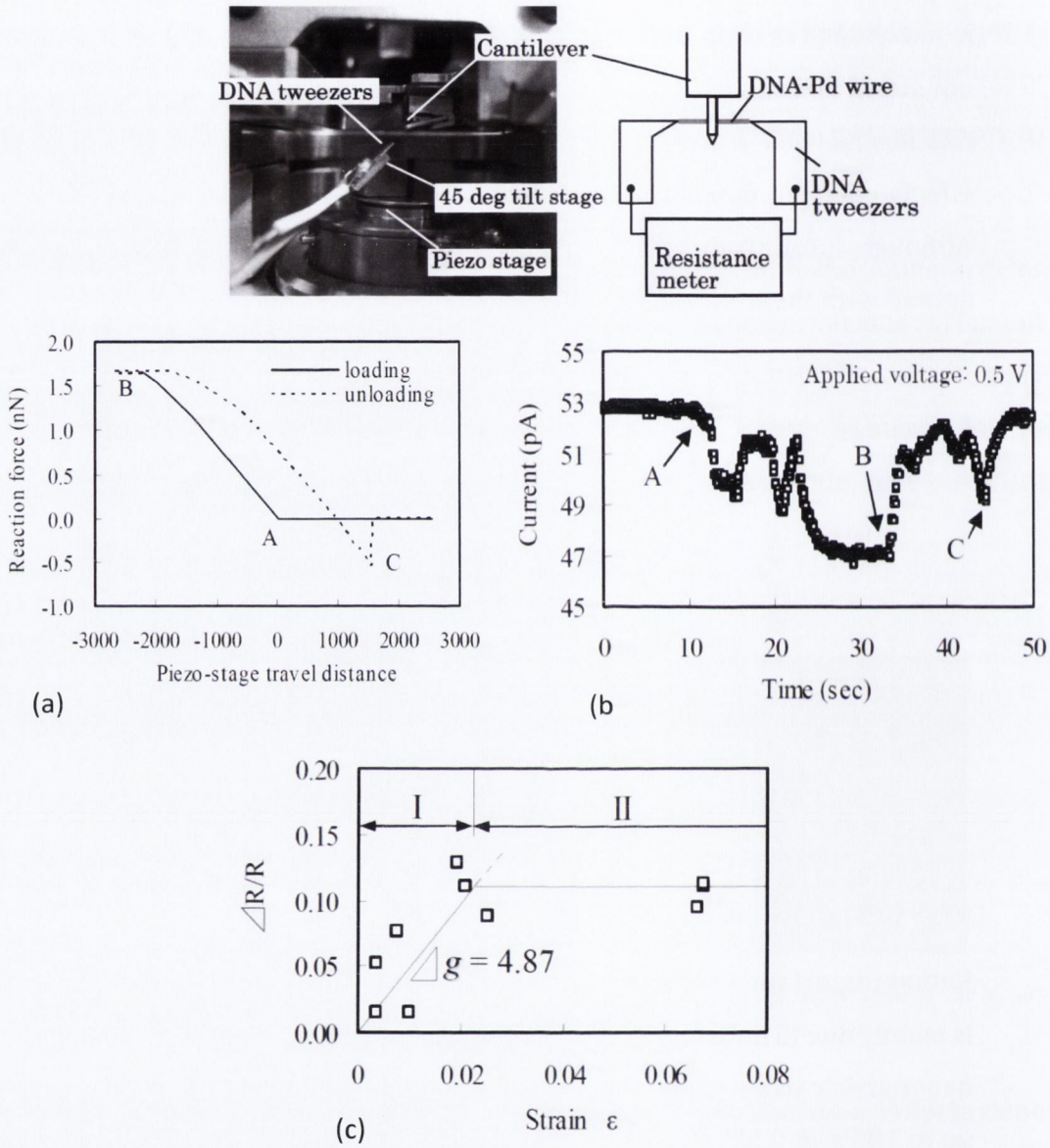

Figure 12:(a) force-deflection curve showing the loading and unloading behaviour of the DNA-Pd wire, (b) real time recording of the current change during loading and unloading and (c) relationship between resistance change and strain[35].

Figure 11 shows a photograph of the experimental chamber and a schematic of the measurement technique. The DNA-Pd NP wire is mounted between the tweezers

probes while the AFM tip is used to load and measure the mechanics. The spring constant of the AFM tip was kept very low, 6.4 *mN/m*, in order to apply small high precision loads to the wire.

The Pd NP used to coat the DNA wire were ~ 3 *nm* in diameter and cover the surface of the DNA. Due to the cationic repulsion between the Pd particles it was considered that only a single layer of Pd NP covered the DNA molecules. Figure 12 (b) shows the current change with time at critical loading points shown in figure 12 (a). At point 'A' the loading process begins to a maximum load at point 'B'. The recovery process from 'B-C' shows a change in stiffness which indicates viscoelastic deformation. The electrical current is monitored at a constant 0. 5 *V* source voltage. After a given deformation the current starts to drop. The maximum current drop is shown at point 'B', the point of maximum load. Between points 'A-B' there are two peaks when the current briefly returns to un-strained levels. These peaks are not explained in the paper but may be a result of the viscoelastic nature of the system under strain. Unloading between points 'B-C' is accompanied by a rapid increase in current. At point 'C' a brief decreasing current peak was observed, reflecting the application of a negative force on the wire, by the tip, as it overcomes electrostatic attraction. The current returns to its previous level after deformation. Resistance change (ΔR/R) with strain is shown in figure 12 (c). In region I a resistance increase of 12% was observed at 2. 2% strain. In region II further resistance change becomes independent of strain. The piezo-resistance characteristics of the wire are attributable to the distance change of each Pd NP coating the wire surface. The effect of contact resistance was not discussed but may in fact play a huge role in resistance changes. 4-point electrical measurement would elucidate the true mechanism.

Electromechanical measurements on nanoparticles are interesting due to their small volume and may show unusual behaviour that could be of use in technological applications. However, measuring the electromechanical properties of 0D materials is extremely difficult, as shown by the lack of publications in the area. Currently the field is dominated by papers describing the electromechanical properties of NP assemblies, such as, films and wires. The obvious difficulty is the design and fabrication of systems to measure such properties of 0D materials. 2-dimensional

materials are more amenable to electromechanical measurements. The next section discusses 2-dimensional electromechanical measurements.

1.3.2 2- Dimensional (2D) electromechanical measurement – thin films

Thin films are 2-dimensional (2D) in nature because they experience electron confinement in 1 direction. Thin films have been studied extensively mainly due to their application in devices[36, 37]. Their characterisation provides a wide range of information on surface physics and chemistry, interfacial properties, mechanical and electrical properties. Methods to investigate the electromechanical properties of thin films include stretching[38], compression[39] and bending[40] experiments. There are a vast number of papers published on the electromechanical properties of thin films, ranging from metallic devices, to nanoparticle films, to nanowire network films. The following review is a selected overview of the different types of electromechanical measurements performed on 2D films, mainly nanowire/nanotube network films.

In 2010, Fraga *et al*[40] studied the effect of nitrogen doping on piezoresistive properties of amorphous silicon carbide (a-Si_xC_y) thin film strain gauges. The films were prepared by plasma-enhanced chemical vapour deposition (PECVD) with the strain gauges fabricated by conventional photolithography, metallisation and reactive ion etching (RIE). Piezoresistive measurements were performed using the beam bending method. Figure 13 (a) shows how the strain gauge is loaded. The a-Si_xC_y was bonded to the clamped edge of a stainless steel cantilever beam. Strain is induced by adding calibrated weights to the free end of the beam, labelled 'F'. The electrical resistance of each strain gauge type was measured both without applied load and during loading. The beam bending produces uniaxial strain along the length of the beam. The piezoresistive coefficient of the thin film resistor was calculated from equation 15 below;

$$\frac{\Delta R}{R} = \pi_l (1 - \nu)\sigma_l \qquad (15)$$

where R is the resistance, π_l is the longitudinal piezoresistive coefficient, ν is Poisson's ratio and σ is the applied strain. Figure 13 (b) shows the change in resistance for both nitrogen doped and un-doped thin films. The authors found a

huge increase in resistance in both cases, which is reflected in the gauge factor shown in figure 13 (c). Figure 13 (d) shows the change in the piezoresistive coefficient due to stress. A decrease was observed in both cases. Unfortunately, the mechanism for the resistance increase or the change due to doping was not discussed. A similar type of experiment was also performed by Biasotti *et al*[41] on $La_{0.7}Sr_{0.3}CoO_3$ thin films in 2010. In this paper an increase in resistance was observed with applied tensile strain. The authors found a resistance increase of ~0.6% at 0.12% strain. Tensile stretching measurements have been performed on other thin film materials such as ZnO[42] and Titanium[43] strain gauges.

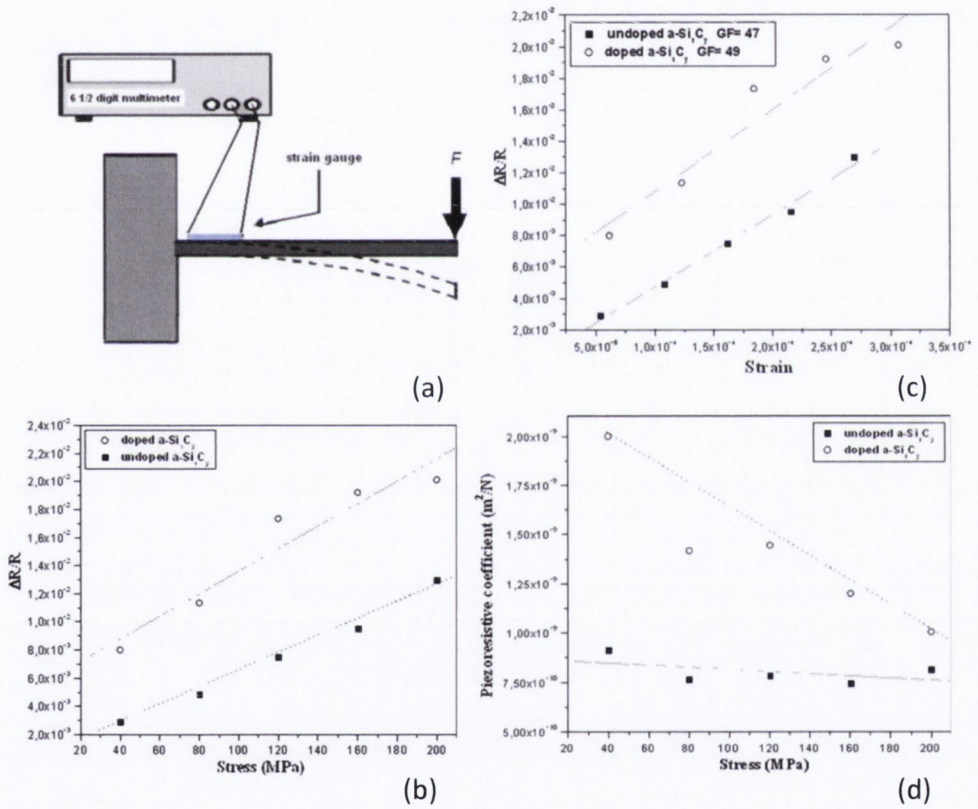

Figure 13: (a) Schematic diagram of the cantilever beam bending method used for piezoresistive measurements, (b) the fractional resistance change as a function of stress for both types of strain gauges, (c) the fractional resistance as a function of strain for doped and un-doped strain gauges and (d) the piezoresistive coefficient as a function of stress for nitrogen doped and un-doped strain gauges[40].

Another area of non-conventional thin film research has focused on nanomaterial assemblies. Thin films fabricated from single entity nanomaterials have shown prominence in the literature. Thin film gauges have been made from carbon

nanotubes (CNT)[44-47], hybrid CNT films[48], graphene[38], polymer nanofibres[49] and nanowires[50, 51].

In 2013, Bae *et al*[52] reported on a graphene based strain sensor. In this paper chemical vapour deposition (CVD) graphene was grown on Ni catalysed SiO_2/Si substrate and transferred to a poly(dimethylsiloxane) (PDMS) flexible substrate. The piezoresistive properties of the graphene film were measured by applying uniaxial tensile strain via stretching. The authors observed a continuous increase in normalised resistance as a function of strain, shown in figure 14.

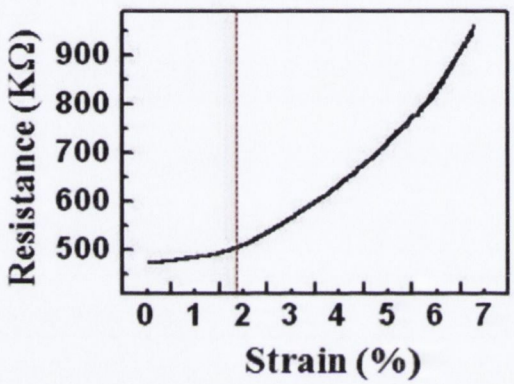

Figure 14: Resistance as a function of strain for graphene based strain sensor[52].

A maximum strain of 7.1% was applied with a resistance increase of just over 200%. In region 1, below 2% strain, the linear increase in resistance was attributed to carbon-carbon bond stretching. The non-linear region 2, above 2% strain, was explained by the imperfection of the material i.e. crystallographic imperfections and doping concentrations as well as other less intrusive factors such as temperature changes and carrier effective masses[53]. Other research on thin film CVD graphene strain sensors have shown similar behaviour[54] in addition to sprayed graphene flakes[38].

In 2011, Lipomi *et al*[44] measured the electromechanical properties of sprayed CNT thin films. Rather than beam bending they utilised stretching to apply tensile strain to the films. In this paper CNT thin films were prepared by spray coating tubes onto a stretchable substrate, PDMS. The electromechanical properties were measured by stretching the PMDS substrate to a particular strain per cent while measuring the change in resistance. Figure 15 (a) shows the change in resistance as a function of

strain for seven stages of applied strain and relaxation. It was observed that on the first application of 50% strain the resistance increased by a factor of 0.71. This was attributed to loss of tube-tube junctions as the substrate is stretched. On relaxation the authors found the resistance to recover to 0.64 of the initial resistance. Interestingly they observed that when the film was strained by greater than 50% of the previous maximum strain, there was a higher relaxed state resistance. This is clearly seen by the systematic increase in resistance when the film is strained beyond 50% of its previous load. This effect is due to the CNT's aligning parallel to the strain direction, decreasing the number of junctions hence increasing the resistance. Figure 15 (b) displays the reproducibility in resistance change if the strain not increased beyond 50%.

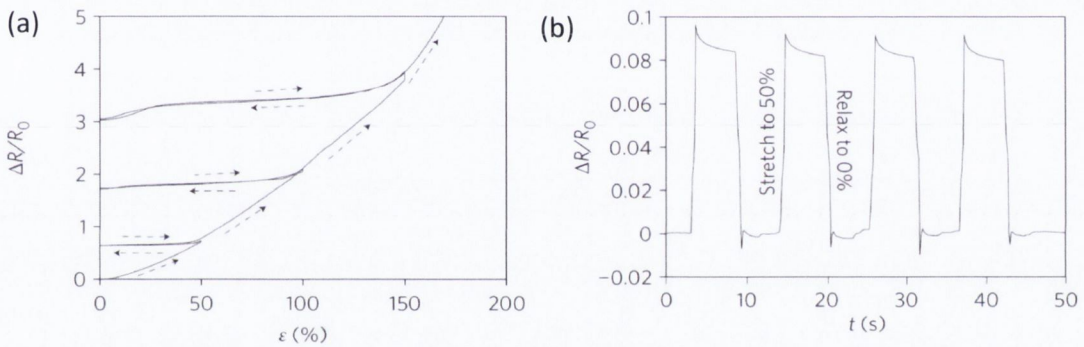

Figure 15: Effect of applied strain on spray coated CNT films on PDMS. (a) Change in resistance versus strain for a nanotube film on a PDMS substrate, (b) Resistance change with time in response to four cycles of stretching from 0 – 50%[44].

Yu *et al*[55] observed similar results to Lipomi *et al*[44], albeit for a slightly different CNT system. There have also been reports on nanotube films being stretched up 100% without a significant resistance increase[56].

Xu and Zhu studied the electromechanical properties of silver nanowire thin films in 2012[51]. In this paper the authors use stretching to uniaxially deform a drop cast thin film of 90 *nm* diameter silver nanowires (Ag NW) on a stretchable substrate. Thin films were fabricated by drop casting a highly concentrated Ag NW solution onto Si substrates. The substrates were then covered in liquid PDMS and allowed to cure. The PDMS was then peeled away from the Si substrate with the Ag NW network left embedded in the cured PDMS. In this paper the film was stretched using a tensile

testing stage. Figure 16 shows the resistance change as a function of the applied strain.

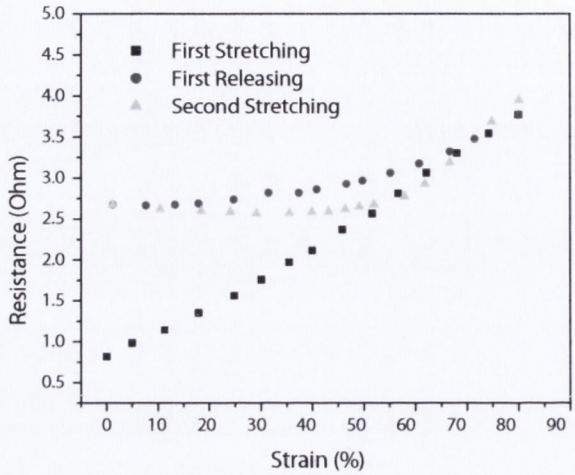

Figure 16: Resistance of AgNW/PDMS conductor as a function of tensile strain[51].

It was observed that the resistance increased linearly from 0.82 Ω to 3.77 Ω when the tensile strain was increased to 80%. Upon release of the strain, the resistance partly recovered to 2.67 Ω. When the film was strained again to 80% the resistance showed no change up to 50% strain, then increases linearly to 80% strain, following the same path as the initial strain cycle. After repeated stretching cycles below 50% strain stability in the resistance change was observed. Using optical imaging the film was found to permanently deform at 80% strain which explains the observed ground state change in resistance on release. The stretchable range with stable resistance is comparable to CNT-based stretchable conductors where the resistance is much lower in the stretched state[57-59].

In 2011, Yu *et al*[60] measured both tensile and compressive strain on Ag NW films via bending. They found no change in resistance during compression and an increase in resistance of 2.9 times at a tensile strain of 16%. Similarly in 2012 Yun *et al*[61] used stretching to measure the resistance change with strain of embedded Ag NW networks. They found a two order of magnitude increase in sheet resistance at 140% strain. Other nanowire systems studied include ZnO nanowire/polystyrene hybridised thin films[50].

Electromechanical measurements on thin films have been performed extensively on a wide variety of materials. This has given us an insight into the fundamental characteristics and properties of the materials themselves, as well as the opportunity to develop new devices[44]. There is a huge variation in the degree of resistance change with strain from material to material, and even within the same material group as shown for CNT strain gauges. There is also a dependence on the method of testing, be it bending or stretching type experiments. The techniques to measure the electromechanical properties of thin film type materials have been discussed above. 2D materials still remain a topic of great interest in the literature.

1.3.3 1- Dimensional (1D) electromechanical measurement – nanowires

Nanowires are of particular interest due to their potential application as fundamental building blocks of future electronic, optoelectronic, electromechanical, sensing and actuation nanosystems[62], as well as the building blocks in NW films that can help separate junction effects from the influence of the actual wires[63]. Researchers have been able to demonstrate unique and novel functionality using nanowires; for example, high mobility single nanowire transistors[64], strain controlled logic gates[65], single nanowire lasers[66], strain sensors[67] and nanoelectromechanical systems (NEMS)[68]. In 1D materials reduction in lateral dimensions should result in a decrease in the number of defects per unit length resulting in superior mechanical properties compared to bulk[69], as well as interesting electronic[70], optical properties[71] and enhanced electromechanical properties[72, 73]. The main area of focus within 1D electromechanics is piezoelectric materials, however, similar experimental methods can be used to characterise other materials that do not display piezo behaviour. The most common methods for characterising piezoelectricity in nanowires usually involve tensile loading or lateral bending of the material with simultaneous electrical measurement. The former technique can involve *in-situ* electron microscopy (EM) utilising a tensile loading stage, while the latter utilises lateral AFM and a specific form of AFM known as piezoresponse force microscopy (PFM). Here, EM and AFM based techniques will be discussed separately.

1.3.3.1 EM based techniques

In 2012, Espinosa *et al*[74] published a review on *in situ* electromechanical testing of nanowires and nanotubes. Electron microscopy based electromechanical measurements generally utilise a TEM for high resolution imaging with an *in situ* tensile strain gauge for mechanical manipulation and electrical measurement. The benefits of *in situ* measurements include; high resolution imaging giving atomic resolution, crystal structure through diffraction and high speed image acquisition, allowing for precise material analysis during deformation. The identification of pre-existing defects in 1D nanostructures and its relevance to mechanical and electromechanical properties deserves special attention[75].

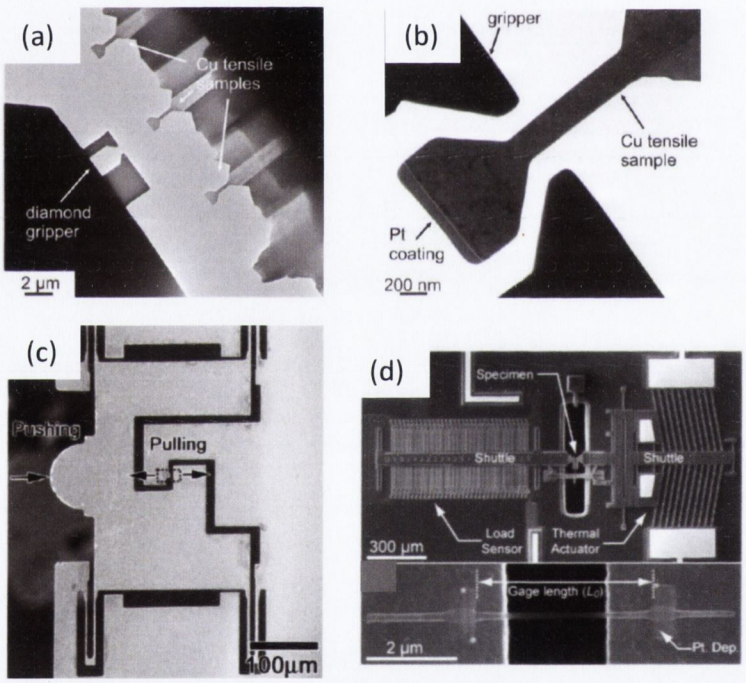

Figure 17: (a) Low magnification TEM image showing several tensile samples as well as the conductive diamond gripper used to load the individual specimen, (b) Higher magnification image of gripper aligned to the sample prior to tensile testing[77], (c) SEM image of the push-to-pull device. The transfer of a compressive load to tensile load is clearly shown[81]. (d) SEM image of the MEMS device as well as a single GaN nanowire mounted between the actuator and sensor, welded with electron beam induced deposition of platinum (Pt-EBID)[74].

Stacking faults and defects are well known to influence the mechanical response. However, their influence on electromechanical properties are not well understood and are generally overlooked due to difficulty in measurement. Inversion domain boundaries and dislocations inducing a localised strain have a known effect on piezoelectricity[76]. Also, the role of stacking faults and surface defects is not well established but is known to locally alter band structure and hence transport properties[76].

There have been multiple techniques described for measuring mechanical and electromechanical properties using *in situ* TEM. In 2011 Kiener *et al*[77] measured the mechanical properties of FIB fabricated copper nanostructures using *in situ* TEM. Figure 17 (a, b) shows low magnification TEM images of their experiment arrangement. A conductive diamond gripper coupled with a picoindenter, for precise strain application, is used to apply a tensile load to the Cu nanostructures and garner mechanical information on the sample. *In situ* TEM compression experiments on various types of nanowires have also been demonstrated[78-80]. Resonance methods have been applied to study the mechanical properties of nano-materials. In resonance characterisation, the modes of vibration of a free standing nanostructure are characterised and the mechanical properties extracted based on continuum and statistical mechanical models[74]. A variety of nanowire materials have been studied using this method[13, 42, 43]. A slightly different method of applying a tensile load was demonstrated in 2011[81]. In this paper, a microfabricated flexure microelectromechanical system (MEMS) stage was used to convert the compressing motion of a nanoindenter into tension on 270 *nm* diameter VO_2 nanowires[81], figure 17 (c). In this type of system, load is applied using a thermal actuator on one side of the freestanding specimen and is measured on the other side using a differential capacitive load sensor based on interdigitated electrodes[82-86]. Local structural information during deformation is visualised via TEM. The experimental setup is shown in figure 17 (d).

As well as mechanical properties MEMS devices have been used to probe the electromechanical properties of nanowires. In 2011 Yong *et al*[87] characterised the piezoelectric response of Silicon nanowires using a MEMS device. In this paper the authors use the MEMS device for simultaneous electrical and mechanical

characterisation of individual nanowires. The device consists of an electrostatic actuator and two capacitive sensors, shown in figure 18 (a). On the left side of the device the actuator shuttle includes an electrostatic actuator and a capacitive displacement sensor. The force sensor contains a capacitive force sensor which measures the tensile load on the specimen as well as the displacement as a result of the load. Here, the authors use *in situ* SEM to select and mount the nanowire onto the MEMS device. The electromechanical results are shown in figure 18 (b). The nanowire specimens were strained from 0% to 3%, while recording an IV sweep at incremental strains. The resistance and resistivity at 0% strain were determined to be 5.9 x 10^{11} Ω and 406 Ω *m*. At 3% strain the resistance and resistivity decreased by a factor 26.8 showing the piezoelectric behaviour of silicon nanowires.

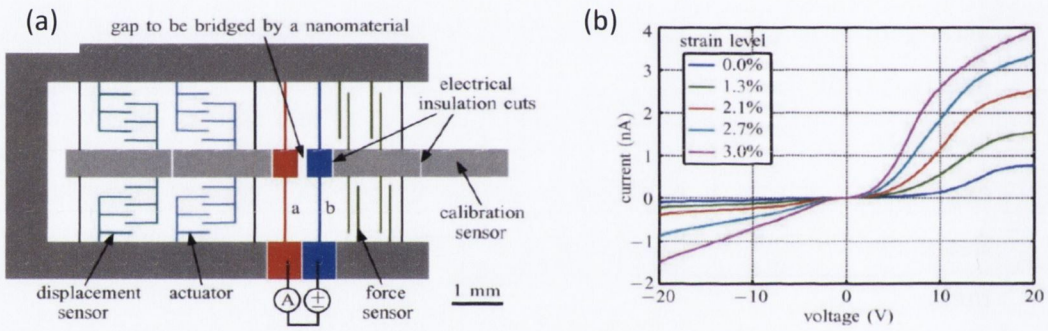

Figure 18: (a) Schematic of the MEMS device used for electromechanical characterisation. Force and displacement data are both acquired simultaneously. (b) IV characteristics of silicon nanowire under different strain conditions[87].

Importantly, the electrical measurement was performed in a 2-point geometry. Hence, the effect of the contact resistance under the loading is not accounted for, although, the authors do discuss the observed Schottky barrier purely in terms of the electrical measurement. A similar 2-point electromechanical MEMS approach was performed by Kiuchi and colleagues[88], albeit using a slightly different MEMS device. Here, the authors studied the piezoresistance of carbon nanowires. Rather than single nanowires, double bridged nanowires were analysed. On tensile loading of up to 9.8% a resistance increase of ~3% was observed. It was also observed that above 4% strain the resistance decreases back to its initial state. This was attributed to phase transition in the carbon nanowires[88]. Other reports include the measurement of mechanical and electrical properties separately using a MEMS device[89].

It is important to measure the electromechanical properties of nanowires in a 4-point electrical geometry. This allows for accurate resistance and resistivity measurement by removing the effects of contact resistance. Also, the contact resistance is dynamically changing as the nanowire is loaded, usually as a result of the contact acting as the pinning point as well as an electrical probe. In 2011, Espinosa and Bernal[90] patented an *in situ* 4-point MEMS testing system. In this device, a previously established platform for mechanical measurements[86] was extended to accommodate four independent electrical connections to the nanostructure. Figure 19 is an SEM image of the MEMS device showing the four electrical connection leads as well as a nanowire mounted onto the device. The contact leads are fabricated on freestanding silicon nitride layers to ensure that all electrical signals are isolated from each other. The specimen is connected to the leads via Electron Beam Induced Deposition (EBID) of Pt in a Focused Ion Beam (FIB) chamber.

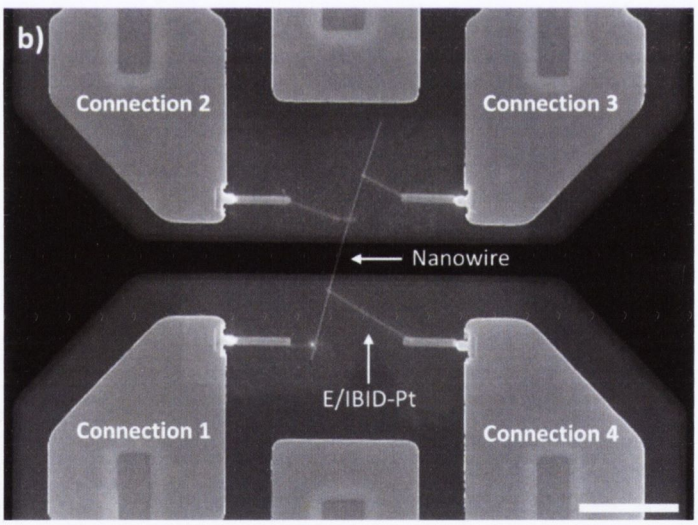

Figure 19: MEMS device for four point electromechanical measurement. A single nanowire is contacted to four pads using Pt-EBID. (5 μm scale bar)[90].

The authors have yet to publish results on the electromechanical properties of nanowires using this device[90]. Other types of *in situ* electromechanical measurements have been reported on ZnO nanowires[91, 92] and copper nanowires[93].

Electron microscopy techniques for electromechanical measurements on single nanowires have been shown to be extremely informative. However, there are

currently limitations to the technique, such as; sample throughput and preparation as well as dimension limitations[74]. Generally, nanowires are mounted on to the testing device using *in situ* SEM micromanipulation needles. However, it is extremely difficult to manipulate structures <100 *nm* in diameter using this method. This limits the technique to larger nanostructures. AFM based methods are more suitable for measuring mechanical and electromechanical properties of nanowires. Generally, in performing AFM based experiments, the nanowires being studied are drop cast or grown onto the support substrate. As a result the size distribution of nanowires varies widely i.e. both small and large nanowires in diameter can be measured. This gives greater sample throughput across a wide range of dimensions, not limited to micromanipulation of nanowires. In the next section AFM based techniques are discussed.

1.3.3.2 AFM based techniques

1.3.3.2.1 Piezoresponse Force Microscopy

In 2012, Espinosa *et al*[75] published an excellent review on techniques to measure the electromechanical and piezoelectric properties of nanowires. PFM is a scanning probe technique where a metal coated AFM tip is used to apply a local electric potential to an area of interest and measure the resultant displacement of the AFM tip as a function of the applied potential. This type of measurement is ideal for nano-sized piezoelectric specimens as it has the ability to apply local electric fields and measure the piezo-response in the same location. Generally, PFM systems are coupled with a waveform generator to monitor AC voltage response. Vertical and lateral piezoelectric behaviour can be monitored by the tip. PFM measurement on nanowires is non-trivial and it requires precise tip positioning on the nanowire, which are often under 100 *nm* in diameter. Despite these difficulties, PFM has been widely used to study the piezoelectric effect at the nanoscale[60, 94-101].

In 2006, Fan *et al*[102] reported on the piezoelectric properties of vertically aligned ZnO nanopillars. The authors used PFM in their experimental approach. In this method the pillars were template grown on a highly doped substrate that also functioned as a bottom contacting electrode. As the pillars are vertically aligned their top facet is in contact with the AFM tip, which acts as a top contacting electrode.

Figure 20 (a) shows the experimental setup for this type of experiment. This method allowed multiple PFM measurements to be performed on several pillars at once. This is seen in figure 20 (b), the panel on the left shows the PFM image while the right image is the topography channel. The correspondence between the bright areas on the PFM image and the top of the individual pillars on the topography image can be observed. ZnO nanopillars with an average diameter of 300 *nm* were studied, with a piezoelectric constant of ~7.5 *pm/V* obtained. In this paper the AFM tip was in contact with the pillar (0001) surface, rather than the nanowires lying flat on the substrate surface. Figure 20 (c) shows the linear behaviour of the observed piezoresponse amplitude against the applied electric potential.

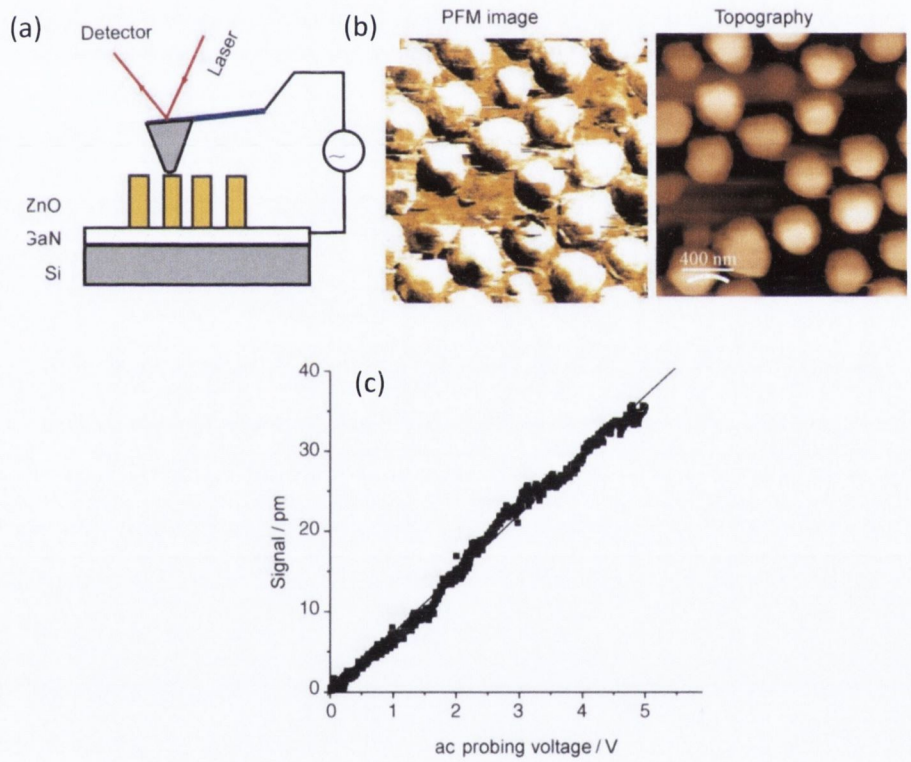

Figure 20: Piezoelectric characterization of the 300-nm ZnO pillars. a) Schematic diagram of the measurement setup. b) A typical scanning piezoresponse image showing that the piezoresponse signals originate selectively from the pillars (bright spots in the image). c) Measurement on an individual pillar with a probing frequency of 33. 25 kHz. The piezoelectric coefficient was determined to be (7.34±0. 3) pmV⁻¹ from the slope of the linear fit[102].

Scrymgeour *et al*[103] performed a similar study on vertically aligned ZnO nanorods in 2008, using nanorods between 400-600 *nm* in length and 150-500 *nm* in diameter. To ensure the mechanical stability of the vertically aligned nanorods during contact mode imaging the authors embedded the nanorods in a photoresist and performed light plasma etching to expose the top of the rods. A variation in the piezoelectric constant from 0.4 to 9.5 *pm/V* was observed. Interestingly, a direct correlation was found between the nanorods resistivity and piezoelectric coefficient. Nanorods with a lower piezoelectric response display a low resistivity, with variation from 0.1-155 Ω *cm*. The variation in resistivity was attributed to inhomogeneous impurity incorporation across the growth substrate. The variation in the piezoelectric coefficient with resistivity was explained by the reduction of the Madelung constant due to free electrons, confirming earlier results that conductivity quenches the piezoelectric response[68].

PFM measurements have also been reported on GaN nanowires as small as 64 *nm* in diameter[94]. In this paper, PFM was performed on nanowires drop cast on a flat, gold covered substrate, the gold substrate acting as a bottom contact while a metal coated AFM tip acts as the top contact. For this type of measurement it is essential to align the nanowire facets to the tip direction, achieved by orienting the substrate to the tip. Nanowires with hexagonal structure were grown by catalyst free molecular beam epitaxy (MBE) and showed a piezoelectric constant of ~10 *pm/V*, three times that of the bulk value. The results obtained are summarised in figure 21. An AFM topography image of a 64 *nm* GaN nanowire is shown in figure 21 (a), with simultaneous piezoresponse amplitude and phase image shown in (b) and (c). In this experiment an AC potential was applied via a 10 V_{pp} function, with a low scan rate of 0.25 *Hz*. The top facet of the nanowire exhibits a strong piezoelectric signal, clearly seen in figure 21 (d). This level of accuracy can only be obtained by the precise orientation of the AFM tip with the nanowire. The lateral facets show minimal piezoresponse. A linear behaviour between the piezoresponse and the applied voltage was observed, figure 21 (e). The obtained shear piezoelectric constant of the nanowire was 10 *pm/V*.

In 2011 Minary-Joulandan *et al*[73] highlighted the importance of measuring all three independent piezoelectric constants in nanostructures. Nearly all studies on the

piezoelectric characterisation of nanowires provide only one piezoelectric constant, generally the out-of-plane piezoelectric deformation measured by vertical bending of the AFM tip. However, full piezoelectric characterisation on individual nanowires is possible by PFM. In this paper the torsional twist and flexural bending of an AFM tip was employed to measure the in-plane and out-of-plane displacements induced by applying AC voltage on the piezoelectric nanowire. Through the application of an electric field in various directions and by physically rotating the nanowire with respect to the AFM tip, the three piezoelectric constants in individual GaN nanowires were measured. The authors found that for nanowires with diameters ranging from 64-190 *nm*, piezoelectric coefficients of d_{33}= 12.8 *pm/V*, d_{13} = 8.2 *pm/V* and d_{15} = 10.2 *pm/V* were observed, revealing GaN nanowires display a piezoresponse of up to six times the bulk value.

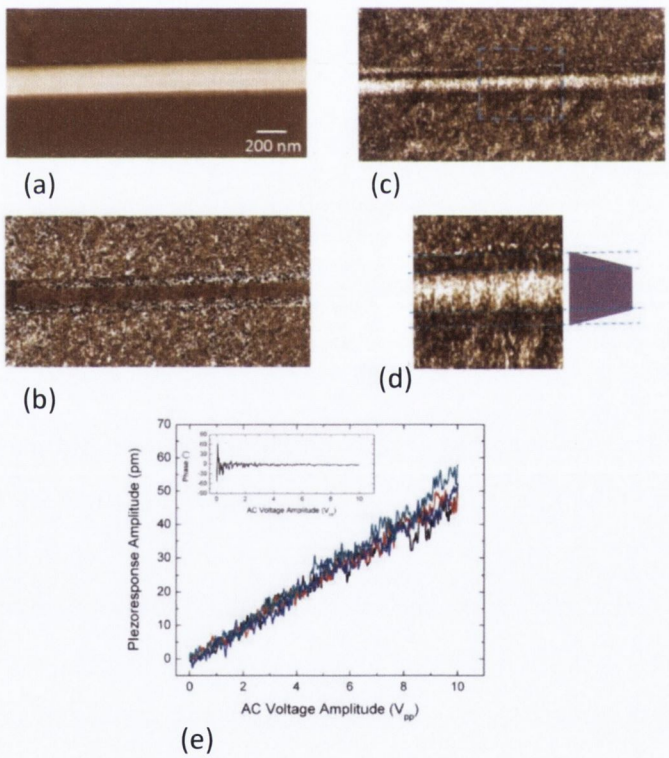

Figure 21: (a) AFM topography image of 64 nm GaN nanowire, (b) PFM piezoresponse phase image and (c) amplitude image. (d) Higher magnification image of section marked in (c). It is clear to see the top facet of the nanowire displays a strong piezoresponse. (e) Lateral piezoresponse amplitude versus applied AC voltage peak-to-peak amplitude. Four responses measured over different areas of the nanowire showing the reproducibility of the measurement[94].

1.3.3.2.2 AFM lateral bending

Lateral bending measurements using an AFM tip has been widely used to measure the mechanical properties of nanowires[7, 78, 79, 104, 105]. This principal has also been applied to the study of electromechanical and piezoelectric properties of nanowires. In lateral bending experiments, a conductive AFM probe bends the nanowire and the generated electric potential across the nanowire is measured with the same conductive probe. This was shown by Wang and Song in 2006[106]. In this paper the authors studied the conversion of mechanical load into electrical power of vertically aligned ZnO nanowires, figure 22 (a). Nanowires were grown via the Vapour-Liquid-Solid (VLS) process on an α-Al_2O_3 substrate with Au particles as a catalyst. A Pt covered AFM tip was used to load the nanowire and act as a contacting electrode. The bottom contact was inherently fabricated during the nanowire synthesis process and simply involved applying silver paste to the ZnO film formed. Figure 22 (b) shows a TEM image with the inset diffraction pattern showing a growth direction of [0001]. The measurement was performed in contact mode with a constant tip-sample force of 5 *nN* applied. Figure 22 (c) schematically outlines the measurement procedure. As the AFM scans the surface it contacts the vertical nanowires and imparts a lateral load. The nanowire mechanics are monitored by the AFM tip deflection while a circuit loop records the electrical response to the load. Using well defined nanowire arrays the authors found a potential power output of ~10 $pW/\mu m^2$. Similar experiments have been performed on ZnO nanowires elsewhere[76, 80]. This method has also been applied to CdS nanowires[80] and GaN nanorods[13]. Theoretical calculations have shown that in lateral bending by an AFM tip, the maximum potential produced at the nanowires surface has an inverse relationship with the cube of its length/diameter aspect ratio and a direct relationship with the lateral displacement by the probe[82].

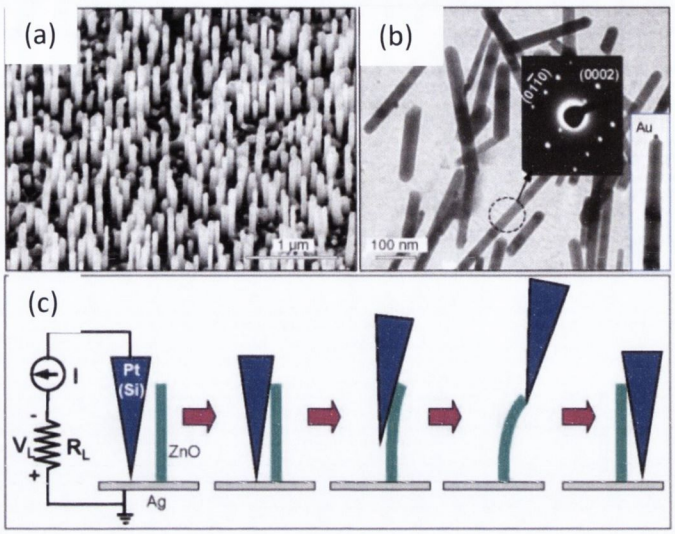

Figure 22: Experimental design for converting nanoscale mechanical energy into electrical energy by a vertical piezoelectric ZnO NW. (a) SEM image of vertically aligned ZnO NW, (b) TEM image of ZnO NW with diffraction pattern inset and (c) schematic of experimental setup and procedure used to deform nanowires and measure the piezoresponse[106].

In 2011, Xu *et al*[107] used an improved method to study the piezoelectric properties of GaN nanowires. In this study, two types of GaN nanowires were analysed; intrinsic GaN nanowires and Si doped (n-type) GaN nanowires with AIN insertion in the middle of the wire. The nanowires were grown by MBE on silicon substrates using a 2 *nm* thick AIN buffer layer to improve the nanowire orientation. Using this method 25-30 *nm* diameter vertically aligned nanowires were obtained at a surface density of approximately 250 $NW/\mu m^2$. Doped nanowires were grown by introducing Si impurities during growth, followed by the deposition of an 8 *nm* AlN barrier layer. The continued growth produced silicon doped GaN nanowires. The experimental procedure is outlined in figure 23 (a).

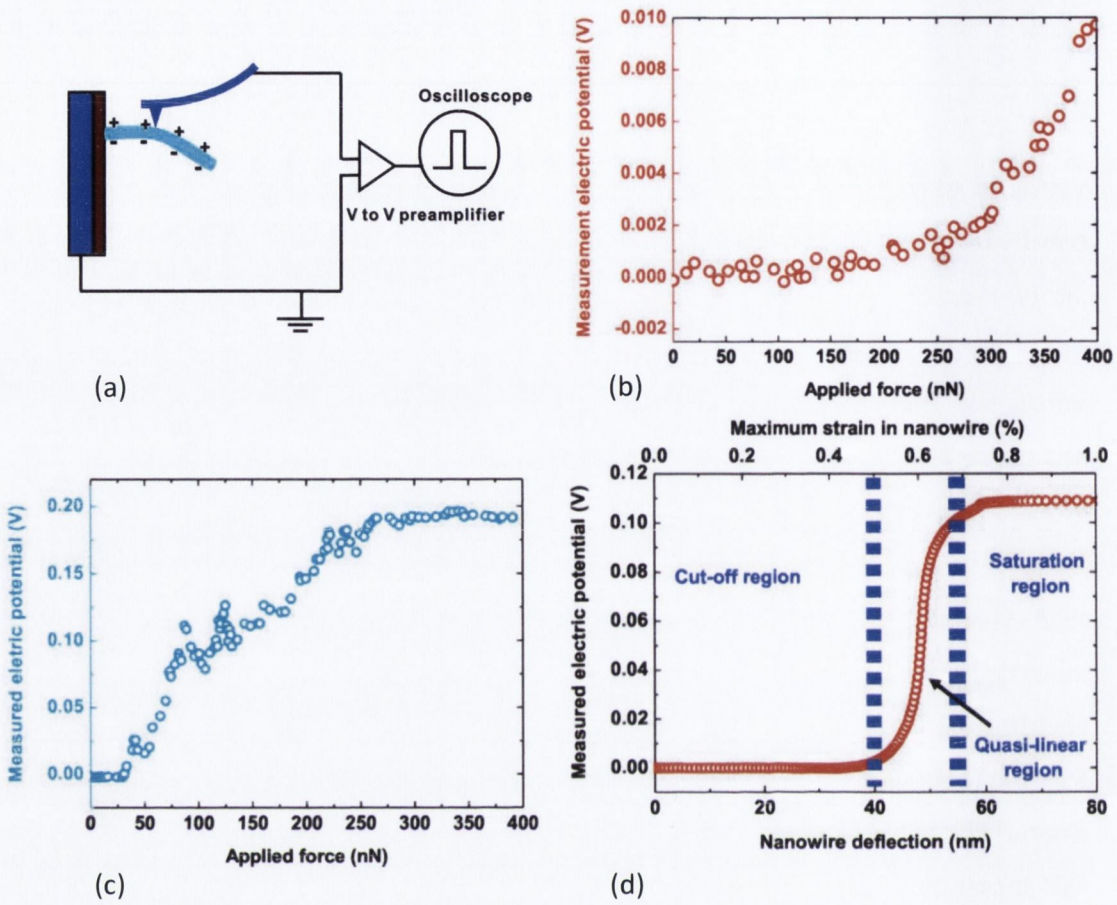

Figure 23: (a) Schematic of the experimental configuration, (b) measured electric potential of intrinsic GaN nanowire and (c) doped nanowire as a function of applied force. (d) Measured electric potential as a function of nanowire deflection for intrinsic GaN nanowire[107].

The sample is vertically fixed to a metal support using silver paste to ensure ohmic contact. This acts as the back contact for the electrical measurement. The Pt-Ir covered metallic AFM tip acts as the top contact and completes the circuit when contact to the nanowire is made. The authors performed the measurement by first acquiring a topographic image of the nanowire array. This allowed a suitable nanowire to be chosen as well as the ability to precisely choose the load point on the nanowire beam, enabled by using a closed loop AFM scanner. The AFM tip can be used to load the nanowire at multiple points along its length. Here, the AFM tip acts as both a mechanical tool and electrical measurement system, recording both properties simultaneously. Figure 23 (b, c) show the results obtained. Under the same experimental conditions the authors found that the measured electrical

potential of intrinsic GaN nanowires is 1.7 x 10^{-3} *V* (figure 23 (b)) and 2.0 x 10^{-1} *V* (figure 23 (c)) for Si doped GaN nanowires. Both measurements were performed at a 250 *nN* load. The relation between measured electric potential as a function of nanowire defection is shown in figure 23 (d). The potential-deflection curves can be divided into three regions. In the cut-off region there is no potential change observed as the nanowire is deformed. This is attributed to the Schottky barrier restriction and the bad electrical tip-nanowire contact induced by the weak force at the beginning of the manipulation. It is also considered that the deflection was too small to alter the band structure. At a critical strain (quasi linear region) the Schottky barrier is eliminated and the potential change with load can be monitored. The authors found for intrinsic GaN nanowires the potential change is almost 15 times higher than theoretical calculations and almost 45 times higher for Si doped GaN nanowires. The significant difference in theoretical calculations and experiment was attributed to piezoelectric and dielectric size dependence effects[107]. Other bending techniques have been applied to single nanowires, such as that shown by Toriyama *et al*[108] on silicon nanowires and bending experiments on CNT's shown by Cao *et al*[109].

A multitude of techniques and experimental setups have been used to probe the electromechanical properties of nanowire systems. In terms of AFM based techniques, piezo-force-microscopy is commonly used to measure the piezo-response of individual nanowires. Although there have been reports on applying the AFM as an electromechanical tool[109], AFM based techniques have generally been avoided, due to the difficulty in combining accurate 4-point electrical measurements and mechanical capabilities. In this thesis, we further the understanding of AFM based electromechanical measurements by combining accurate electrical characterisation in tandem with precise mechanical measurements.

1.4 Conclusion

Electromechanical measurements on the nanoscale have been studied using a wide range of methods. Thin films are generally probed by bulk like tensile stages or macro bending setups. Nanowires have been mostly studied using either AFM or EM techniques. The advantage of *in situ* EM methods is accuracy in measuring the

specimen dimensions as well as the possibility of real time atomic resolution imaging during deformation. They are usually extremely challenging measurements to perform, with limited flexibility in terms of experimentation on materials with dimensions <100 *nm*. The advantage of an AFM-based technique is the ability to experiment on nanowires as small as 20*nm* and extract a wide variety of properties (resistance, resistivity, modulus, strength and fracture mechanism). Beam-bending experiments using AFM allow us to probe and control the bending moment very accurately, important in characterising potential NEMS devices.

The next chapter outlines the methods and equipment used to perform the experiments throughout this thesis.

1.5 References

1. Feynman, R.P., *"There's Plenty of Room at the Bottom".* Engineering and Science Magazine, 1960. **23**(22).
2. Moore, G.E., Electronics, 1965. **38**: p. 114.
3. http://www.itrs.net/links/2009ITRS/Home2009.htm, 2009.
4. http://www.itrs.net/Links/2005itrs/home2005.htm, 2005.
5. http://www.itrs.net/Links/2012ITRS/Home2012.htm, 2012.
6. Loh O. Y., E.H.D., *Nanoelectromechanical contact switches.* Nature Nanotechnology, 2012. **7**(5): p. 283-295.
7. Bin Wu, A.H., John J. Boland, *Mechanical properties of ultrahigh strength gold nanowires.* Nature Materials, 2005. **4**(525-529).
8. Ngo, L.T., et al., *Ultimate-Strength Germanium Nanowires.* Nano Letters, 2006. **6**(12): p. 2964-2968.
9. Hertzberg, R.W., *Deformation and Fracture Mechanics of Engineering Materials.* John Wiley & Sons, Inc., 1996.
10. Callister, W.D., *Materials Science and Engineering; An Introduction.* John Wiley & Sons, Inc., 2003: p. 117.
11. J. J. Wortman, R.A.E., *Young's Modulus, Shear Modulus, and Poisson's Ratio in Silicon and Germanium.* Journal of Applied Physics, 1965. **36**: p. 153.
12. Davies, J.D., and Bose, D. K., *Stress distribution in splitting tests.* J. Am. Concr. Inst., 1968. **65**(8): p. 662-669.
13. Treacy, M.M.J., T.W. Ebbesen, and J.M. Gibson, *Exceptionally high Young's modulus observed for individual carbon nanotubes.* Nature, 1996. **381**(6584): p. 678-680.
14. Yu, M.-F., et al., *Strength and Breaking Mechanism of Multiwalled Carbon Nanotubes Under Tensile Load.* Science, 2000. **287**(5453): p. 637-640.
15. P. Poncharal, Z.L.W., D. Ugarte, W. A. d Heer, Science, 1999. **283**: p. 1513.
16. Y. Zhu, H.D.E., Proceedings of the National Academy of Sciences of the United States of America, 2005. **102**: p. 14503.

17. X. D. Li, H.S.H., C. J. Murphy, K. K. Caswell, Nano Letters, 2003. **3**: p. 1495.
18. Salvetat, J.-P., et al., *Elastic and Shear Moduli of Single-Walled Carbon Nanotube Ropes.* Physical Review Letters, 1999. **82**(5): p. 944.
19. Ghani, T., et al. *A 90nm high volume manufacturing logic technology featuring novel 45nm gate length strained silicon CMOS transistors*. in *Electron Devices Meeting, 2003. IEDM '03 Technical Digest. IEEE International*. 2003.
20. Patton, G.L., et al., *Silicon-germanium base heterojunction bipolar transistors by molecular beam epitaxy.* Electron Device Letters, IEEE, 1988. **9**(4): p. 165-167.
21. Fishbane P.M., G.S., Thornton S.T., Physics, For Scientists And Engineers, 1996. **2nd Edition**: p. 723-741.
22. Fishbane P.M., G.S., Thornton S.T., Physics, For Scientists And Engineers, 1996. **2nd Edition**: p. 731.
23. Niemann, J., *Electrical Measurement On Nanoscale Materials.* Keithley Inc., 2005.
24. Keblinski, P., Phillpot, S. R., Choi, S. U. S., Eastman, J. A., International Journal of Heat and Mass Transfer, 2002(45): p. 855.
25. Zaluska, A., Zaluski, L., Strom-Olsen, J. O., Journal of Alloys and Compounds, 1999(288): p. 217.
26. Brust, M., Kiely, C., J. Colloids and Surfaces a-Physicochemical and Engineering Aspects, 2002(202): p. 175.
27. Ke, Y.C., Long, C. F., Qi, Z. N., Journal of Applied Polymer Science, 1999(71): p. 1139.
28. Shipway, A.N., Katz, E., Willner, I., Chemphyschem, 2000. **1**(18).
29. Han, J.H., et al., *Nano-electromechanical zero-dimensional freestanding nanogap actuator*, in *IEEE International Conference on Micro Electro Mechanical Systems*2011. p. 1357-1360.
30. Moreira, H., et al., *Electron transport in gold colloidal nanoparticle-based strain gauges.* Nanotechnology, 2013. **24**(9): p. 095701.
31. Huth, M., *Granular metals: From electronic correlations to strain-sensing applications.* Journal of Applied Physics, 2010. **107**(11): p. 113709-7.
32. Herrmann, J., et al., *Nanoparticle films as sensitive strain gauges.* Applied Physics Letters, 2007. **91**(18): p. 183105.
33. Vossmeyer, T., et al., *Networked Gold-Nanoparticle Coatings on Polyethylene: Charge Transport and Strain Sensitivity.* Advanced Functional Materials, 2008. **18**(11): p. 1611-1616.
34. Yin, J., et al., *Molecularly Mediated Thin Film Assembly of Nanoparticles on Flexible Devices: Electrical Conductivity versus Device Strains in Different Gas/Vapor Environment.* ACS Nano, 2011. **5**(8): p. 6516-6526.
35. Hosogi, M., et al. *Electro-Mechanical Measurement of Nano Wires -Evaluation of Lambda DNA Wire Coated with Palladium Nano Particles*. in *Solid-State Sensors, Actuators and Microsystems Conference, 2007. TRANSDUCERS 2007. International*. 2007.
36. Wilk, G.D., Wallace, R. M., Anthony, J. M., Journal of Applied Physics, 2001. **89**.
37. Dimitrakopoulos, C.D., Malenfant, P. R. L., Advanced Materials 2002. **14**.
38. Hempel, M., et al., *A Novel Class of Strain Gauges Based on Layered Percolative Films of 2D Materials.* Nano Letters, 2012. **12**(11): p. 5714-5718.

39. Liwei, L., A.P. Pisano, and R.T. Howe, *A micro strain gauge with mechanical amplifier.* Microelectromechanical Systems, Journal of, 1997. **6**(4): p. 313-321.
40. Fraga, M.A., et al., *Effect of nitrogen doping on piezoresistive properties of a-Si x C y thin film strain gauges.* Microsystem Technologies, 2010. **16**(6): p. 925-930.
41. Biasotti, M., Pellegrino, L., Bellingeri, E., Manca, N., Siri A.S., Marre, D., *Strain responce of $La_{0.7}Sr_{0.3}CoO_3$ thin films probed by $SrTiO_3$ crystalline microcantilevers.* Applied Physics Letters, 2012. **97**.
42. Liu, K.H., et al., *In situ probing mechanical properties of individual tungsten oxide nanowires directly grown on tungsten tips inside transmission electron microscope.* Applied Physics Letters, 2006. **89**(22): p. 221908.
43. Nam, C.-Y., et al., *Diameter-Dependent Electromechanical Properties of GaN Nanowires.* Nano Letters, 2006. **6**(2): p. 153-158.
44. Lipomi, D.J., Vosgueritchian, M., Tee, B. C. K., Hellstrom, S. L., Lee, J. A.. Fox, C. H., Bao, Z., *Skin-like pressure and strain sensors based on transparent elastic films of carbon nanotubes.* Nature Nanotechnology, 2011. **6**(12): p. 788-792.
45. Lee, D., et al., *Microfabrication and characterization of spray-coated single-wall carbon nanotube film strain gauges.* Nanotechnology, 2011. **22**(45): p. 455301.
46. Yamada, T., Hayamizu, Y., Yamamoto, Y., Yomogida, Y., Izadi-Najafabadi, A., Futaba, D. N., Hata, K., *A stretchable carbon nanotube strain sensor for human-motion detection.* Nature Nanotechnology, 2011. **6**(5): p. 296-301.
47. Yamada, T., Yamamoto, Y., Hayamaizu, Y., Sekiguchi, A., Hiroyuki, T., Kobashi, K., Futaba, D. N., Hata, K., *Torsion-Sensing Material from Aligned Casrbon Nanotubes Wound onto a Rod Demonstrating Wide dynamic Range.* ACS nano, 2013. **7**(4): p. 3177-3182.
48. Chun, K.Y., Oh, Y., Rho, J., Ahn, J. H., kim, Y.J., Choi, R., Baik, S., *Highly conductive, printable and stretchable composite films of carbon nanotubes and silver.* Nature Nanotechnology, 2010. **5**: p. 853-857.
49. Liu, N., et al., *Electrospun PEDOT:PSS-PVA nanofiber based ultrahigh-strain sensors with controllable electrical conductivity.* Journal of Materials Chemistry, 2011. **21**(47): p. 18962-18966.
50. Xiao, X., et al., *High-Strain Sensors Based on ZnO Nanowire/Polystyrene Hybridized Flexible Films.* Advanced Materials, 2011. **23**(45): p. 5440-5444.
51. Xu, F. and Y. Zhu, *Highly Conductive and Stretchable Silver Nanowire Conductors.* Advanced Materials, 2012. **24**(37): p. 5117-5122.
52. Bae, S.-H., Lee, Y., Sharma, B.K., Lee, H-J., Kim, J-H., Ahn, J-H., *Graphene-based transparent strain sensor.* Carbon, 2013. **51**(0): p. 236-242.
53. C., K., *Introduction to solid state physics/Charles Kittel.* New York, Wiley, 1976: p. 89-218.
54. Fu, X.-W., et al., *Strain dependent resistance in chemical vapor deposition grown graphene.* Applied Physics Letters, 2011. **99**(21): p. 213107-213107-3.
55. Yu, Z., et al., *Intrinsically Stretchable Polymer Light-Emitting Devices Using Carbon Nanotube-Polymer Composite Electrodes.* Advanced Materials, 2011. **23**(34): p. 3989-3994.
56. Zhang, Y., et al., *Polymer-Embedded Carbon Nanotube Ribbons for Stretchable Conductors.* Advanced Materials, 2010. **22**(28): p. 3027-3031.
57. Sekitani, T., et al., *Stretchable active-matrix organic light-emitting diode display using printable elastic conductors.* Nat Mater, 2009. **8**(6): p. 494-499.

58. Shin, M.K., et al., *Elastomeric Conductive Composites Based on Carbon Nanotube Forests.* Advanced Materials, 2010. **22**(24): p. 2663-2667.
59. Kim, K.H., M. Vural, and M.F. Islam, *Single-Walled Carbon Nanotube Aerogel-Based Elastic Conductors.* Advanced Materials, 2011. **23**(25): p. 2865-2869.
60. Yu, Z., et al., *Highly Flexible Silver Nanowire Electrodes for Shape-Memory Polymer Light-Emitting Diodes.* Advanced Materials, 2011. **23**(5): p. 664-668.
61. Yun, S., et al., *Compliant Silver Nanowire-Polymer Composite Electrodes for Bistable Large Strain Actuation.* Advanced Materials, 2012. **24**(10): p. 1321-1327.
62. Yang, P., R. Yan, and M. Fardy, *Semiconductor Nanowire: What's Next?* Nano Letters, 2010. **10**(5): p. 1529-1536.
63. Nirmalraj, P.N., et al., *Manipulating Connectivity and Electrical Conductivity in Metallic Nanowire Networks.* Nano Letters, 2012. **12**(11): p. 5966-5971.
64. Li, Y., et al., *Dopant-Free GaN/AlN/AlGaN Radial Nanowire Heterostructures as High Electron Mobility Transistors.* Nano Letters, 2006. **6**(7): p. 1468-1473.
65. Wu, W., Y. Wei, and Z.L. Wang, *Strain-Gated Piezotronic Logic Nanodevices.* Advanced Materials, 2010. **22**(42): p. 4711-4715.
66. Johnson, J.C., Choi, H-J., Kelly P.S., Richard D., Peidong, Y., Saykally, R. J., *Single gallium nitride nanowire lasers.* nature materials, 2002. **1**(2): p. 106-110.
67. Zhou, J., et al., *Flexible Piezotronic Strain Sensor.* Nano Letters, 2008. **8**(9): p. 3035-3040.
68. Loh, O.Y. and H.D. Espinosa, *Nanoelectromechanical contact switches.* Nat Nano, 2012. **7**(5): p. 283-295.
69. Levitt, A.P., *Whisker Technology.* Wiley-Interscience, 1970.
70. McAlpine, M.C., et al., *High-Performance Nanowire Electronics and Photonics on Glass and Plastic Substrates.* Nano Letters, 2003. **3**(11): p. 1531-1535.
71. Yan, R., Gargas, D., Yang, P., *Nanowire photonics.* Nature Photonics, 2009. **3**(10): p. 569-576.
72. Agrawal, R. and H.D. Espinosa, *Giant Piezoelectric Size Effects in Zinc Oxide and Gallium Nitride Nanowires. A First Principles Investigation.* Nano Letters, 2011. **11**(2): p. 786-790.
73. Minary-Jolandan, M., et al., *Individual GaN Nanowires Exhibit Strong Piezoelectricity in 3D.* Nano Letters, 2011. **12**(2): p. 970-976.
74. Espinosa, H.D., R.A. Bernal, and T. Filleter, *In Situ TEM Electromechanical Testing of Nanowires and Nanotubes.* Small, 2012. **8**(21): p. 3233-3252.
75. Espinosa, H.D., R.A. Bernal, and M. Minary-Jolandan, *A Review of Mechanical and Electromechanical Properties of Piezoelectric Nanowires.* Advanced Materials, 2012. **24**(34): p. 4656-4675.
76. Morkoc, H., *Handbook of Nitride Semiconductors and Devices.* Wiley-VCH, Germany, 2008. **1**.
77. Kiener, D. and A.M. Minor, *Source Truncation and Exhaustion: Insights from Quantitative in situ TEM Tensile Testing.* Nano Letters, 2011. **11**(9): p. 3816-3820.
78. Huang, J.Y., et al., *In Situ Nanomechanics of GaN Nanowires.* Nano Letters, 2011. **11**(4): p. 1618-1622.
79. Huang, J.Y., et al., *In Situ Observation of the Electrochemical Lithiation of a Single SnO2 Nanowire Electrode.* Science, 2010. **330**(6010): p. 1515-1520.

80. Asthana, A., et al., *In situ observation of size-scale effects on the mechanical properties of ZnO nanowires.* Nanotechnology, 2011. **22**(26): p. 265712.
81. Guo, H., et al., *Mechanics and Dynamics of the Strain-Induced M1–M2 Structural Phase Transition in Individual VO2 Nanowires.* Nano Letters, 2011. **11**(8): p. 3207-3213.
82. Bernal, R.A., et al., *Effect of Growth Orientation and Diameter on the Elasticity of GaN Nanowires. A Combined in Situ TEM and Atomistic Modeling Investigation.* Nano Letters, 2010. **11**(2): p. 548-555.
83. Zhu, Y. and H.D. Espinosa, *An electromechanical material testing system for in situ electron microscopy and applications.* Proceedings of the National Academy of Sciences of the United States of America, 2005. **102**(41): p. 14503-14508.
84. Zhu, Y., N. Moldovan, and H.D. Espinosa, *A microelectromechanical load sensor for in situ electron and x-ray microscopy tensile testing of nanostructures.* Applied Physics Letters, 2005. **86**(1): p. 013506.
85. Espinosa, H.D., Y. Zhu, and N. Moldovan, *Design and Operation of a MEMS-Based Material Testing System for Nanomechanical Characterization.* Microelectromechanical Systems, Journal of, 2007. **16**(5): p. 1219-1231.
86. Yong, Z., C. Alberto, and D.E. Horacio, *A thermal actuator for nanoscale in situ microscopy testing: design and characterization.* Journal of Micromechanics and Microengineering, 2006. **16**(2): p. 242.
87. Yong, Z., et al., *Piezoresistivity Characterization of Synthetic Silicon Nanowires Using a MEMS Device.* Microelectromechanical Systems, Journal of, 2011. **20**(4): p. 959-967.
88. Mario, K., M. Shinji, and I. Yoshitada, *The piezoresistance effect of FIB-deposited carbon nanowires under severe strain.* Journal of Micromechanics and Microengineering, 2008. **18**(6): p. 065011.
89. Han, J.H. and M.T.A. Saif, *In situ microtensile stage for electromechanical characterization of nanoscale freestanding films.* Review of Scientific Instruments, 2006. **77**(4): p. 045102.
90. Espinosa, H.D., Bernal R. A., *Microelectromechanical Device and System.* WO 2011/053346 A1, 2011.
91. Yang, Q., et al., *Enhancing Sensitivity of a Single ZnO Micro-/Nanowire Photodetector by Piezo-phototronic Effect.* ACS Nano, 2010. **4**(10): p. 6285-6291.
92. WangWang, et al., *Piezoelectric Field Effect Transistor and Nanoforce Sensor Based on a Single ZnO Nanowire.* Nano Letters, 2006. **6**(12): p. 2768-2772.
93. Hongjiang, Z., et al., *In situ SEM electromechanical characterization of nanowire using an electrostatic tensile device.* Journal of Physics D: Applied Physics, 2013. **46**(30): p. 305501.
94. Minary-Jolandan, M., R.A. Bernal, and H.D. Espinosa, *Strong piezoelectricity in individual GaN nanowires.* MRS Communications, 2011. **1**(01): p. 45-48.
95. Zhao, M.-H., Z.-L. Wang, and S.X. Mao, *Piezoelectric Characterization of Individual Zinc Oxide Nanobelt Probed by Piezoresponse Force Microscope.* Nano Letters, 2004. **4**(4): p. 587-590.
96. Yun, W.S., et al., *Ferroelectric Properties of Individual Barium Titanate Nanowires Investigated by Scanned Probe Microscopy.* Nano Letters, 2002. **2**(5): p. 447-450.

97. Wang, Z., J. Hu, and M.-F. Yu, *One-dimensional ferroelectric monodomain formation in single crystalline BaTiO[sub 3] nanowire.* Applied Physics Letters, 2006. **89**(26): p. 263119-3.
98. Wang, J., et al., *Ferroelectric domains and piezoelectricity in monocrystalline Pb(Zr,Ti)O[sub 3] nanowires.* Applied Physics Letters, 2007. **90**(13): p. 133107-3.
99. Wang, J., et al., *Piezoresponse force microscopy on doubly clamped KNbO[sub 3] nanowires.* Applied Physics Letters, 2008. **93**(22): p. 223101-3.
100. Feng, X., et al., *Stretchable Ferroelectric Nanoribbons with Wavy Configurations on Elastomeric Substrates.* ACS Nano, 2011. **5**(4): p. 3326-3332.
101. Ke, T.-Y., et al., *Sodium Niobate Nanowire and Its Piezoelectricity.* The Journal of Physical Chemistry C, 2008. **112**(24): p. 8827-8831.
102. Fan, H.J., et al., *Template-Assisted Large-Scale Ordered Arrays of ZnO Pillars for Optical and Piezoelectric Applications.* Small, 2006. **2**(4): p. 561-568.
103. Scrymgeour, D.A. and J.W.P. Hsu, *Correlated Piezoelectric and Electrical Properties in Individual ZnO Nanorods.* Nano Letters, 2008. **8**(8): p. 2204-2209.
104. Bin Wu, A.H., John J. Boland, John E. Sader, XiaoMing Sun, YaDong Li, *Microstructure-Hardened Silver nanowires.* Nanoletters, 2006. **6**(3): p. 468-472.
105. Heidelberg, A., et al., *A Generalized Description of the Elastic Properties of Nanowires.* Nano Letters, 2006. **6**(6): p. 1101-1106.
106. Wang, Z.L. and J. Song, *Piezoelectric Nanogenerators Based on Zinc Oxide Nanowire Arrays.* Science, 2006. **312**(5771): p. 242-246.
107. Xu, X., et al., *An improved AFM cross-sectional method for piezoelectric nanostructures properties investigation: application to GaN nanowires.* Nanotechnology, 2011. **22**(10): p. 105704.
108. Toriyama, T., D. Funai, and S. Sugiyama. *Electro-mechanical properties of single crystal silicon nano wire*. in *Nanotechnology, 2001. IEEE-NANO 2001. Proceedings of the 2001 1st IEEE Conference on*. 2001.
109. Cao, J., Q. Wang, and H. Dai, *Electromechanical Properties of Metallic, Quasimetallic, and Semiconducting Carbon Nanotubes under Stretching.* Physical Review Letters, 2003. **90**(15): p. 157601.

Chapter 2: Equipment and Methods

In this chapter the equipment and methods used to perform the experiments throughout the thesis are described.

2.1. Electron microscopy

Electron microscopes are powerful tools that can be used in a wide variety of applications, ranging from imaging the interior structure of biological cells[1] to obtaining detailed crystallographic information on nano-sized objects[2].

The driving force behind the development of the electron microscope was the limited resolution of the light microscope. If we apply the classic Rayleigh criterion for the resolution of a light microscope, we find that the smallest distance that can be resolved is approximately half of the wavelength of the radiation, which equates to an optical resolution ~200 nm. To overcome these difficulties electron microscopes were invented. Louie de Broglie theorised that the electron had wave like characteristics in 1925[3]. This was demonstrated in 1927 by electron diffraction experiments[4]. Only a few years later in 1931 the first electron microscope was reported[5]. By referring to Louie de Broglie's equation linking wavelength of electrons, λ, and their energy, E, we expect the following relationship: $\lambda = 1.22/E_{1/2}$ with λ in *nm* and E in *eV*. Most SEMs function between 0.5 and 30 *kV*. The higher voltages theoretically provide sub-nanometric resolution (0.2 *nm*). However imperfections in electron lenses make this limit almost unachievable. Nevertheless state-of-the-art microscopes can routinely achieve nanometre resolution.

In addition to scanning probe microscopy (SPM) methods, electron based microscopy (EM) was widely used in this work. Not only is EM a useful tool for visualising nanomaterials, as in transmission electron microscopy (TEM), but also as a fabrication tool in processes such as electron beam lithography (EBL). In this thesis a suite of Carl Zeiss SEMs were used. These include the Zeiss Supra, Auriga and Ultra. The Zeiss Supra was the SEM most heavily used in this work.

2.1.1. *Scanning Electron Microscope*

SEM operates in an almost identical principal to optical microscopes, except electrons are used rather than photons. The SEM generates a beam of electrons, from an electron source called the "gun", that are scanned across the surface in a raster motion. The beam is collimated by a series of electromagnetic lenses. Condenser lenses collimate the electrons on exiting the gun into a parallel beam, allowing the objective lens to focus the beam. Electromagnetic coils raster the beam across the sample. Figure 1 shows a schematic of the SEM electron column.

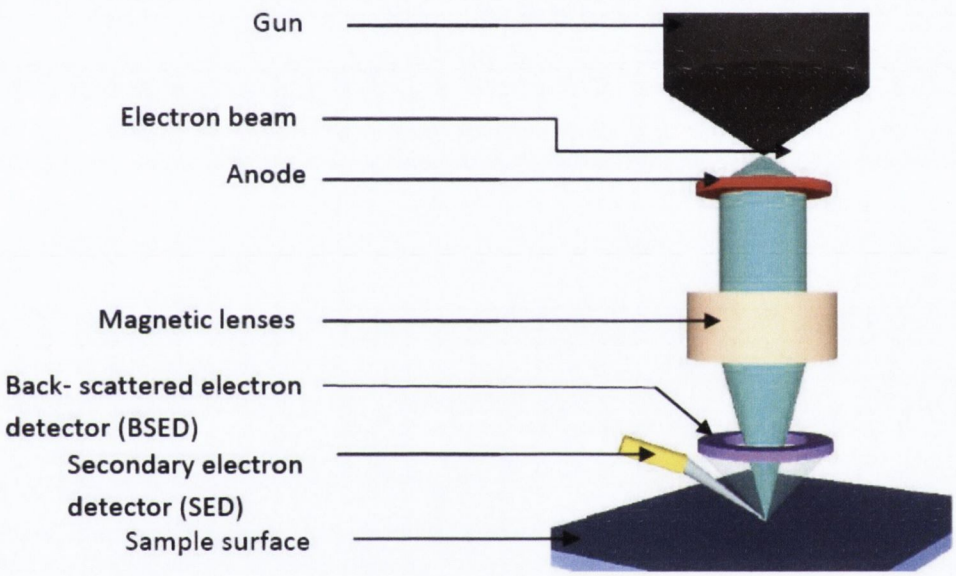

Figure 1: Schematic representation of a SEM column. The major features along the column are labelled.

SEM systems must operate under vacuum. Generally, the chamber pressure under operation is 10^{-6} *mbar* and gun vacuum 10^{-9} *mbar*. The chamber contains the stage, sample and all the detectors used to form an image. The gun acts as the source of electrons. There are three types of electron sources used; Tungsten, Lanthanum hexaboride (LaB_6) and Field Emission Gun (FEG). The most important characteristic of the electron source is brightness. Brightness is directly related to the current density and ultimately determines the contrast, resolution and signal-to-noise capabilities of the microscope.

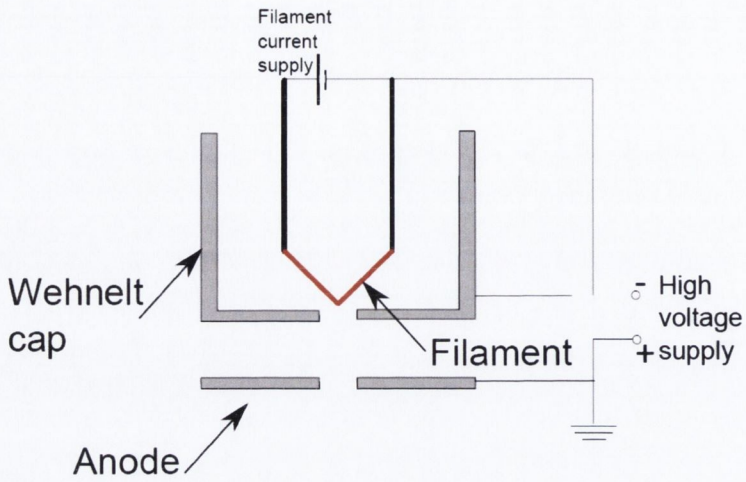

Figure 2: Schematic of the working principal of a LaB_6 electron source and tungsten electron source

Tungsten and LaB_6 sources work in a very similar way. A current is passed through the cathode generating electrons through thermionic emission. These electrons are then attracted by the anode situated below the filament to generate the beam. Figure 2 shows a schematic representation of the operating principal of a LaB_6 and tungsten source. FEG works in a completely different way but provide by far the highest resolution, hence they are most often found as TEM sources. The principal of FEG is based on electron tunnelling. The gun is constructed of a very sharp tungsten tip onto which an extremely high negative voltage (up to 3 *kV* as in TEM) is applied with respect to a nearby electrode. The high field collapses the barrier to emission and tunnelling becomes possible resulting in electrons emitted from the metal tip, that travel down the column where they can be utilised for imaging, analysis or lithographic purposes. Table 1 shows a comparison of the different source characteristics.

Table 1: Comparison of characteristics for three different electron sources

	Brightness ($A/cm^2.sr$)	**Source size**	**Energy spread** (eV)	**Vacuum** ($mbar$)
Tungsten	$x\ 10^5$	25 μm	2 – 3	$x\ 10^{-6}$
LaB_6	$x\ 10^6$	10 μm	2 – 3	$x\ 10^{-8}$
FEG	$x\ 10^9$	5 nm	0. 22	$x\ 10^{-9}$

Image formation in SEM is dependent on the acquisition of signals from electron sample interactions. When the incident electron beam reaches the surface, several electron-solid interactions take place below the surface, forming a pear shaped excitation volume, shown in figure 3. These interactions can be elastic or inelastic in nature. Elastic scattering occurs when the incident electrons are deflected by the atomic nucleus or core shell electrons of the atoms in the solid. The interaction results in negligible energy loss but results in a large change in the angle of trajectory. Electrons that are scattered more than 90° are called back scattered electrons (BSE) and are used for image formation. BSE are highly dependent on the atomic number of the atom they interact with, therefore compositional information can be garnered from the image.

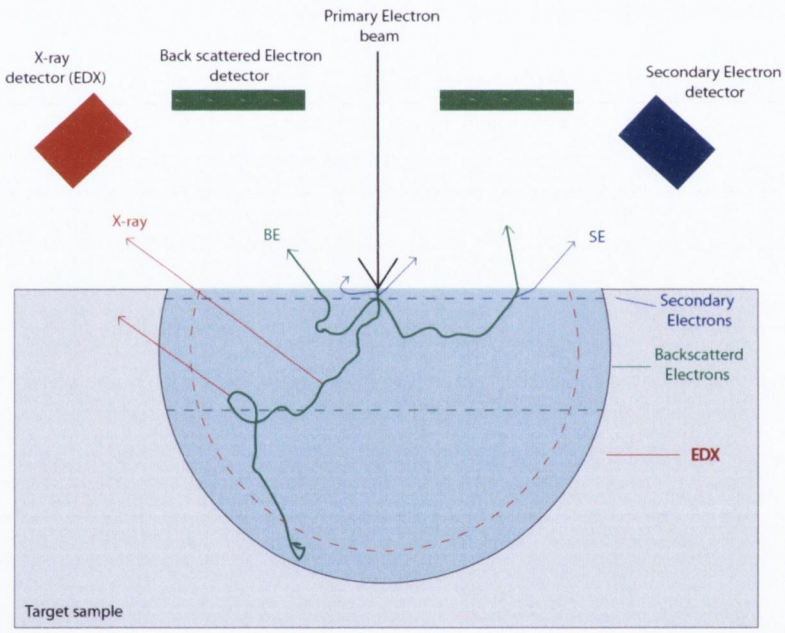

Figure 3: Schematic showing the various incident electron beam interactions with the sample

Secondary electrons are produced when the incident electron excites an electron in an atom of the sample losing its energy in the process. The excited electron under goes further elastic and inelastic collisions until it reaches the surface where it can escape if it has sufficient energy. Given their low energy (~ 10 *eV*), only secondary electrons near the surface, within 20 *nm*, contribute to image formation. At the higher end of the energy spectrum X-rays are produced deep within the interaction volume from the excitation of core shell electrons and the subsequent relaxation of

core holes. X-ray detectors can be placed within the column and can be used for qualitative elemental analysis.

The beam acceleration voltage in SEM is generally between 0. 2 *kV* to 30 *kV*. For most common samples an acceleration voltage of 5 *kV* is used. This is a compromise between good resolution and low signal to noise.

2.1.2. Transmission Electron Microscope (TEM)

The first electron microscope invented by Ruska *et al* [5] was a transmission electron microscope (TEM). Fundamentally TEM is different from SEM as images are formed using transmitted electrons that pass through the sample, rather than back scattered and secondary electrons detected in SEM. Specimens must be very thin for electrons to pass through them. The first high resolution breakthrough in TEM came in the 1950s with the development of thinning techniques for metal foils down to electron transparent thickness, and the development of diffraction contrast theory[6]. In TEM, electrons are sourced from the gun, accelerated down the column through the specimen and converged by a series of lenses onto a detector or screen. Therefore the thickness of the sample is of paramount importance for the quality of the image. The requirement to get enough electrons transmitted through the sample is a function of beam electron energy and atomic number of the specimen. Using high *kV* acceleration voltages allows for thicker samples to be imaged but causes greater beam damage. High resolution TEM (HRTEM) requires samples to be less than 100 *nm* thick. Producing very thin specimens can be achieved by grinding the bulk material using a grinding tool and electro-polishing or by ion milling a thin slice, known as a lamella, from the surface of the material. TEM lamellas are produced using focused ion beam (FIB) milling at various beam currents.

TEMs operate at very high acceleration voltages (80 *kV* to 3 *MV*). However, operating at such high voltages can rapidly cause beam damage to the specimen. Generally TEM's are used at acceleration voltages between 200 – 400 *kV* giving the best resolution while minimizing beam damage, although beam damage is generally inevitable when using high electron doses in small areas. There are two main operating modes of TEM; imaging and diffraction.

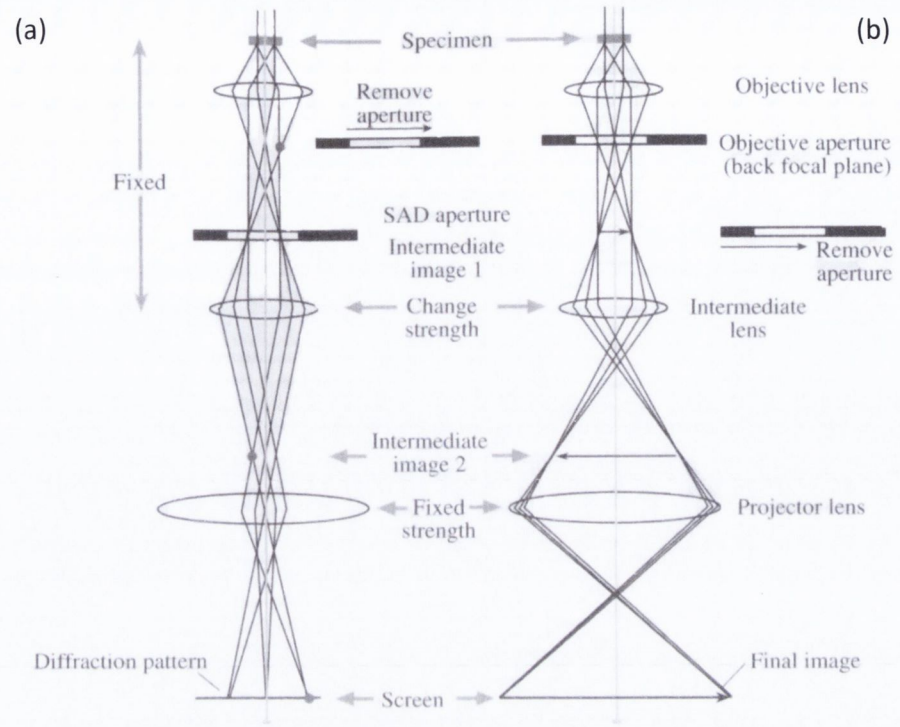

Figure 4: Schematic showing the beam orientation in TEM. (a) diffraction imaging mode and (b) imaging mode.

Figure 4 shows a schematic representation of the beam orientation and lens selection for both diffraction, (a) and imaging, (b), operating modes of the TEM. The objective lens is the first lens the beam encounters after passing through the specimen. The objective lens forms the diffraction pattern. Depending on the position and strength of the intermediate lens, the back focal plane or imaging plane from the objective lens can be selected. The insertion of a Selected Area Diffraction (SAD) aperture allows the user to select a specific area of the specimen to contribute to the diffraction pattern. This is extremely useful to study NWs as the dimensions of the specimen are small.

The principal advantage of TEM over other electron microscopy methods is its resolution. By applying the Rayleigh criteria at 100 keV, described earlier for the SEM, the wavelength is 4 pm, hence a resolution of 2pm is theoretically possible. Unfortunately this is not the case because of imperfect electron lenses. However, the resolution of TEM has been dramatically improved in the last few years mainly due

to breakthrough in spherical and chromatic aberration corrected TEMs. Therefore the improvement of electron lenses and the use of higher voltages led to the development of HRTEM, allowing the visualisation of columns of atoms in crystals.

We have established the importance of having extremely thin specimens. Such thin and delicate samples must be mounted on support frames, known as TEM grids, in order to image them in a TEM. There are a number of different types of grids depending on the application. Most commonly lacey carbon grids are used. Lacey carbon grids are constructed of a thin copper support frame (100 μm thick) covered on one side with an amorphous carbon layer (50 nm), figure 5. Lamellas are placed onto the grid using a micromanipulator and tip.

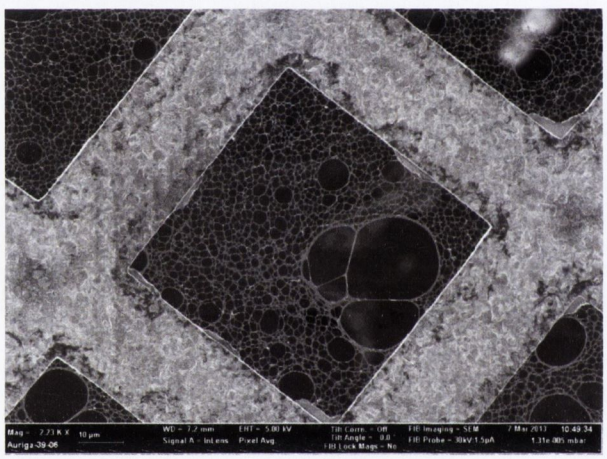

Figure 5: SEM image of a lacey carbon TEM grid

Grids can also be made from silicon nitride or silicon dioxide. Generally, this type of grid consists of a 200 μm support frame with a perforated SiN membrane covering a square 500 x 500 μm area at the centre of the grid. A range of different membrane thicknesses, perforation dimension, and pitch can be purchased. For example, SiN grids are suitable for mechanical measurements as they provide a rigid support for nano-entities. There are also copper horse shoe type grids available. With this type of support-mount lamella must be attached at particular positions along the inner region of the grid. There is no support film, the specimen is supported at one edge by EBID deposited material. The advantage of the latter type of grid is the ability to refine the specimen thickness after it is mounted onto the grid, avoiding the need to manipulate the delicate specimen after fine thinning. Further thinning can also be performed if necessary.

Similar to SEM, when electrons interact with the specimen in TEM they can be elastically or inelastically scattered. Elastic scattering is generally coherent with the incident beam at scattering angles < 10°. Scattering events > 10° are incoherent and all inelastic events are incoherent. Scattering effects increase with greater specimen thickness and decrease at increased acceleration voltages. For thin samples, single scattering events are most common as the mean free path of an electron accelerated at TEM voltages are of the order of tens of *nm*.

In TEM the beam can be rastered across the specimen similar to that of SEM. This application is known as Scanning-TEM (STEM). In STEM mode the electron beam is formed into a fine point probe and scanned across the specimen, in contrast to TEM where the beam is parallel. As in SEM, secondary and backscattered electrons are produced. Both the transmitted and non-transmitted electrons can be probed by multiple detectors providing the maximum amount of information from each scan. Figure 6 shows the lens and detector arrangement of a dedicated STEM system[7]. It is similar to the TEM arrangement but a set of scanning coils focus and raster the beam before specimen interaction.

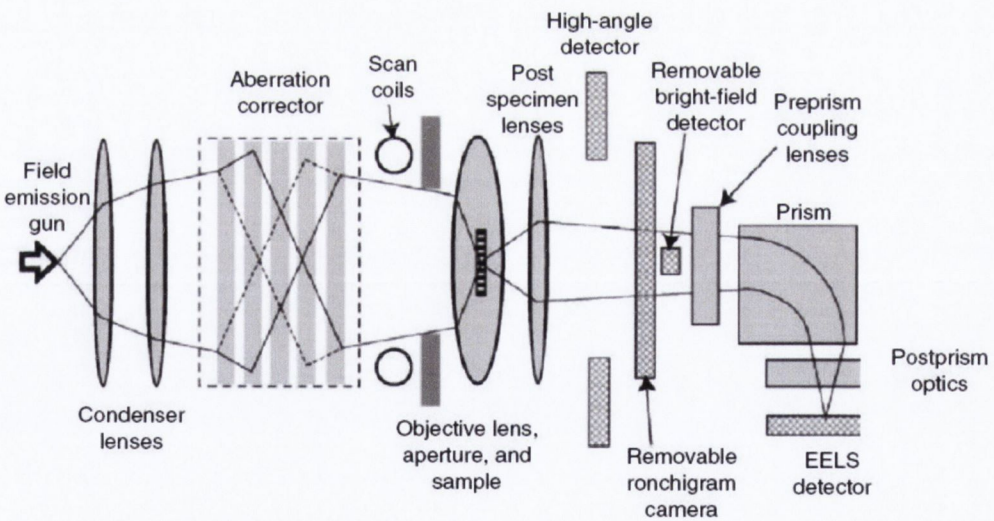

Figure 6: Schematic image of the set up for a stand-alone STEM system [22]

STEM can be utilised to provide qualitative characterisation on single nano-entities such as crystal structure, morphology and composition. High resolution Energy Dispersive X-ray (EDX) spectroscopy and Electron Energy Loss Spectroscopy (EELS) can be performed using STEM providing accurate local compositional characterisation.

To achieve high resolution in TEM a quantitative understanding of diffraction is essential. Crystalline materials produce an array of dots that are indicative of the crystal structure. Poly-crystalline materials produce an array of rings that are separated by specific distances depending on the structure. An amorphous material will produce a diffuse halo. It is important to understand that diffraction data is a representation of structure in reciprocal space. For example, in a crystalline solid a dot on the diffraction pattern represents a row of atoms in real space. Obtaining accurate diffraction data can give the entire crystal structure of the solid.

TEM was used extensively throughout this work to characterise NW and obtain both quantitative and qualitative information on material sets.

2.2. Electron Beam Lithography (EBL)

Electron microscopes can be utilised to perform high resolution lithography. This process is known as Electron Beam Lithography (EBL). EBL was invented in the 1960s [8] and reduced the dimensions of microelectronics to the nanoscale. As early as 1976 sub 10 *nm* features were realised using EBL[9]. EBL has a distinct advantage over optical techniques as smaller feature size can be routinely achieved. Interest in EBL has since extended beyond the semiconductor industry to an interdisciplinary field encompassing biology, chemistry, engineering and physics.

EBL involves irradiating a substrate with electrons in a particular pattern, the substrate being covered in an electron sensitive thin film, known as a "resist". When electrons bombard the resist material its chemical composition is altered in a specific way. For example, for a polymer based resist the bonds within the polymer chains may either break or cross link when irradiated with electrons, depending on the desired application. There are two types of resist material; positive and negative. In a positive photoresist the area exposed by the electron beam is removed, in a negative resist the area exposed by the beam remains after development. EBL is generally performed using SEM's that have been converted into EBL systems. This involves installing beam blanking plates in the electron column and design software that controls the beam. Designs are drawn using EBL design software, such as Raith. The exact dimensions of the desired device are drawn using separate write layers that can be aligned to other pre-fabricated structures such as UV electrodes. Raith

is a CAD package which saves designs in a GDSII format. The software is specially written for lithographic applications and allows the user to align to pre-fabricated features and chose write fields to fit the desired device dimensions. The beam step size is directly dependent on the write field, amongst other parameters such as beam current.

Before samples are exposed they must be prepared. This involves a thorough cleaning to remove any contaminants that may have accumulated on the surface. The type of resist, negative or positive, is chosen depending on the desired application. For example, a concentrated positive resist is more suitable for metal deposition. The concentration of the resist is very important, directly affecting the thickness and ultimately the resolution that can be achieved. The thickness can also be tuned by altering the spin coating process by which the resist is cast onto the substrate. Typical resist thicknesses for EBL range between 5 – 1000 *nm* depending on the fabrication requirements.

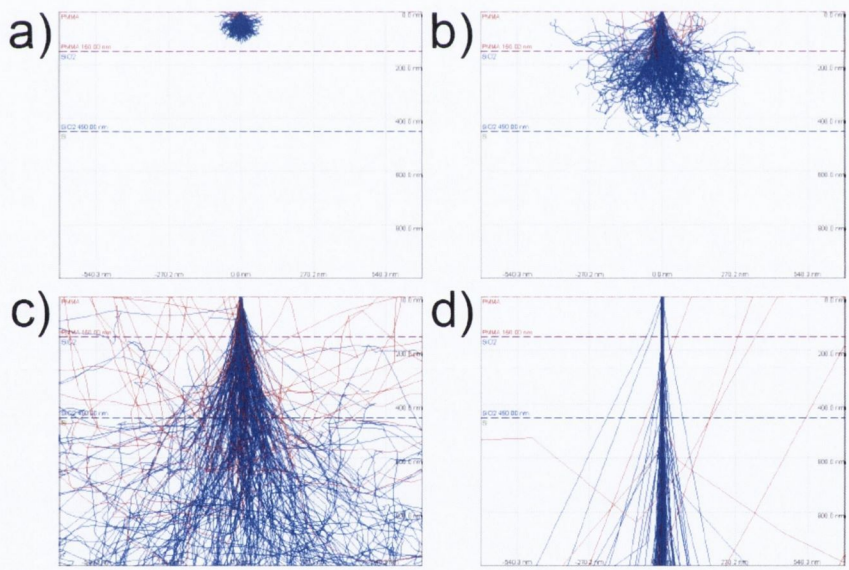

Figure 7: Casino calculations showing the penetration depth of the e-beam at various energies into a PMMA covered SiO_2/Si substrate. (a) 2 keV acceleration voltage, (b) 5 keV acceleration voltage, (c) 15 keV acceleration voltage and (d) 100 keV acceleration voltage.

As was discussed extensively in previous sections, electron-specimen interactions are very important. Back scattered (BSE) and secondary electrons (SE) can cause unpredictable exposure doses, known as the proximity effect[10]. The degree of BSE and SE is dependent on the energy of the impingent electrons on the surface. As

electrons pass through the resist forward scattering events are most common. This can result in positive effects, such as resist undercut which is ideal for metal deposition, as well as negative effects such as over-exposure and feature blurring. SE have energies between 2 – 100 *eV*. SE expose the resist, for example in PMMA secondary electrons break the molecular backbone of the PMMA chains allowing them to be removed on development. The impingent electron energy is controlled by the acceleration voltage. A high acceleration voltage will have the smallest interaction area with resist. This is ideal for small features, but requires a large dose which has other implications such as increasing the exposure time. The electron interaction depth into the specimen can be modelled at different acceleration voltages. Figure 7 displays electron scattering trajectories using CASINO simulation package[11, 12].

For simulation purposes, the sample was chosen to be 150 *nm* PMMA resist on 300 *nm* SiO_2 substrate with silicon bulk beneath. Each simulation shows an area 1 μm into the specimen. Figure 7 (a) has an acceleration voltage of 2 *keV*. At this energy the electrons do not penetrate through the PMMA film and would not be useful for EBL. A 5 *keV* acceleration voltage is shown in figure 7 (b). The electrons pass through the resist, but there is a large interaction volume which would make fine features unattainable at this electron energy. Figure 7 (c) represents a 15 *keV* acceleration voltage, suitable for EBL. The beam fully penetrates the resist with a little undercut shown from the beam spread at the PMMA/SiO_2 interface. Specialist EBL systems can use acceleration voltages up to 100 *keV*, figure 7 (d). There is minimal undercut as the beam linearly passes through the resist with little scatter.

The resist is exposed at a particular acceleration voltage and dose. The dose is comprised of the beam dwell time, step size and beam current. The dwell time is the amount of time the beam resides at a particular point. The step size is the distance the beam moves between each pixel and beam current is the current of the impingent electron beam. The acceleration voltage and aperture size control the beam current. The aperture controls the magnitude of the source beam that is allowed to interact with the specimen by excluding electrons outside a certain radius. The dose is user defined and chosen after a series of dose tests are performed.

In this work the SEM used for EBL was a Carl Zeiss Supra SEM. The design software used to fabricate devices was the Raith Elphy Quantum Lithography suite. Either 15 kV or 10 kV acceleration voltages and a 10 μm aperture were used in this work.

2.3. Atomic Force Microscope

The Atomic force Microscope (AFM) and Scanning Tunnelling Microscope (STM) are types of Scanning Probe Microscopy (SPM). STM was invented by Binnig and Roher in 1981[13] and earned them a Nobel Prize in 1986. The AFM was invented the same year by Binnig, Quate and Gerber[14]. In essence, the AFM operates by rastering a sharp tip close to a surface while monitoring the interaction between the tip and the surface via a feedback loop. The raster scanning, tip-surface interaction and feedback loop allow an image of the surface topography to be constructed. Generally tip-surface interaction is dominated by Van der Waals or electrostatic forces, but by careful consideration of the tip it is possible to probe many different types of interaction e.g. electrical, magnetic, electrostatic, thermal and mechanical properties.

2.3.1. Working Principal

Initially Binnig *et al* [14] used a STM tip mounted in contact with the back of an AFM tip to monitor the motion of the AFM tip through feedback, however, in modern AFM the motion of the tip scanning across the surface is detected by a laser beam, usually 1 mW, or Superluminescent Diode (SLD) aligned onto the back of the tip. The beam strikes the tip and is reflected onto a 4-quadrant photodetector (PD) as shown in figure 8. The four-quadrant PD allows the lateral and normal signals to be monitored and recorded simultaneously. From the position of the reflected beam striking the PD the interaction between the tip and the surface can be monitored. AFM has two operating modes: Contact mode and tapping mode, also referred to as dynamic or AC mode. Contact mode is an intrusive imaging technique where the tip intimately scans the surface in a scratching like motion. In this mode feedback is detected from the cantilever deflection. Changes in cantilever deflection are monitored by the 4-quadrant PD, which can detect changes of less than 1 $\AA$. A pre-defined set point is maintained by the feedback loop. Feedback utilises a PID controller (proportional-integral-derivative) which minimizes the error between the signal and the desired

set point. The image is constructed by maintaining the PD set point and moving the tip in the z-direction using the z-piezo stack as the tip moves across the surface. In contact mode, the force applied to the surface by the tip is maintained and is usually on the order of 10^{-9} *N*. The force, F, is calculated from Hooke's Law, $F=-kx$, where k is the spring constant of the cantilever and x is the cantilever deflection.

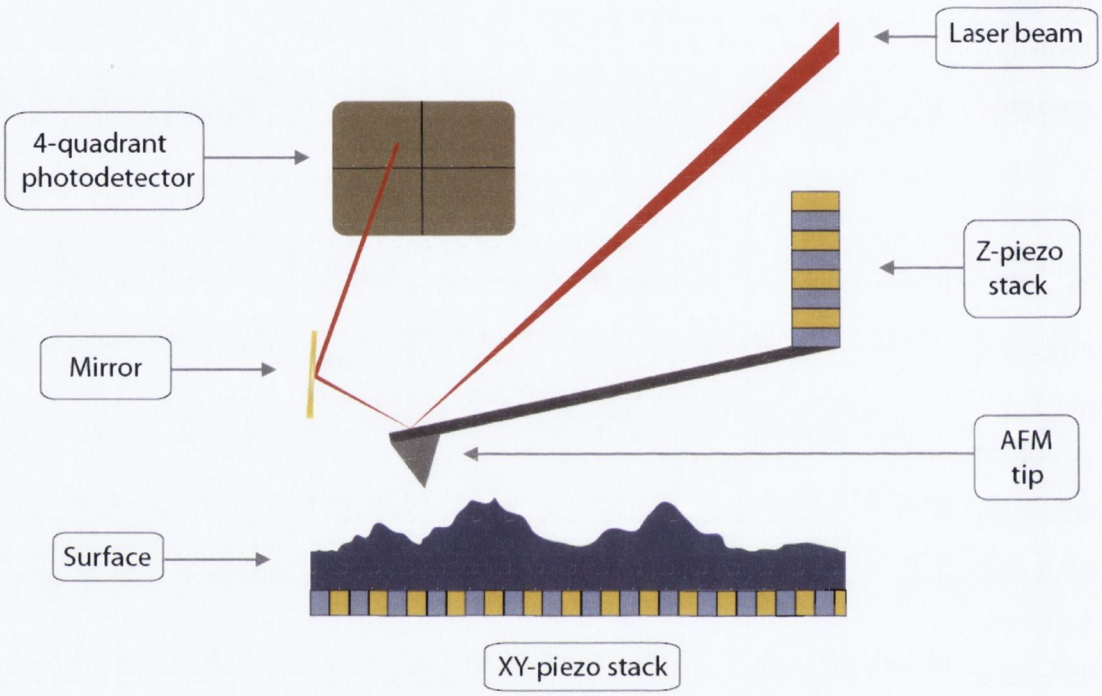

Figure 8: Schematic diagram showing the working principal of an AFM. The tips motion is captured by the photodetector as it scans across the surface providing a topographical image.

In tapping mode the tip is oscillated at constant amplitude (usually between 20 to 100 *nm*) and gently taps across the surface building up a point by point topography image of the surface. In this mode feedback is monitored by the cantilever amplitude and frequency. The feedback loop maintains constant oscillation amplitude by measuring the root mean square of the signal acquired by the PD. The oscillation amplitude is constantly maintained at the predefined "amplitude set point", hence a constant tip-sample interaction is maintained during imaging. The amplitude is maintained by feedback between the PD and z-piezo. As the cantilever amplitude on the PD is dampened or accelerated feedback moves the z-piezo, and hence the tip, up

or down to maintain the amplitude set point. Controlling the set point allows the tip to probe close to, or far from, the surface depending on what information is desired.

Table 2 lists some of the advantages and disadvantages of contact and tapping mode AFM:

Table 2: Comparison of contact mode vs. tapping mode AFM

	Contact mode	***Tapping mode***
Advantages	• High scan speeds • Atomic resolution • Electrical measurements	• High lateral resolution • Low force and less damage to sensitive samples
Disadvantages	• Distortion to image from shear forces • Damage to surface due to scratching • Piezo non-linearities and creep	• Slow scan speed • Piezo non-linearities and creep

2.3.2. Scanners

The AFM scanner is the most important component of any AFM system. The scanner performance will determine the overall reliability of the results that the AFM can provide. Scanners are made from piezoelectric materials that allow accurate movement of the probe along the surface. However, piezoelectric materials are hampered by non-linear characteristics such as trace and re-trace hysteresis and creep. These drawbacks increase the difficulties in achieving high quality images, or completing complex nanomanipulation tasks[15]. Hence, it is important to remove piezoelectric artefacts from the imaging process. Figure 9 (a) shows the effect of piezo creep on image quality. Figure 9 (b) shows the same image with piezo effects

corrected for. Scanners can either scan the tip or scan the stage. The former utilise tube scanners where XY-Z piezo motors are grouped together. Tube scanners suffer from increased non-linear background motion as they are not orthogonal 3D actuators. Scanning the stage and the tip separately decouples the XY and Z piezo. These scanners are known as flexure scanners. Closed loop scanning, which uses a capacitive position sensor, is yet more precise and accurate than open loop scanners. Closed loop systems can achieve spatial positioning within a few nanometres. This is very important for patterning and manipulation type experiments. The AFM used in this work has a closed loop scanner.

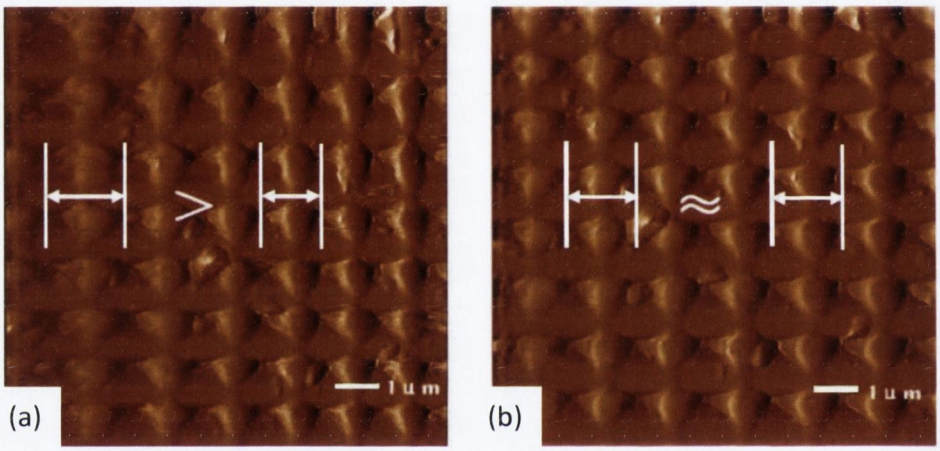

Figure 9: Scanned topographic results of scanning over a periodic calibration grating (a) without hysteresis compensation and (b) with compensation for piezo hysteresis[3]

2.3.3. Probes

The type of probe used depends on the desired measurement. For example, in conductive AFM (C-AFM) metallic probes are required to ensure electrical contact. Generally, there are two types of probes available commercially: silicon nitride and Silicon. Silicon Nitride cantilevers are triangular in shape, figure 10 (a), and exhibit low spring constants between 0.02 N/m to 0.8 N/m. They are generally used for contact and tapping mode imaging in liquid.

Silicon probes are rectangular in shape and exhibit spring constants of up to 50 N/m and are used for contact and tapping mode imaging in air. Both types of tips are available with different coatings depending on the application (magnetic, electrical, chemical, biological etc). The back side of the cantilever may be coated in a metal like aluminium to increase reflectivity; increasing the intensity of the reflected laser

beam. The resonant frequency of the cantilever depends on the physical dimensions. A longer cantilever will decrease the resonant frequency and a shorter cantilever will increase the resonant frequency. Users choose cantilever resonant frequencies depending on whether contact or tapping mode imaging is required. Tapping mode tips have resonant frequencies from 50 *kHz* to 400 *kHz*. Contact mode tips have resonant frequencies from 10 *kHz* to 75 *kHz*. The apex of standard AFM tips is around 20 *nm*, however, high resolution tips can have an apex of ~5 *nm*. Single carbon nanotube tips are also available and provide ultra-high resolution imaging.

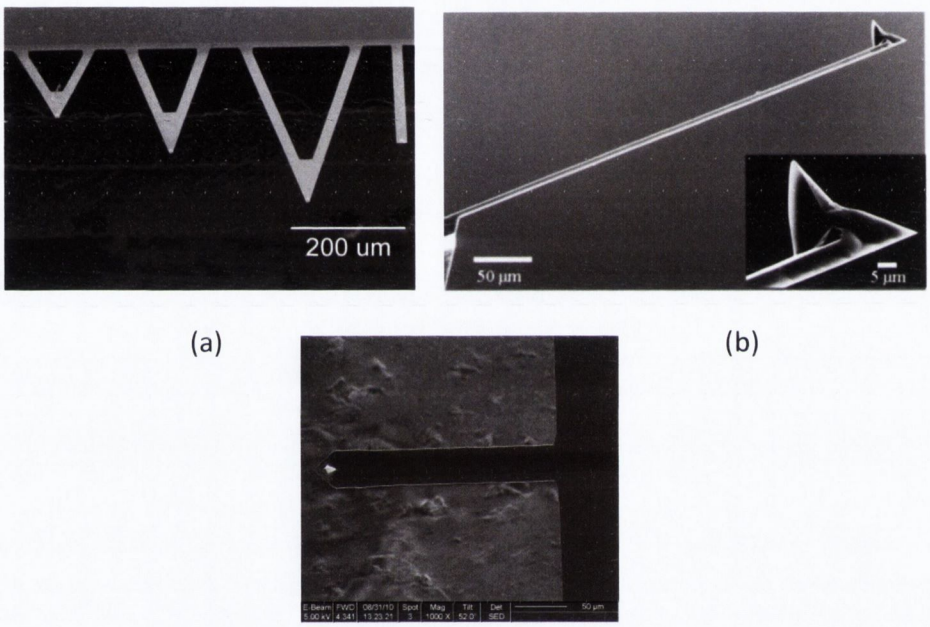

Figure 11: SEM images of AFM cantilevers, (a) triangular shaped cantilevers, (b) side on view of the cantilever, the inset shows a higher magnification image of the tip itself and (c) a top view image of the cantilever.

The lateral resolution of AFM is not nearly as accurate as the vertical resolution, which can be ±0.1 *nm*. Although AFM tips are very sharp, standard tips have a pyramidal shape, figure 10 (b), culminating in a sharp point, the tip. When the tip approaches a higher point on the surface the angular edge of the tip will image the higher point rather than the tip itself. Hence, lateral imaging is difficult and generally not reliable. This problem can be minimised by using high aspect ratio tips. The defining characteristic for both types of probes is the spring constant, *k*. For triangular cantilevers the spring constant is usually calculated using the thermal

noise method. For rectangular shaped cantilevers k is calculated using the following equation,

$$k = \frac{Et^3 w}{4L^3}$$

Where E is the Young's modulus, w is the width of the beam, t is the thickness and L is the length. There have been numerous methods reported to calculate the AFM tip spring constant[16-23]. In our experiments a different method is used to calculate k. This is important as the technique presented in this thesis results in torsional tip motion, hence, the torsional spring constant of the tip is required, not purely the normal spring constant. This is discussed in section 2.4.1.3.

The AFM is a versatile tool allowing for high resolution imaging of a wide range of surfaces in different media. Unlike STM, AFM can image conducting, semiconducting and insulating materials to the same accuracy and precision. By carefully choosing the tip and its coatings, one can probe specific physical properties. In tapping mode, the resonant frequency of the tip is modified by tip-surface interaction forces. Shifts in frequency can provide information about the sample, this is called frequency modulated AFM (FM-AFM). A similar technique, amplitude modulated AFM (AM-AFM), provides information on the phase of the cantilever oscillations which can distinguish between materials on the surface. Another main advantage of AFM is the ability to manipulate and pattern a surface. The former was used extensively in our work on the study of the electromechanical properties of nanowires (NW).

2.4. Electromechanical

Directly measuring the change in transport properties as a function of mechanical strain, known as the electromechanical effect, is extremely challenging and is highlighted by the lack of publications in the area. This is due to the lack of tools available to accurately measure both mechanical and transport properties simultaneously. The electromechanical measurement is a combination of two types of equipment and techniques. Here the AFM is utilised for mechanical measurements and a 4-point Keithley based LabView platform for electrical measurement. The AFM and lab view platform are carefully interfaced to perform

electrical and mechanical measurements in parallel. The electrical measurement components are home built and customised to be compatible with an Asylum MFP-3D AFM. The mechanical measurements will be discussed in section 2.4.1 and electrical measurements are outlined in section 2.4.2.

2.4.1. Mechanical measurement

As mentioned in Chapter 1 of this thesis, several techniques have been reported for measuring the mechanical properties of NW. Previous studies have utilised lateral AFM measurements in which the nanowire specimen is clamped at one end and loaded at various distances away from the clamped end[24]. However, the nanowire is not suspended from the substrate surface, hence, nanowire/surface friction contributes to the measured mechanical properties[24]. The method we present overcomes the main disadvantages of previous techniques by removing the wire-substrate friction, while accurately measuring the nanowire diameter and the elastic properties. In order to measure a wide range of mechanical properties such as Young's modulus, yield strength, plastic deformation and failure, a novel method using Focused Ion Beam (FIB), Scanning Electron Microscope (SEM), Electron Beam Induced Deposition (EBID) and AFM have been developed in our lab[25, 26]. Here, a slightly modified preparation technique is used. Electron Beam Lithography (EBL), Reactive Ion Etching (RIE) and UV lithography are utilised to fabricate substrates for mechanical measurements. The substrate fabrication and processing is described in the next section. The measurement technique involves laterally pushing a double clamped NW suspended above a trench with an AFM tip, while measuring the force imparted to bend, stretch or break the wire. This results in a force-displacement (f-d) curve, which can then be analysed to yield the mechanical properties of the wire.

2.4.1.1. Substrate processing for mechanical, electrical, and electromechanical measurements

Specific substrates must be fabricated to perform mechanical and electrical measurements simultaneously. 500 μm thick Silicon wafers with a thermally grown 1 μm thick SiO_2 layer on the top surface are used to fabricate the substrates. Wafers were cleaved into 1 *cm* x 1 *cm* pieces using a diamond scribe. The square pieces were sonicated in acetone for 5 *min* to remove organic material, sonicated in isopropanol

(IPA) for 2 *min* and dried using N_2 flow. UV lithography was used to define the large outer electrical contact pads, see figure 11.

In the UV lithography process the substrate was outgassed at 150 *°C* for 5 *min* in a pre-bake step. S1813 positive photoresist was applied to the centre of the substrate and spun at 5000 *rpm* for 40 *sec*, with a 500 *rpm* 5 *sec* ramp up. The photoresist was soft baked at 115 *°C* for 75 *sec* to evaporate the solvent and solidify the film. Exposure was performed using a Near Ultra Violet (NUV)-mask aligner for 5 *sec* with a wavelength, λ = 405 *nm*. This gave a dose of 23 mW/cm^2. The sample was then developed using MF-319 developer for 60 *sec*. A 5 *nm* titanium adhesion layer and 35 *nm* gold were evaporated on to the substrate and the photoresist removed over a 24 *hrs* period using acetone, in a so-called "lift-off" process. This leaves behind metal electrodes in the design specified by the lithographic mask. Figure 11 (a) shows the UV exposure steps. Figure 11 (b) is an optical image of the UV patterned electrodes after lift-off.

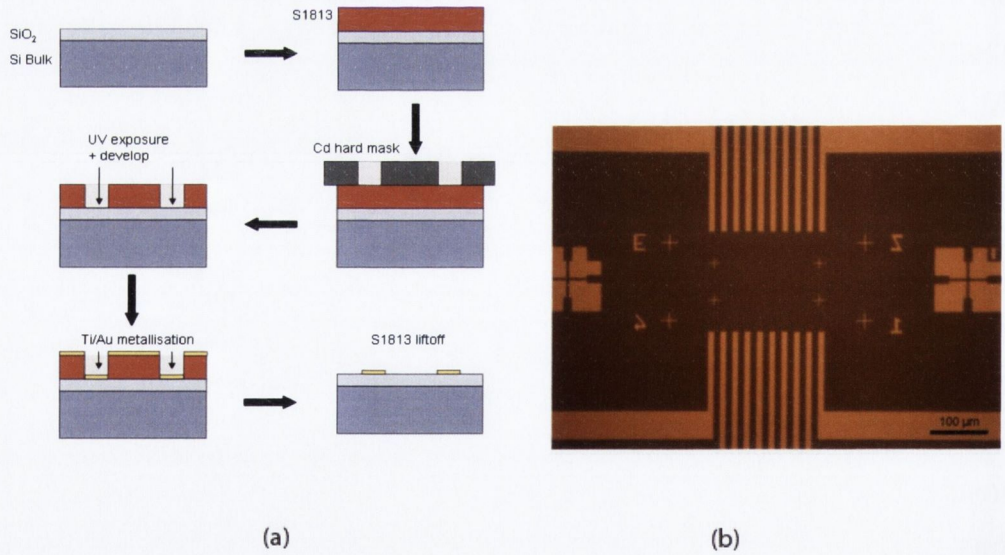

Figure 12: (a) Schematic showing the experimental steps in the UV lithography process and (b) optical image showing an electrode array fabricated using UV lithography

Electron Beam Lithography (EBL) is used to define the area where trenches will be situated. EBL is performed on substrates with UV defined electrodes. Samples were outgassed at 200 *°C* for 5 *min*. ZEP positive tone electron beam resist was applied to the centre of the substrate. The resist was spun cast on to the sample at 3000 *rpm*

for 45 *sec* with a 5 *sec* 500 *rpm* ramp up step. The resist was soft baked at 180 *°C* for 3 *mins*. Exposure was performed on a Zeiss Supra SEM system using Raith EBL software. EBL must be performed under vacuum conditions. The chamber pressure is circa 1 x 10^{-6} *mbar*. The SEM was set to an acceleration voltage of 15 *kV* and 10 μm aperture. The design mask was uploaded using the Raith software and the sample exposed at a dose of 35 $\mu C/cm^2$. The sample was then developed using BOB developer for 5 *mins*. Development exposes the under lying SiO_2 substrate while leaving the resist covering the rest of the substrate.

Reactive Ion Etching (RIE) is used to mill trenches in the oxide. RIE was performed on the EBL exposed substrates at a vacuum pressure of 6 *mT*. A 10 *sccm* CHF_3 and 40 *sccm* Ar gas mixture was used to etch the samples using an inductive coupled plasma (ICP) power of 1500 – 2500 *W* and RIE power of 70 – 250 *W*. A DC bias with an extraction voltage of -100 - -250 *V* with a 10 *T* He back pressure was used. These parameters gave an etch rate of 100 *nm/min*. The samples were etched for 2.5 *min* giving a trench depth of ~ 250 *nm*. Post RIE the ZEP resist was removed using 1165 resist remover at 80 *°C* for 24 *hrs* followed by sonication at 80 *Hz* for 60 *mins*. Substrates were then sonicated in IPA for 5 *mins* and dried using N_2 flow. The fabrication process produces 1 *cm* x 1 *cm* substrates with an array of 20 contact pads, figure 12 (a). 13 trenches 180 μm long and 2 μm wide are located in the centre of the contact pad array, figure 12. Figure 12 (b) shows an AFM image two trenches. The inset shows the depth profile.

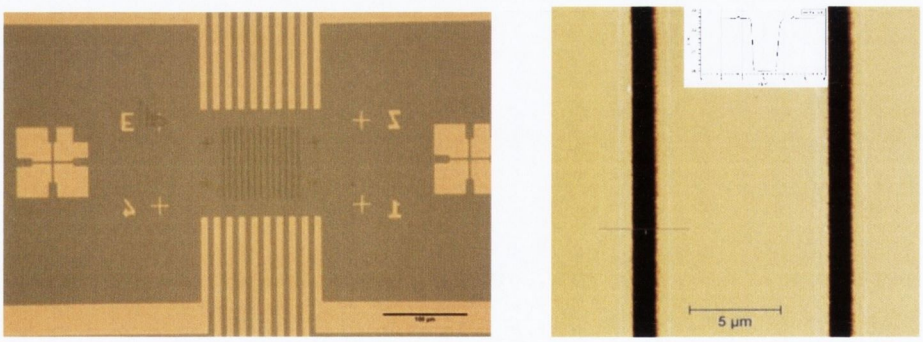

(a) (b)

Figure 13: Substrate used to perform electromechanical experiments, (a) optical image of 20 electrode array with trenches fabricated in the centre region and (b) AFM image of trench with a depth profile inset.

2.4.1.2. NW placement and contacting protocol for electrical and electromechanical measurements

Nanowires were placed on the pre-fabricated substrate by a drop-cast method. This was made possible by the NWs being dispersed in a volatile solvent after growth. In the case of germanium nanowires (GeNW), the NWs were grown using the vapour-liquid-solid (VLS) method and dispersed in IPA by our collaborators in University College Cork . Silver nanowires (Ag NW) were purchased pre-dispersed in IPA at a concentration of 20 *mg/ml*. A AgNW concentration of 0.01 *mg/ml* was prepared from the as received batch. Nickel NWs (NiNW) were purchased encapsulated in anodised aluminium oxide (AAO), as the NiNW are synthesised in an AAO template. NiNWs were removed from the AAO template by using 30 % HNO_3 to remove electrodeposited Ni from the back Au contact. The Au coating was removed by gentle exfoliation using an Au etchant. The AAO template was removed by immersion in NaOH. The Au etchant was applied to a 50 *mm* diameter swab and gently applied to the Au back-contact of the AAO/Ni NW cake, removing the Au layer. The cake was then dispersed in 3 *M* NaOH for 24 *hrs* to dissolve the AAO template. The NW's were washed in deionised water and dispersed in IPA.

NW's were dispersed on to the substrate by drop casting. Prior to drop casting the vial containing NW's was lightly agitated to give a homogenous solution. The nanowire vial was not sonicated as this sometimes breaks the NW. Between 3 μL and 5 μL of the solution was drop cast on to the substrate. A gentle N_2 flow was used to align the NW perpendicular to the trenches. This involved blowing the NW droplet in the perpendicular direction to the trench long axis resulting in most of the NW lying in the direction of the N_2 flow. The substrate was then visually inspected using an optical microscope to check for NWs spanning the trenches.

In previous studies in our group[27] NW were clamped at the trench edges by Pt-EBID in a SEM/FIB dual chamber. However, we are concerned with electrical and mechanical properties, and Pt-EBID exposes the sample and the immediate vicinity to leave a Pt halo. Instead, the NW were clamped to the trench edges by 120 *nm* EBL defined contacting electrodes, figure 13 (a).

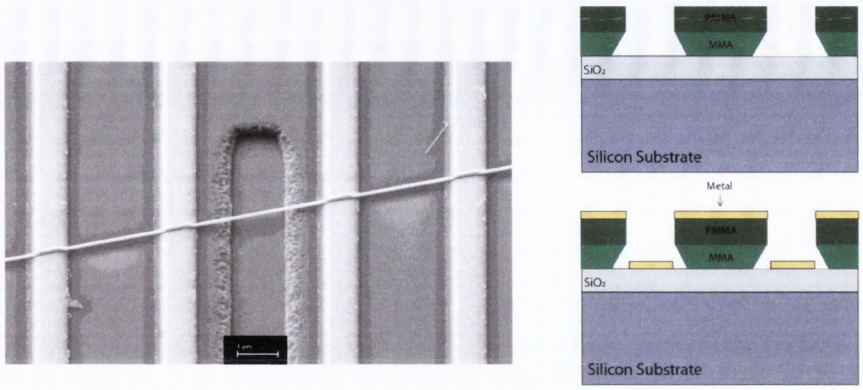

(a) (b)

Figure 14: (a) Single suspended nanowire contacted with 4 electrodes, (b) Schematic of the MMA/PMMA bilayer resist

The contacting electrodes were fabricated using EBL. A bi-layer resist was used to give an undercut in the resist cross section, clearly shown in figure 13 (b). The undercut allows the deposited metal on the exposed and non-exposed areas of the substrate to be detached from each other. Hence, no artefact metal fragments, known as 'rabbit ears', remain attached to the electrodes after lift-off. The resist stack consists of a methyl methacrylate (MMA) undercoat and polymethyl methacrylate (PMMA) top coat as shown in figure 13 (b). Substrates were degassed for 5 *mins* at 180 *°C*. MMA was spun cast at 6000 *rpm* for 45 *sec* with a 500 *rpm* 5 *sec* ramp up. The substrate was then soft baked at 165 *°C* for 2 *mins* to remove the solvent and bake the resist beyond the glass transition temperature, T_g. The substrate was allowed to cool. PMMA was spun on using the same recipe as the MMA step. PMMA was soft baked at 180 *°C* for 3 *mins*. The substrates were then loaded into the SEM chamber and allowed to pump down to circa 1×10^{-6} *mbar*. EBL was performed using a Zeiss Supra SEM and Raith EBL software, the same tool as used for trench fabrication. The design mask was uploaded using the Raith software and the sample exposed at a dose of 262 $\mu C/cm^2$. The sample was developed in 1:3 methyl isobutyl ketone : propan-2-ol (MIBK:IPA) for 45 *sec* and rinsed in IPA for 5 *sec*. The process resulted in undercut resist geometry as shown in figure 13 (b). 120 *nm* of the desired contacting metal was evaporated on to the substrate. It is important to deposit pinning electrodes whose thickness is at least 1.5 times the diameter of the nanowire to ensure stable pinning and reliable electrical contact. The bi-layer resist was then lifted off in acetone for 24 *hrs*. Figure 12 (a) shows a

single suspended Ag NW contacted and pinned by four Ag electrodes using the technique described above.

2.4.1.3. AFM calibration and operation for mechanical measurements on individual nanowires

For now, mechanical measurements will only be discussed. The combination of electrical and mechanical equipment is described in 2.4.3.

The sample is positioned on an Asylum MFP-3D AFM in such a way that the nanowire long axis lies parallel with the cantilever long axis.

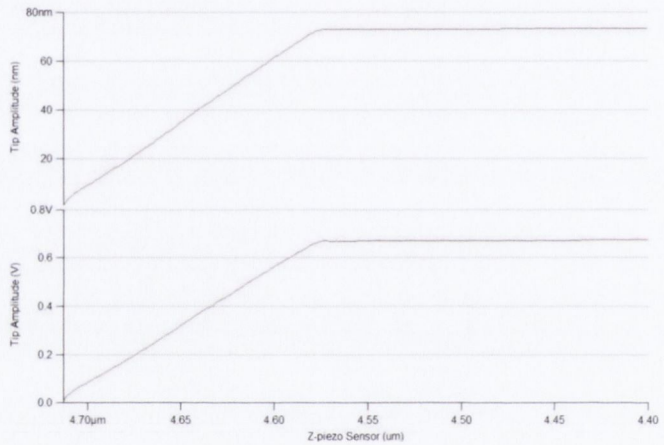

Figure 15: Tip amplitude versus z-piezo displacement. Upper panel shows amplitude in nm, the lower panel showing amplitude in photodetector voltage.

The height of the tip relative to the surface is of paramount importance. A tapping mode force plot was performed to determine the height of the tip from the surface. Figure 14 is a typical plot of tip amplitude, lower panel, and tip height, upper panel, versus z-piezo displacement for an AFM tip with a 75 *kHz* resonant frequency. The region between 4.4 μm to 4.67 μm on the x-axis shows the free amplitude of the tip where there is no tip-surface interaction. The steep slope between 0 V to 0.7 V is the AFM tip being deflected by the surface, and hence, provides the range of setpoints available for tapping mode imaging. $0V$ being the tip in contact with the surface. Figure 14, upper panel, shows the tip amplitude in *nm*. From this plot the average tip height from the surface at each setpoint could be established. For example, at a setpoint of 0.5 V the tip is on average 50 *nm* from the surface. Knowledge of tip height relative to the surface was used to draw an accurate line scan, seen later. A

tapping mode image of the nanowire was acquired. Accuracy of the manipulation was ensured by taking a high magnification image, where the nanowire takes up close to 80 % of the image. The lithography panel of the MFP-3D AFM was used to perform the manipulation. In this application the tip can be moved along a user defined closed-loop path where the velocity, direction and height of the tip from the surface are closely controlled by the user. The tip is located at the centre of the NW span length, 2 μm away from the wire in the perpendicular direction along the trench. A drive path was defined for the tip. The x-y tip velocity was set at 20 *nm/sec.*

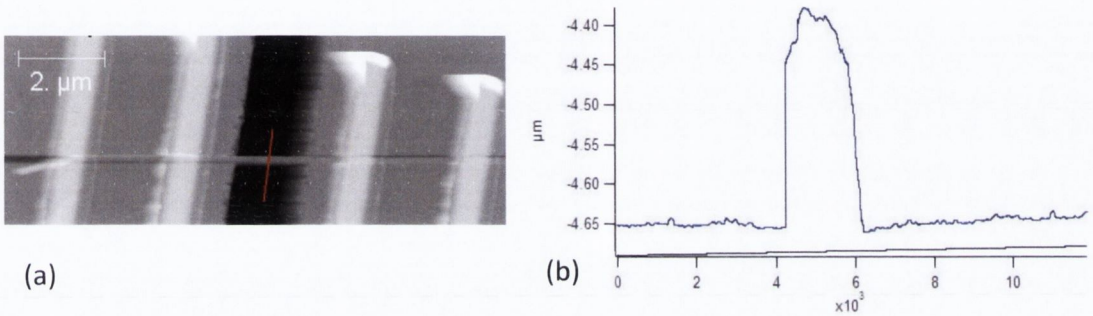

Figure 16: The location of the tip during mechanical manipulation (a) AFM image showing the drive path labelled by the red line, (b) line scan plot along the red line. This is used to specify the height of the tip for manipulation

A tapping mode line scan was taken along the defined path. The line scan accurately establishes the height of the nanowire from the bottom of the trench and allows the user to choose the height of the tip. A line scan plot along the red line in figure 15 (a) is shown in figure 15 (b). The height of the tip was manually chosen from the line scan click and drag option. The optimal height of the tip depends on the amplitude vs. tip-surface height plot shown in figure 14.

Prior to the manipulation contact mode was selected. This locks the z-piezo to the tip height selected by the line scan, and turns the feedback off so the z-piezo doesn't lift the tip as it contacts the nanowire. The path was chosen to either perform a sequence of loading and unloading cycles on the wire or pass through the wire in a single shot experiment leading to wire failure. Figure 16 shows a typical deflection voltage vs. displacement plot for an Ag NW loaded to fracture.

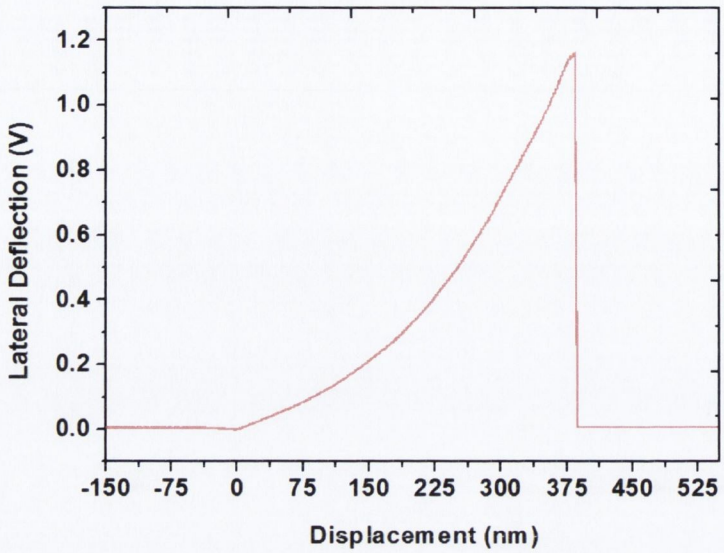

Figure 17: Typical lateral displacement curve for a nanowire displaying brittle behaviour. The lateral deflection has units of Volts, from the photodetector.

The red line represents the lateral signal from the torsional motion of the tip moving the laser beam laterally on the photodetector. The initial region of the plot from -150 *nm* to 0 *nm* represents the baseline by which the tip is approaching the nanowire. The lack of deflection in this region shows the tip is not touching the bottom of the trench. At 0 *nm* the tip begins to laterally load the nanowire. The sharp drop in lateral deflection at 370 *nm* is the point at which the nanowire breaks. This releases the torsional force on the tip and allows it to revert to its pre-manipulation lateral deflection. Once the manipulation is over a tapping mode image of the fractured wire was captured. Figure 17 (b) shows the complete fracture of the nanowire after the manipulation. Once the nanowire was loaded the tip was immediately calibrated to determine the lateral and vertical sensitivity.

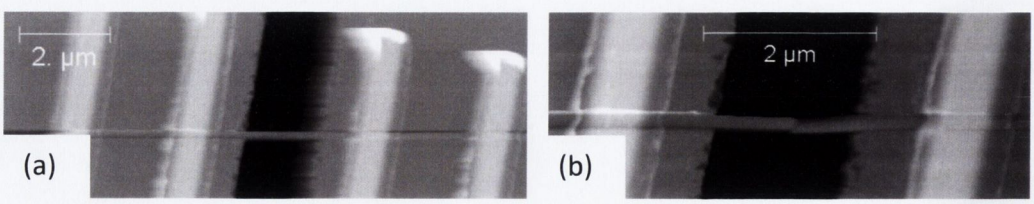

Figure 18: AFM images of a nanowire before, (a,) and after, (b), fracture

Calibration was performed following the procedure and calculations set out by Schwarz *et al*[28]. The tip is laterally calibrated by loading and unloading the tip against a non-compliant calibration grid at least 3 times as in figure 18. The calibration grid is constructed using Silicon Nitride and acts as a rigid body to push against.

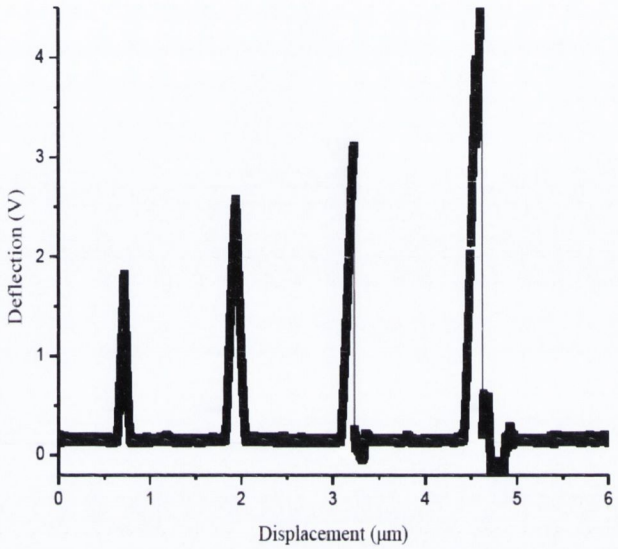

Figure 19: Lateral loading curves used to calibrate the torsional spring constant of the tip.

The calibration was carried out at the same tip height as the manipulation. This is very important as the relative stiffness of the cantilever depends on the loading point along the height of the tip. The resulting slope gives the lateral sensitivity, known as S_{lat}, of the cantilever in V/m. The vertical sensitivity of the cantilever, known as S_{ver}, is calibrated by performing a vertical force plot. The AFM is set to contact mode. A suitable position to perform the force plot was selected and a trigger setpoint of 0.2 V was chosen. The tip is brought in contact with the surface by performing an initial rough force plot. This plot allows the tip to find the surface from the withdrawn state. A second force plot was then performed. Figure 19 shows a typical plot of vertical deflection against the z-piezo displacement. The z-piezo data is the absolute value of the piezo position. Hence, an increase means the piezo is being extended. In this case an extension in the z-piezo will push the tip closer to the surface. The flat region between 6 μm and 6.225 μm represents the free deflection of the tip at which the tip is not in contact with the surface. At approximately 6.225 μm the tip is attracted to the surface through long range attraction causing initial negative

deflection. The tip was driven further into the surface between 6.225 μm to 6.3 μm and was positively deflected to the 0.2 V setpoint.

The tip is only pushed into the surface to a deflection setpoint of 0.2 V to protect the tip from damage. The inverse slope of this graph, expressed in m/V, gives a value for the vertical sensitivity, S_{ver}. The tip was then immediately removed from the AFM and brought to the SEM to measure the physical dimensions of the cantilever. Width (w), Length (L), Thickness (t) and tip length (l_{tip}) were measured using SEM. Typical values for w, L, t, l_{tip}, S_{ver} and S_{lat} for 300 kHz and 75 kHz are shown in table 2. Figure 20 shows the SEM images used to measure the dimensions of the AFM tip. The tip is rotated and tilted in the SEM chamber to achieve the optimum measuring angle.

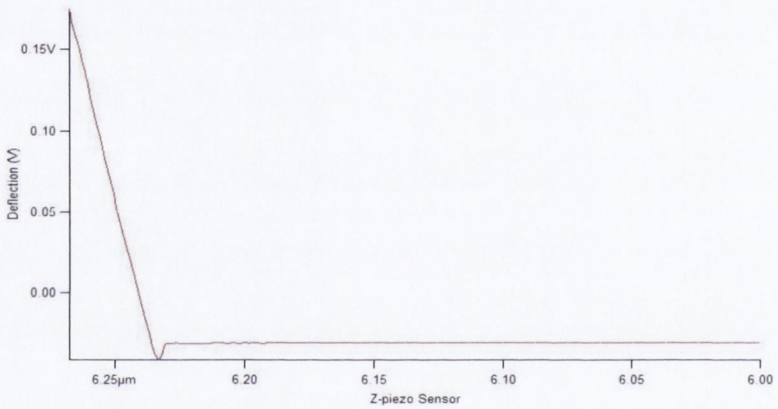

Figure 20: Vertical deflection - z-sensor plot used to calculate the vertical sensitivity of the AFM tip

The following well known equation relates the force, F, exerted by the tip and the relative change in signal on the photodetector, ΔU_{lat}, in volts;

$$F = \frac{Gwt^3}{4L^2 l_{tip}} S_{ver} \Delta U_{lat}$$

where G is the shear modulus. The cantilever spring constant, k_c, is calculated using the calibration parameters. The cantilever spring constant is calculated using the following the equation;

$$k_c = S_{lat} \frac{F}{\Delta U_{lat}}$$

This technique has been employed in all AFM based mechanical measurements presented in this thesis.

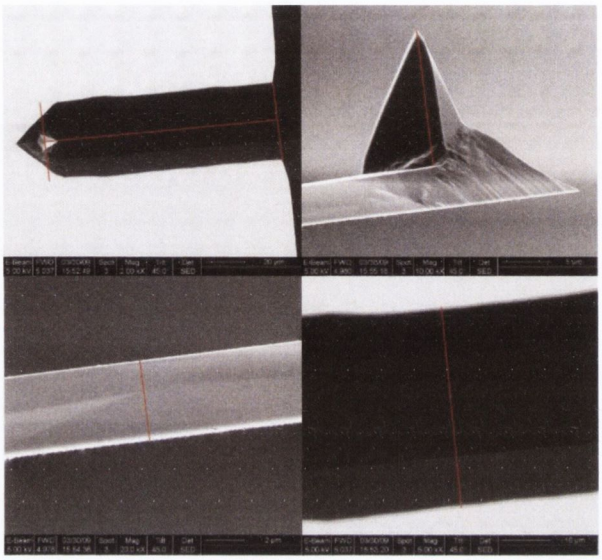

Figure 21: SEM images of an AFM tip. These images are used to measure the dimensions of the cantilever and tip, essential for the calibration procedure. The length was measured from the end of the cantilever to the apex of the tip. The width was measured at various locations along the length of the cantilever and an average value calculated. The thickness was measured in a similar fashion. The tip length was measured from the base of the tip to the apex. Accurate dimensions were achieved by tilting the tip within the SEM chamber in order to align the electron beam with the desired surface.

Table 3: Geometry and sensitivity comparison between 300 kHz and 75 kHz AFM tips

	W (μm)	***t (μm)***	***L (μm)***	L_{tip} ***(μm)***	S_{lat} ***(V/m)***	S_{ver} ***(m/V)***
300 *kHz*	41	4. 2	120	13. 5	20	5×10^{-8}
75 *kHz*	32	3. 5	240	13	45	2×10^{-7}

2.4.2. *Electrical measurement*

Measuring the transport properties of single nano-entities is non-trivial and requires the use of sensitive source-drain meters and multi-meters. In this thesis, single nanowire electrical properties are measured in a 4-point regime. 4-point electrical measurement eliminates metal/nanowire interface contact resistance and probe lead resistances. Single NWs are contacted with four isolated electrodes via a series of lithography, etching and metallisation steps, the procedures are described extensively earlier. Figure 21 shows a single Ag NW contacted with four Ag electrodes and the resulting 2-point and 4-point current-voltage (I/V) curve.

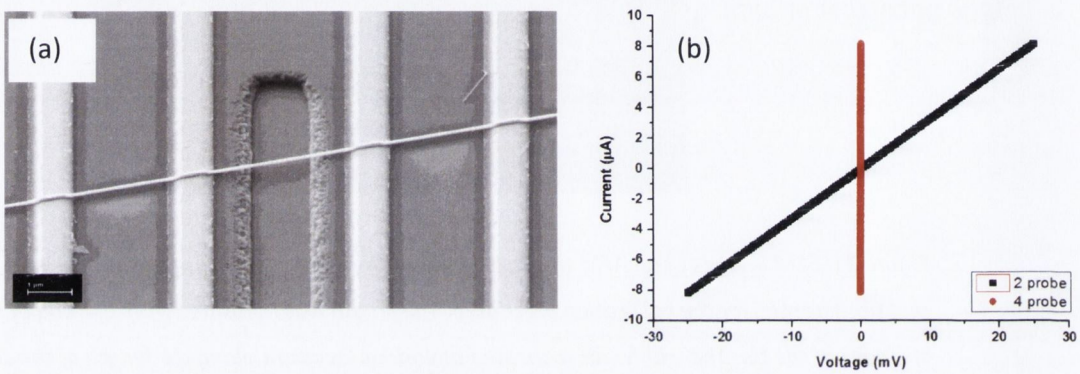

Figure 22: (a) SEM image of a single Ag NW, spanning a trench, contacted with 4 electrodes, (b) 2 and 4-point IV characteristics of the device shown in (a).

Electrical characterisation is performed using two sets of equipment. Samples are characterised using an isolated Karl Suss probe station to ensure all four contact leads are connected to the nanowire. The probe station is controlled using multiple LabView VI's that allow either the voltage (V) or current (I) to be swept through negative and positive biases. The system also allows constant voltage or current to be sourced. Samples were probed by commercially available tungsten micromanipulator needles with a tip diameter of 20 μm that were placed on the contact pads using a *x 10* and *x 50* magnification optical microscope. DC voltage was sourced using a Keithley 2400 source meter. Current and measured voltages were read by two Keithley 2000 multimeters. A current pre-amplifier was used to give accurate measurement at low currents ($>\mu A$). All Keithley instruments were controlled through LabView. A typical IV using the probe station for a single Ag NW is shown in figure 21 (b). This system was used to ensure the fabrication process

produced functioning samples. NiNWs were electrically characterised using a Keithley 4200 SCS parameter analyser. The resistivity values recorded on both our home built electromechanical apparatus and electrical probe station are in agreement with other known electrical measurements on similar nanowires, as shown in chapters 3, 4 and 5. To perform electromechanical measurements a home built electrical measurement system was built to couple with an Asylum MFP-3D AFM.

2.4.3. Electromechanical measurement

Here we describe the approach to performing electromechanical measurements, providing a direct measure of the influence of strain on the NW electrical resistance. The experimental set-up is shown in figure 22 and consists of an Asylum MFP-3D atomic force microscope combined with a home built probe station capable of making accurate 4-point resistance measurements. NW mechanical properties were measured using an AFM lateral manipulation technique developed previously[25, 26, 29], which allows the full spectrum of mechanical properties to be measured, ranging from elasticity to plasticity and failure, and during which a simultaneous measurement of the resistance change of the NW was recorded. To perform synchronised 4-point resistance and three-point mechanical measurements the substrate was attached to a chip carrier and electrically connected to the chip carrier by wire-bonding. It was essential to ensure that the wire-bonding sites were located at least 5 *mm* from the nanowire area to ensure the AFM tip access to the nanowire site. The chip carrier was securely connected into a chip holder resulting in ohmic contact between the substrate and the electrical measurement system, and a stable platform for mechanical measurements.

For electromechanical measurements the voltage sourced (V_S) was constant. Hence, the current and the measured voltage across the circuit were also constant. When the nanowire was loaded by the AFM tip a change in resistance can only be attributed to the nanowire and not to changes in V_S. The electrical contacts were placed >500 *nm* away from the NW clamps (the clamp being the edge of the trench) to ensure that a change in resistance was not due to mechanical alteration at the contact/NW interface.

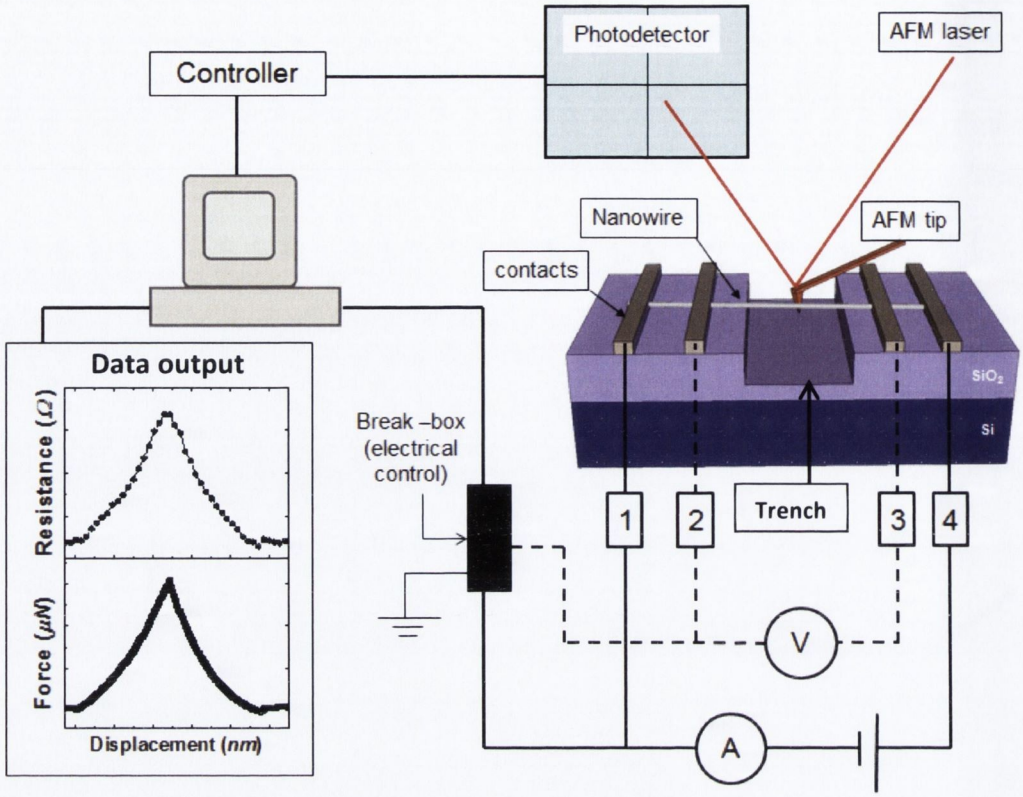

Figure 23: Schematic of the electromechanical experiment. The AFM allows for accurate mechanical characterisation by lowering the AFM tip below the axis of the nanowire, into a predefined trench, and laterally driving the tip in the x-y plane perpendicular to the nanowire long axis until the AFM tip loads the nanowire. During loading the torsional motion of the AFM is recorded by the AFM laser-photodetector signal. The contacts, labelled 1-4, allow for 4-point resistance measurement; voltage is sourced and the current is measured across the outermost contacts 1 and 4. The voltage drop across the nanowire is measured across the inner two contacts 2 and 3. The lateral signal from the AFM tip torsional motion during nanowire loading is measured in unison with the 4-point resistance giving resistance- and force-displacement curves. The break box allows the user to control each electrical contact individually, essential during experiment assembly.

In order to perform electrical measurements whilst performing AFM requires the contacting leads and cables to be accessed from underneath the sample. The reason being the sample surface must be flat to allow the AFM tip to be positioned accurately and provide un-obstructed access to the manipulation site. The chip holder clipped into a chip carrier that was mounted on a home built support frame that attached to the AFM scanner. The chip carrier contact pins were soldered to electrical wire that entered into a break box. The break box allows the user to control each contact individually. This is especially important for NiNW electrical measurements, as we

will see later. The break box was connected to a Keithley 6430 source meter and Keithley 2000 multimeter via coaxial cables. Here, the Keithley 6430 acts as both V_s and current measure, I_m, whilst the Keithley 2000 multimeter measured voltage, V_m. All of the Keithley's were controlled through LabView. Using this protocol electrical measurement and mechanical measurement can be performed simultaneously using lateral-AFM and our home built electrical system. This method was used extensively throughout this thesis, and provided the critical results presented in chapter 3, 4 and 5.

2.5. Conclusion

Scanning probe microscopy and Electron microscopy are cornerstones to nanotechnology, spanning a wide range of materials in varied fields such as engineering, biology, chemistry and physics. They allow us to view, manipulate, control and characterise matter on a minute scale. We have demonstrated how SPM allows us to study the mechanical and electromechanical properties of low dimensional materials, while EM allows us to characterise and control materials through processes such as EBL. AFM, SEM, TEM and EBL were described in detail and were used extensively throughout this thesis.

In the next chapter we will describe the mechanical and electromechanical properties of germanium nanowires, discussing the limitations and reasons for working with metallic nanowire systems.

2.6. References

1. Drummond, S.P., Allen, T. D., , *Introduction to Electron Microscopy for Biologists, Vol. 88 of Methods in Cell Biology, T. D.Allen.* Academic Press, 2008(20): p. 97-108.
2. Takahashi, H., K. Ohata, and T. Morishita, *TEM studies on the crystal structure of YBa2Cu3O7–x thin films prepared by pulsed laser deposition.* Journal of Materials Research, 1992. **7**(09): p. 2333-2336.
3. de Broglie, L., Annales de Physiques, 1925. **3**.
4. Davisson, C. and L.H. Germer, *Diffraction of Electrons by a Crystal of Nickel.* Physical Review, 1927. **30**(6): p. 705-740.
5. Ruska, E., Knoll, M., Z. techn. Physik, 1931. **20**(21): p. 389-400.
6. Hirsch, P.H., A.; Nicholson, R.; DW, P.; Whelan, M. , *Electron microscopy of thin film crystals.* New York, 1977.

7. Varela, M., et al., *MATERIALS CHARACTERIZATION IN THE ABERRATION-CORRECTED SCANNING TRANSMISSION ELECTRON MICROSCOPE.* Annual Review of Materials Research, 2005. **35**(1): p. 539-569.
8. Hatzakis, M., *Electron Resists for Microcircuit and Mask Production.* Journal of The Electrochemical Society, 1969. **116**(7): p. 1033-1037.
9. Broers, A.N., et al., *Electron-beam fabrication of 80-[A-ring] metal structures.* Applied Physics Letters, 1976. **29**(9): p. 596-598.
10. Chang, T.H.P., *Proximity effect in electron-beam lithography.* Journal of Vacuum Science and Technology, 1975. **12**(6): p. 1271-1275.
11. Drouin, D., P. Hovington, and R. Gauvin, *CASINO: A new monte carlo code in C language for electron beam interactions—part II: Tabulated values of the mott cross section.* Scanning, 1997. **19**(1): p. 20-28.
12. Hovington, P., D. Drouin, and R. Gauvin, *CASINO: A new monte carlo code in C language for electron beam interaction —part I: Description of the program.* Scanning, 1997. **19**(1): p. 1-14.
13. Binnig, G.R., H., *Scanning Tunneling Microscopy.* IBM Journal of Research and Development 1986. **30**(355).
14. Binnig, G., C.F. Quate, and C. Gerber, *Atomic Force Microscope.* Physical Review Letters, 1986. **56**(9): p. 930-933.
15. Zhang, Y., et al., *Image-based hysteresis modeling and compensation for an AFM piezo-scanner.* Asian Journal of Control, 2009. **11**(2): p. 166-174.
16. Gibson, C.T., et al., *Method to determine the spring constant of atomic force microscope cantilevers.* Review of Scientific Instruments, 2004. **75**(2): p. 565-567.
17. Gibson, C.T., et al., *A nondestructive technique for determining the spring constant of atomic force microscope cantilevers.* Review of Scientific Instruments, 2001. **72**(5): p. 2340-2343.
18. Sader, J.E., J.W.M. Chon, and P. Mulvaney, *Calibration of rectangular atomic force microscope cantilevers.* Review of Scientific Instruments, 1999. **70**(10): p. 3967-3969.
19. Akihiro, T., et al., *A method for determining the spring constant of cantilevers for atomic force microscopy.* Measurement Science and Technology, 1996. **7**(2): p. 179.
20. Gates, R.S. and M.G. Reitsma, *Precise atomic force microscope cantilever spring constant calibration using a reference cantilever array.* Review of Scientific Instruments, 2007. **78**(8): p. 086101-3.
21. Golovko, D.S., et al., *Nondestructive and noncontact method for determining the spring constant of rectangular cantilevers.* Review of Scientific Instruments, 2007. **78**(4): p. 043705-6.
22. Langlois, E.D., et al., *Spring constant calibration of atomic force microscopy cantilevers with a piezosensor transfer standard.* Review of Scientific Instruments, 2007. **78**(9): p. 093705-10.
23. Pettersson, T., et al., *Comparison of different methods to calibrate torsional spring constant and photodetector for atomic force microscopy friction measurements in air and liquid.* Review of Scientific Instruments, 2007. **78**(9): p. 093702-8.

24. Wong, E.W., P.E. Sheehan, and C.M. Lieber, *Nanobeam Mechanics: Elasticity, Strength, and Toughness of Nanorods and Nanotubes.* Science, 1997. **277**(5334): p. 1971-1975.
25. Bin Wu, A.H., John J. Boland, *Mechanical properties of ultrahigh strength gold nanowires.* Nature Materials, 2005. **4**(525-529).
26. Bin Wu, A.H., John J. Boland, John E. Sader, XiaoMing Sun, YaDong Li, *Microstructure-Hardened Silver nanowires.* Nanoletters, 2006. **6**(3): p. 468-472.
27. Wu, B., et al., *Microstructure-Hardened Silver Nanowires.* Nano Letters, 2006. **6**(3): p. 468-472.
28. Schwarz, U.D., P. Koster, and R. Wiesendanger, *Quantitative analysis of lateral force microscopy experiments.* Review of Scientific Instruments, 1996. **67**(7): p. 2560-2567.
29. Ngo, L.T., et al., *Ultimate-Strength Germanium Nanowires.* Nano Letters, 2006. **6**(12): p. 2964-2968.

Chapter 3: Mechanical and electromechanical properties of Germanium nanowires

3.1 Motivation

Nanowires are expected to have great potential for applications in sensors, actuators and nanoelectromechanical systems (NEMS)[1-3]. In the drive to implement them into functional devices their mechanical and electrical properties have been extensively studied. However, their electromechanical properties have not been widely studied mainly due the difficulty in performing these combined measurements. In this chapter our main interest lies in mechanical and electromechanical properties of germanium nanowires, however we will discuss silicon as well. Silicon and germanium are quite similar; both are metalloids belonging to group 14 with germanium just below silicon in the periodic table. Both crystals are face-centred cubic (FCC) with the silicon lattice parameter being 5. 43 Å and germanium's 5.64 Å. Silicon nanowires have been studied to a much larger extent than germanium nanowires, due to the importance of bulk silicon in the micro-electronics industry. Germanium was used to build the first transistor in 1947 as it has higher electron mobility than silicon. However the main advantage of silicon over germanium is its superior oxide. SiO_2 has been extensively studied and characterised over the years which makes it easy to incorporate silicon into devices. Germanium oxide is of poor quality (mixture of GeO_x) with GeO_2 soluble in water. Nevertheless, recent advances in nanotechnology and end-of-the roadmap issues with silicon have resulted in renewed interest in germanium.

In terms of mechanical properties, both silicon and germanium are elastic materials exhibiting brittle failure in their bulk form. The stiffness and strength of silicon and germanium are 135 – 190 *GPa* and 22 *GPa*, and 103 – 150 *GPa* and 14 *GPa* respectively[4, 5]. The range of Young's moduli data is due to stiffness differences along different crystallographic orientations. Silicon exhibits a slightly larger

Young's modulus (around 25%) and strength (around 35%) compared with germanium. Importantly, these values were calculated for defect-free materials and therefore represent an upper bound for these parameters.

There have been several reports on the mechanical properties of both silicon[6-9] and germanium nanowires[9-11]. In 2011 Kim *et al* [8] studied the mechanical properties of silicon nanowires (15-70 *nm* diameter) using nanoindentation and AFM three-point bending techniques, comparing their results with others in the literature as well as under different mechanical models. The double-clamped suspended silicon nanowires were prepared by aligning the nanowire specimen on a flat substrate and using conventional lithography and plasma etching to fabricate the clamp points and suspension, the results are summarised in figure 1. The Young's modulus for bulk silicon is represented by the hashed bar in the upper panel[12]. All results, bar one data set, display moduli greater and less than bulk values (103 – 275 *GPa*), with the lack of any trend tending towards increased mechanical stiffness at smaller dimensions. Although very scattered, there was an increase in the ultimate strength as would be expected at smaller dimensions[13]. The authors found the line tension model best described the mechanical properties of silicon nanowires in a 3-point bending experiment. Similar characteristics have been observed in zinc oxide nanowires[14].

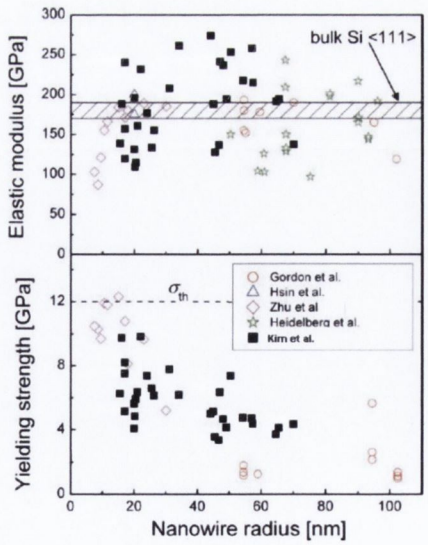

Figure 1: Elastic modulus and yield strength of silicon nanowires as function of lateral nanowire dimensions[8]. The hashed region in the upper panel represents the bulk modulus for silicon, with the dashed line in the lower panel representing the theoretical strength for silicon.

In 2008 Smith *et al*[11] reported on germanium nanoelectromechanical resonators of diameters from 50 – 140 *nm*. The nanowires were pinned at the edge of a copper TEM grid using EBID. By applying an AC voltage between an STM tip placed at the clamped end of the nanowire and a tungsten probe near its free end the nanowire oscillated at its electromechanical resonance shown in figure 2. The frequency response and the vibrational amplitude was measured and the Young's modulus was determined. The authors found no diameter dependence for the range studied. In this clamp free beam configuration the calculation of the Young's modulus was carried out using the following equation derived from the Euler-Bernoulli model;

$$f_1 = \frac{1.875^2}{8\pi}\sqrt{\frac{E}{\rho}}\frac{d}{L^2}$$

where f_1 is the natural resonance frequency, E the Young's modulus, ρ the density of Ge, d the diameter of the wire and L its length. The average Young's modulus was found to be 106 *GPa*, which is within the range of moduli for Ge. In addition, the authors measured the mechanical quality factor of the nanowires and found it decreased with decreasing diameters, attributing this phenomenon to surface losses which increased with the increasing surface-to-volume ratio of the nanowires. This result indicates that surface losses may be a limiting factor for nanoscale resonators and electromechanical devices. Surface chemistry and surface structure are essential to the understanding of energy dissipation phenomena at the nanoscale.

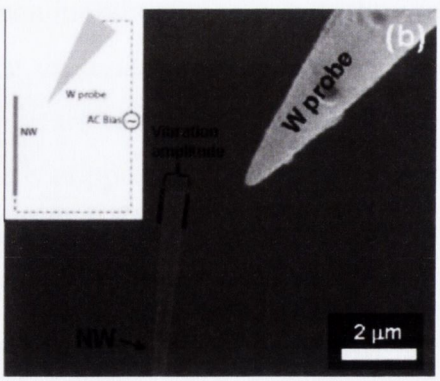

Figure 2: SEM image of a germanium nanowire vibrating due to the AC voltage applied to the tungsten tip located near the free end of the nanowire. The vibrational amplitude was measured using SEM[11]*. Inset is a schematic of the experimental set-up.*

The vibrational and actuatable nature of free standing, or bridged like semiconducting nanowires, has been utilised to make the nano-analogue of microelectromechanical systems (MEMS), namely NEMS. In fact, this is a very important area of emerging research as alternative device structures are envisaged to solve the scaling issues with planar silicon technology, with nanowires being the subject of various studies including switches[15, 16] and high frequency resonators[17-19]. There has been a significant number of reports on carbon nanotube and silicon nanowire based NEMS, but very few concerning germanium nanowires, except for that of Smith *et al*[11], Andzane *et al*[20], and Ziegler *et al*[21].

In 2009 Andzane *et al*[20] studied germanium nanowires in a two-terminal NEMS geometry with ON/OFF regimes carefully controlled by balancing adhesion, electrostatic and elastic forces. The authors used a TEM-SPM technique previously developed[21]. A schematic of the experimental approach is shown in figure 3. A GeNW was pinned at the end of a gold tip and in close proximity to an opposing electrode, as displayed in figure 3. The distance between the two electrodes was carefully controlled to overcome electrostatic forces (Van der Waals forces) that would cause the nanowire to snap onto the opposite electrode, turning the device ON. Upon the application of a voltage between the two electrodes, the NW was forced to deform and move towards the opposite electrode. When a sufficient voltage was applied, the attractive force between the tip and the nanowire specimen exceeds the spring constant of the NW and contact occurs between the tip and the NW. When the voltage was reduced, the NW remained in contact with the electrode at a lower voltage than the initial contact voltage, due to adhesion forces.

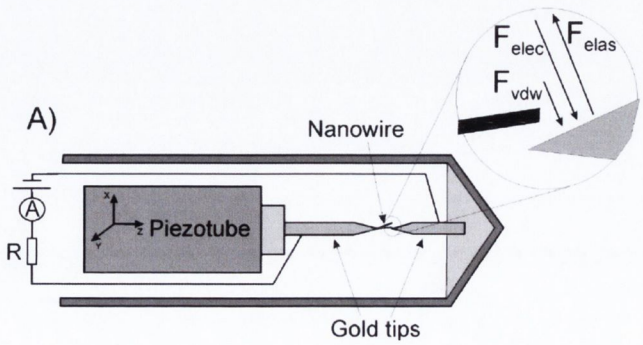

Figure 3: Schematic of the experimental set-up for TEM-SPM study of Ge NEMS[20]

The authors also found that adhesion forces and elastic forces were similar for large NWs (diameter larger than 50 nm). However for smaller diameter NWs, the adhesion force was estimated to be an order of magnitude smaller than the elastic force. This was attributed to the different thickness of oxide on facets of the NWs, hence decreasing the contact area with the electrode. Current densities in the range of $\mu A\ m^{-2}$ were measured across individual nanowires, and due to the high resistivity of Ge NWs, they could be used for high voltages devices.

Ge NWs have been proven as useful resonators and can be integrated into functional devices. Another interesting and useful area of interest for both germanium and silicon nanowires is that of band gap engineering. Ever since the 1950s researchers have studied the effect of strain on band structure for silicon and germanium[22, 23], and today strained silicon components are actively incorporated into functional devices to improve the device performance by increasing carrier mobility within the channel[24]. Hong *et al*[25] reported on strain driven band gap modulation in silicon nanowires. The objective of the study was to understand a mechanism to obtain a direct band gap in Si NWs. Using DFT the authors studied the effect of uniaxial strain on Si NWs depending on their crystal orientation and diameters. Figure 4 shows the variation of band gap for different crystal orientations and diameters. This study is in good agreement with expectation that smaller diameter wires have larger band gap due to quantum confinement effects[26].

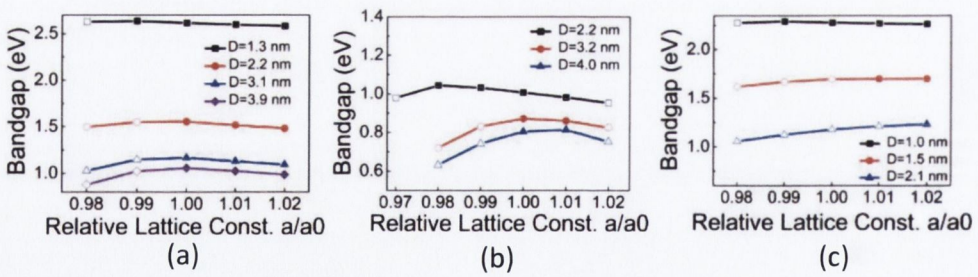

Figure 4: Band gap variation as function of strain for (a) [100] (b) [110] and (c) [111] orientations. The filled and unfilled symbols represent direct and indirect band gap respectively[25].

It was found that tensile strain enhances direct band gap characteristic for the directions [100] and [111]. For the direction [110] both tensile and compressive stresses result in an indirect band gap. The strain dependence on crystal orientation was attributed to the different shapes of wave functions of the valence band for the different crystal orientations. In addition the authors observed that

smaller nanowires with larger quantum confinement had a tendency to exhibit a direct band gap.

In 2012 Greil *et al*[27] studied the effect of tuning the electro-optical properties of germanium nanowires by tensile strain. The authors describe the electrical and electro-optical characterisation of single crystalline germanium nanowires under tensile strain conditions. The measurements were performed on vapour-liquid-solid (VLS) grown germanium nanowires integrated into a micromechanical 3-point strain module. Uniaxial stress was applied along the <111> growth direction of individual 100 *nm* thick wires while performing electrical and optical characterisation at room temperature. Figure 5 (a) shows an SEM image of the germanium nanowire clamped in the strain module. Figure 5 (b) highlights the results.

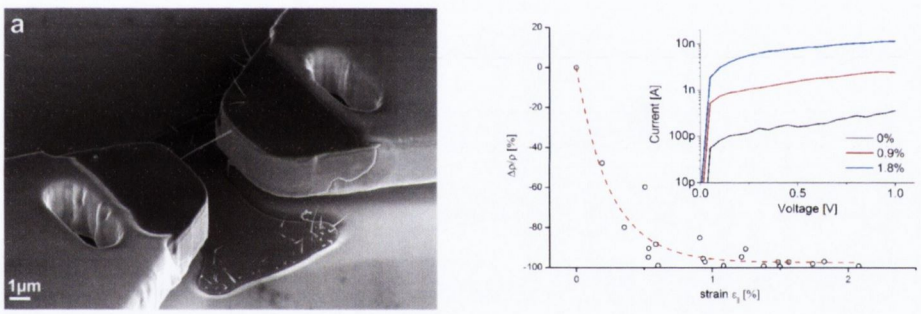

(a) (b)

Figure 5: (a) SEM image of the three point strain module featuring a single GeNW connected the shuttle to the right with the one on the left. (b) Change in resistivity with increasing strain for an individual GeNW. Inset shows the IV curves at each strain[27].

The authors found an exponential decrease in the relative change in resistivity with increasing strain showing an anomalously high and negatively signed piezoresistive coefficient.

In this chapter we investigate the mechanical and electromechanical properties of germanium nanowires, describing an improved TEM/AFM based mechanical characterisation method. We also introduce an AFM based mechanical loading system, referred to as the nanowire "pulley system", that imparts uniaxial tensile deformation on the nanowire, describing its success and, more importantly, its limitations in terms of electromechanical measurements. We also introduce initial

results and attempts to perform electromechanical experiments on germanium nanowires, describing the roadblocks encountered and reasons for moving to metallic silver and nickel nanowire systems.

3.2 Germanium nanowire synthesis and structure

Nanowires were synthesised by our collaborators in *Dr. Justin Holmes'* group in University College Cork using the super critical fluid method[28]. To achieve small diameters the synthesis was performed from gold nanoparticles (Au NPs) capped with perfluorodecanethiol which prevents the Au NPs from agglomeration during the synthesis process. Diphenylgermane precursor was pressurised to 27 MPa and injected with the Au NPs into the reaction cell at 380 °C with super critical CO_2.

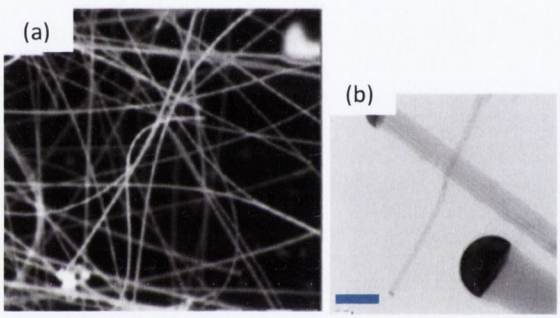

Figure 6: (a) SEM image of germanium nanowires after synthesis (b) TEM image of three germanium nanowires capped with Au NPs (40 nm scale bar).

Figure 6 shows SEM and TEM images of the germanium nanowires after synthesis. Figure 6 (a) outlines the different diameters found in a single dispersion and 6 (b) shows TEM image of the germanium nanowires capped with Au NP. To create small nanowires the temperature must be between 350 - 400 °C[28]. However, at these low temperatures the reaction is kinetically driven and not thermodynamically driven which results in a higher number of kinetic structures and defects[29]. The NWs were dispersed in isopropanol and gently sonicated for 30 *sec* to form a homogenous dispersion before use.

3.3 Mechanical Properties of Germanium Nanowires (GeNW)

3.3.1 Experimental approach

Mechanical measurements on GeNWs were performed using the lateral-AFM 3-point bending technique outlined in chapter 2. Here, we will give a brief synopsis of the technique. A SiO_2 substrate with RIE etch-defined trenches was prepared by EBL exposing 200 *nm* wide *x* 100 μm long lines using ZEP 520A resist. The ZEP 520A was exposed at an area dose of 30 $\mu C/cm^2$ and developed using the standard developer. RIE was used to selectively etch 250 *nm* deep trenches into the SiO_2, the ZEP acting as a mask. ZEP 520A was then removed using 1165 resist remover. A pre-dispersed solution of GeNWs was drop cast on to the fabricated trenched SiO_2 substrate. The NWs were aligned perpendicular to the trench edge by nitrogen flow and imaged using SEM to locate suitable wires. The NWs were mechanically clamped to the trench edge using Pt-EBID, resulting in suspended GeNWs ready for mechanical interrogation using AFM, figure 7 (b) shows an AFM image of an individual suspended GeNW clamped using Pt-EBID.

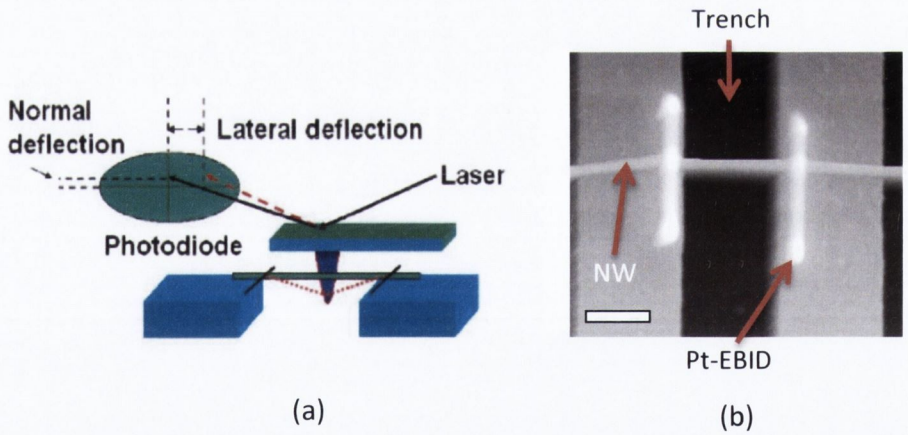

Figure 7: (a) Schematic diagram of the lateral-AFM 3-point bending technique, (b) AFM image of an individual suspended NW clamped at the trench edges using Pt-EBID.

Firstly, using an Asylum MFP-3D AFM, the area was imaged in tapping mode and the NW located. The AFM tip was then brought below the plane of the NW and driven perpendicular to the NW long axis. The AFM tip contacted and loaded the NW, recording the tip deflection on the photodetector. After careful tip calibration, outlined extensively in chapter 2, the NW mechanical properties were extrapolated. Figure 7 (a) shows a schematic of the AFM lateral loading technique. In the next section we present the results for the mechanical properties of GeNWs between 10-80 *nm* in diameter.

3.3.2 Mechanical properties of GeNWs between 10-80 nm diameter using the lateral AFM 3-point bending technique

Germanium nanowires of diameters between 10 – 80 *nm* were mechanically tested using the technique outlined above, and analysed using the generalised mechanical model developed in our group[30];

$$F_{center} = \frac{192EI}{L^3} f(\alpha)\Delta z_{center} \qquad (1)$$

where F is the applied force, E is Young's modulus, I is the areal moment of inertia, Δz_{center} is the lateral displacement and the $f(\alpha)$ term accounts for tensile deformation along the nanowire. A full description of the mechanical model is described in the appendix. A wide range of diameters were measured for two reasons; a wide spectrum of dimension allows us to elucidate scaling trends, and, the synthesised solution has a large NW size distribution. Figure 8 displays the Young's modulus, E (upper panel) and the strength, σ (lower panel) determined for each nanowire. The hashed box in the upper panel represents the calculated value of E for germanium, the range between 100-150 GPa accounts for the different values of E depending on the crystal direction. The dashed line in the lower panel represents the average calculated strength for germanium, 13.1 ± 4.2 *GPa*.

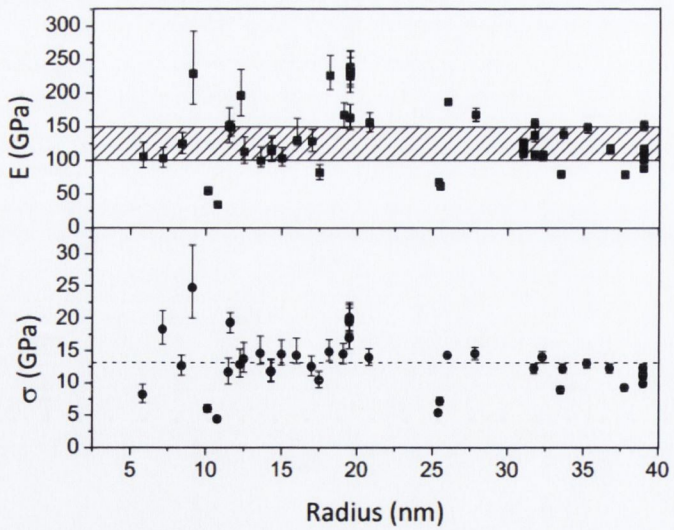

Figure 8: Elastic modulus and yield strength of germanium nanowires as a function of lateral nanowire dimensions. The hashed region in the upper panel represents the bulk modulus for germanium, with the dashed line in the lower panel representing the theoretical strength for germanium.

From figure 8, NWs greater than ~13 *nm* in diameter exhibit both E and σ similar to the values reported previously[10]. However, GeNWs with diameters <13 *nm* displayed significant scatter. The scatter may be a result of two sources; an inhomogeneous/thick oxide along the NW surface and non-cylindrical NWs due to surface faceting, stacking faults and defects. The latter case would change the assumptions of our experiment as we would be dealing with a non-cylindrical structure rather than a uniform cylindrical double clamped beam required by the model. The former case means we are actually dealing with a core-shell structure, and as we do not know the dimensions of the NW oxide, values of E and σ would be invalid.

To determine possible origins of the observed scatter we performed HRTEM on a variety of GeNWs. Figure 9 displays the main types of NWs observed. We observed large oxide thickness varying along the length of the NW, figure 9 (a). We also observed non-cylindrical NWs with high a defect density of stacking faults, figure 9 (b).

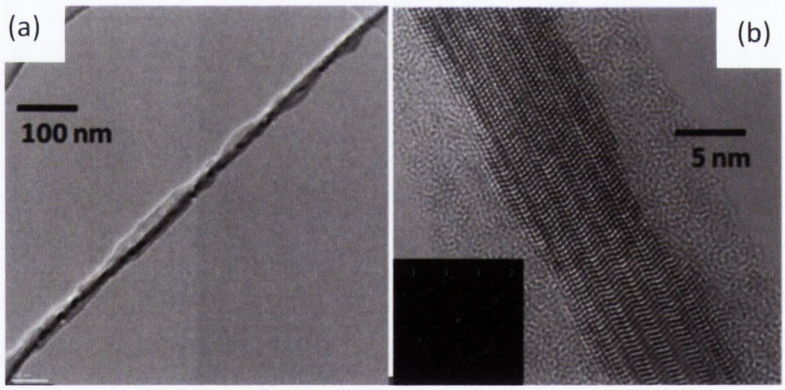

Figure 9: TEM images of GeNWs showing major defects. (a) extremely non-uniform oxide along the length of the wire and (b) HRTEM image of a non-cylindrical NW with a high density of stacking faults. Inset is a diffraction pattern indicative of twinning.

In fact, for GeNWs < 20 *nm* in diameter, Hanrath *et al*[31] showed the variation in growth direction and defect arrangement in GeNWs grown via the vapour-liquid-solid (VLS) method[31]. They found that sub 10 nm NWs displayed surface faceting and <211>-oriented NWs had stacking faults extending down the centre of the wire. Indeed stacking faults or discontinuity in the crystal structure act as nucleation points for fracture under an induced stress[32]. This non-uniformity reduces the mechanical performance of the structure. Figure 10 (i, j) show twinned planes

along the NW long axis, the variation in the number of stacking faults may account for some of the scatter in mechanical data. For NWs less than 20 nm in diameter many cross section geometries were found within the same synthetic batch, figure 10 (a-h). Given that the generalised model assumes a cylindrical geometry[33], the mechanical performance of small NWs may become scattered due to the different cross sectional geometries present. Hence, it is important to correlate the crystal structure to mechanical performance.

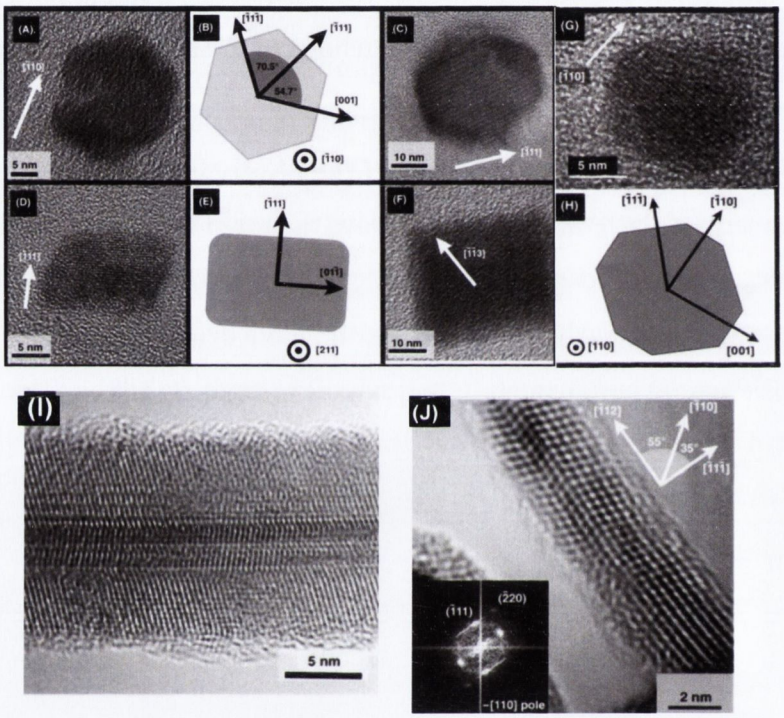

Figure 10: (A-H) Various Germanium NW cross section observed (I) 15 nm diameter NW exhibiting many twinned planes (J) 3 nm diameter NW exhibiting 2 twinned planes[30]

In the next section we outline a TEM/AFM based mechanical characterisation technique to correlate the crystal structure to the mechanical properties of individual GeNWs.

3.3.3 An improved TEM/AFM based mechanical characterisation technique

The GeNWs were dispersed in isopropanol by gentle sonication and drop cast onto a silicon nitride TEM grid. Combined TEM imaging and mechanical measurements were best accomplished using a silicon nitride TEM grid as a nanowire substrate. This type of grid provided a mechanically stiff structure to perform the mechanical measurements on, as well as, a specimen holder for use during TEM imaging. Other

TEM grids, such as lacey carbon grids, were not suitable; the carbon film was not rigid enough and complied as the NW was loaded, hence, the mechanics were actually a measure of the NW/grid relationship and not of the NW itself. The silicon nitride grid consists of a 2. 5 mm hexagonal support frame 200 μm thick with a 500 μm x 500 μm perforated membrane window, 50 nm thick, in the centre of the support frame. The membrane window consists of an array of 2 *μm* holes with a 4 *μm* pitch. Figure 11 shows a GeNW pinned, using Pt-EBID, across a 2 *μm* hole on a silicon nitride grid.

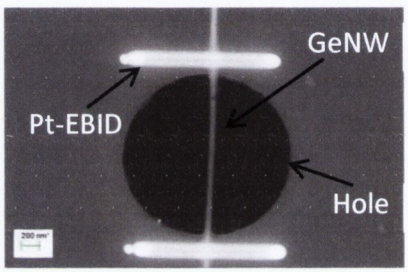

Figure 11: SEM image of Ge NW pinned with EBID-Pt over the 2 μm hole in silicon nitride TEM grid

Figure 12 outlines the experimental steps of the TEM/AFM mechanical measurement technique. Suitable NWs were located using the SEM and pinned at either edge of the hole using Pt-EBID, figure 11. The elastic modulus and strength were measured by the AFM procedure described earlier, and HRTEM performed after mechanical interrogation. It is important to emphasise that the mechanical measurements were not performed *in-situ* on the TEM, mechanical experiments were performed separately in an ambient AFM and the sample was returned to the TEM for high resolution imaging, within 60 *mins* of the mechanical measurement.

Figure 13 shows an f-d curve and TEM image of a 13 *nm* radius GeNW examined using this technique. The NW was not single crystalline as can be seen from the large density of twinned planes in the centre of the NW, figure 13 (b). The analysis of the f-d curve using the generalised model, described earlier, can be used to extract the Young's modulus and strength of the NW. The red curve in figure 13 (a) is the experimental data and the blue line is the fit of the generalised model, equation 1. For this NW the Young's modulus and strength were found to be 43 *GPa* and 5 *GPa* respectively. These values are about three times less than bulk values (103 – 150 *GPa*).

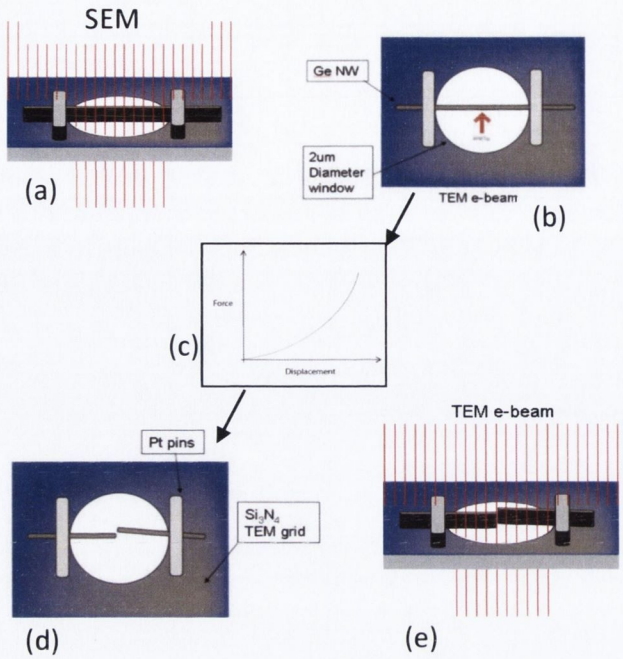

Figure 12: Experimental steps to for combined TEM/AFM mechanical measurements. (a) GeNWs dispersed on the silicon nitride grid are imaged using SEM and clamped to the hole edges by Pt-EBID. (b) Mechanical measurement is performed in air using the lateral AFM approach. (c) the f-d curve from the AFM measurement allows us to extrapolate E and σ. (d) the nanowire is completely fractured by the AFM and imaged using HRTEM (e).

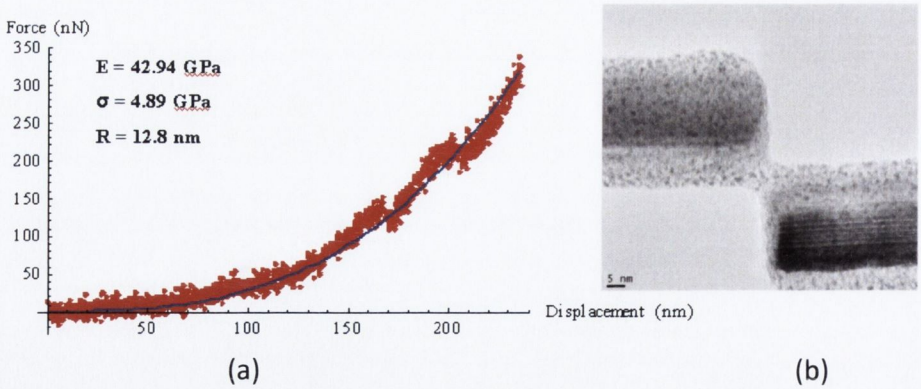

Figure 13: (a) The force-displacement curve for a 12.8 nm radius GeNW. The modulus and strength were given by the blue fit of equation 1 to the red data. (b) HRTEM image of the 12.8 nm radius GeNW. The inferior mechanical characteristics are a result of the thick oxide and high density of stacking faults near the centre of the wire.

Comparing the mechanical response to that of a single crystal GeNW, we see that a single crystal NW displays mechanical characteristics that greatly exceed the bulk value, figure 14. The f-d curve for a 21 *nm* radius single crystal GeNW is shown in figure 14 (a). In this case the NW displays Young's modulus and strength of 371 *GPa* and 28 *GPa* respectively, greatly exceeding bulk (103 – 150 *GPa*). The diffraction pattern in figure 14 (b) shows the wire was single crystalline. HRTEM could not be performed as the wire suffered from of electron beam induced oscillation.

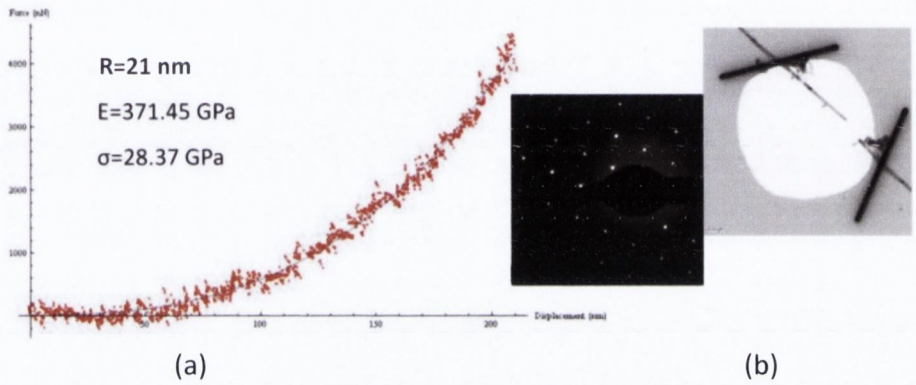

Figure 14: (a) The force-displacement curve for a 21.4 nm radius GeNW. The modulus and strength were given by the blue fit of equation 1 to the red data. (b) TEM image and SAED diffraction pattern of the 21.4 nm radius GeNW. The SAED diffraction pattern shows the NW was single crystalline. The superior mechanical properties may be explained by the highly ordered structure.

This type of mechanical measurement was ideal for correlating the specimen crystallographic structure to the measured elastic modulus and strength, however there are limitations to the technique;

- Performing HRTEM prior to mechanical interrogation is not advisable as the specimen may be damaged by the high energy beam required for high resolution imaging.

- HRTEM imaging post mechanical interrogation is often challenging as the broken NW often suffers from beam induced oscillations, making it difficult to image. Moreover, it is impossible to decipher if any defects, such as twinned planes, present after mechanical characterisation were there before mechanical characterisation, or, are simply a result of mechanical deformation.

- Real time atomic resolution imaging during the deformation process is not accessible, as in other *in-situ* techniques[34].

- The Pt-EBID process can cause material re-deposition on to the specimen obscuring imaging.

The TEM/AFM technique can give an in depth understanding of the mechanical behaviour, indeed an *in-situ* tensile technique for measuring mechanical properties of individual nanowires has been demonstrated[34], although the technique suffers from major limitations, mainly in measuring the mechanical properties of nanowires <100 *nm* in diameter. The TEM/AFM technique developed here overcomes this issue as we have shown the ability to measure the mechanical properties of individual NWs as small as 13 *nm* radius, albeit in a 3-point bending geometry. In order to extend our mechanical technique further and perform uniaxial (purely tensile) mechanical measurements on nanowires with diameters <100 *nm,* we developed a novel AFM technique that uses a similar protocol to that described in chapter 2. In the next section an AFM-based uniaxial loading technique for individual nanowires is described and its limitations discussed.

3.3.4 Uniaxial lateral-AFM measurement technique; Germanium nanowire "pulley system"

Here, we introduce an approach to measure uniaxial deformation of an individual nanowire using lateral AFM. These were the precursor experiments to performing electromechanical measurements using our combined AFM/4-point electrical technique. The mechanical and electromechanical limitations of the "pulley system" will be discussed, with initial experiments using the current technique outlined in the next section.

Figure 15 shows a simplified schematic representation of the experimental approach. The nanowire is double-clamped with a fulcrum point located at some point between the clamped ends, labelled 'pulley' in figure 15. Using an AFM tip, a point load, F, is applied to the centre of only one beam segment, L, with the other passive beam segment, L_e, playing the role of a support structure. The load induced on this passive beam segment depends on the level of friction at the pulley-beam interface and the length of L_e. The pulley does not act as a clamp but rather a

fulcrum by which the nanowire bends and slides around. Ideally, the pulley/nanowire interaction is frictionless, or more realistically less than the breaking strength of the NW itself so the NW slides around the pulley and does not fracture. The bending force on segment L is transformed into purely uniaxial tension over segment L_e by the pulley action.

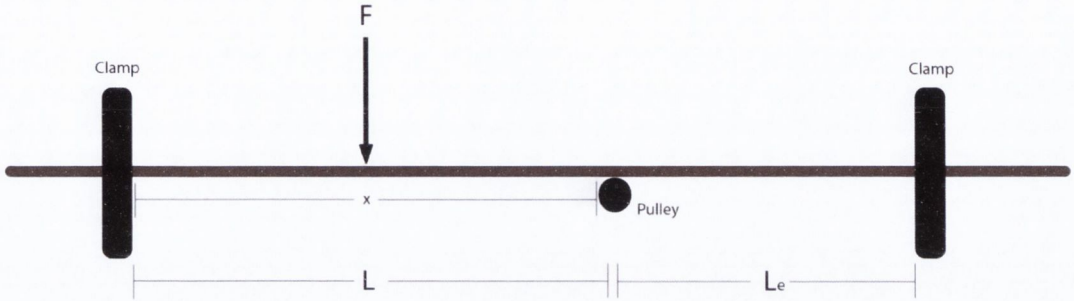

Figure 15: Schematic of the elastic beam with clamped ends and support pulley. Force is applied at centre of load beam segment, L, inducing tension in segment L_e.

Figure 16 shows an SEM image of the experimental setup. The double clamped GeNW spanned over two 2 μm wide trenches, prepared on an Au covered (20 nm Au) SiO_2 substrate by EBL and RIE, with a 500 nm support section, on which the NW sits. The NW was pinned at the outer trench edges using Pt-EBID, a 400 nm high 300 nm diameter platinum pillar fabricated on the centre region acted as the supporting pulley.

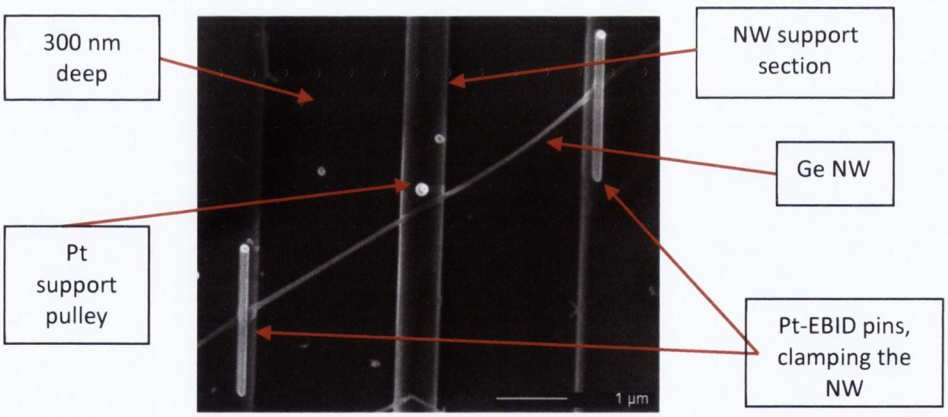

Figure 16: SEM image of the experimental set-up showing a GeNW pinned at the outer edge of two trenches located close a Pt-EBID defined support pulley.

The NW was loaded perpendicular to the NW long axis using lateral-AFM, similar to the 3-point bending technique, at the centre of the loading segment, L; it is not important which segment acts as the loading segment, as long as the wire was

loaded at the centre point ($L/2$) and the dimensions of each segment, L and L_e, were accurately measured.

Figure 17 shows typical experimental results for two individual GeNWs 31 *nm* and 24 *nm* in radius, using this technique. The force-displacement curve for the 31 *nm* wire (figure 17 (a)) displays a Young's modulus and strength of 149 *GPa* and 10 *GPa* respectively, calculated using the generalised model. Elastically brittle behaviour was observed, indicated by the catastrophic failure of the wire at 330 *nm* displacement. The f-d curve displayed clamped-clamped behaviour and fit closely to the clamped-clamped model, showing that the NW did not slide around the support pulley, but rather the support pulley acted as an effective clamp. Figure 17 (b) shows an f-d curve for a 24 *nm* radius GeNW. In contrast to the 31 *nm* NW, the 24 *nm* NW displays an unusual f-d curve artefact at ~250 *nm* displacement. Rather than fracture in the case of double-clamped beam, the NW overcomes its surface bound state and moves around the support pulley, analogous to a nanoscale pulley. The effective change in stiffness is recorded as a change in the slope on the f-d curve. The NW appears to become less stiff, but rather the effective clamped length simply increases as the NW is no longer bound at the support pulley.

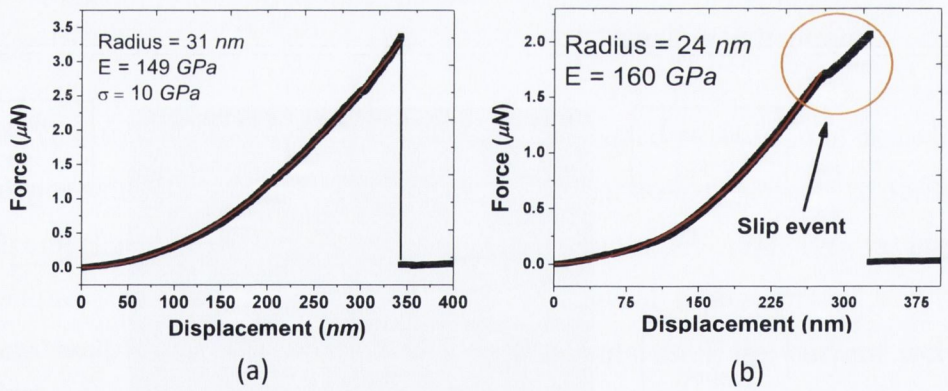

(a) (b)

Figure 17: Force-displacement curves using the "pulley system" for 31 nm and 24 nm radii GeNWs. (a) the 31 nm NW showed clamped-clamped behaviour (b) the 24 nm radius NW displayed a slip event where the NW overcame its surface adhesion.

If we consider the strain $\varepsilon = \Delta L/L$ then it is clear that increasing the length L, whilst maintaining ΔL, will result in a net decrease in strain. Decreasing strain and at a constant stress will result in an apparent reduction in stiffness. Effectively, this is what happens when the NW overcomes the NW/support-pulley surface adhesion; when the NW is bound by the support pulley, as in figure 17 (b) 0 – 240 *nm*, the f-d

curve has a consistent curvature, as described by the generalised model, but when the NW overcomes the support-pulley surface adhesion the curvature changes as the applied strain is spread over a longer wire length.

In the NW/substrate/support-pulley system, adhesive interaction is very important. In order for the NW to slide around the support-pulley the force of interaction must be less than the fracture-force of the wire. The force of interaction can be estimated by calculating the Van der Waals interaction for a cylinder in contact with a flat surface[35];

$$F = \frac{-2AL}{6\pi}\left(-\frac{3\left(\frac{1}{D}\right)^{\frac{3}{2}}\pi.r^2}{4(D+2r)^{\frac{5}{2}}} - \frac{3\left(\frac{1}{D}\right)^{\frac{5}{2}}\pi.r^2}{4(D+2r)^{\frac{3}{2}}} \right)$$

Where F is the force of interaction, L is the length, A is the Hamaker constant, D is the distance from the surface and r is the radius. We approximate the surface-NW distance as $D = 1$ *nm* and the length of surface interaction is 500 *nm* i. e. $L = 500$ *nm*, the NW support section in figure 16. The Hamaker constant for Ge-Au system has been reported previously as 1.0413×10^{-18} *J* [36]. Here, we make several assumptions in the calculation. We assume uniform contact of the NW with the surface and ignore the presence of NW surface oxide, as well as adsorbates from the atmosphere. The NW's are also assumed to be perfect cylinders i. e. with no surface faceting, the surface to be perfectly flat and that each atom in the NW interacts with the surface atoms with an equal magnitude.

Figure 18 (a) shows the calculated adhesion force between a Ge cylinder on a gold surface as a function the cylinder radius, given by the red line. The circular symbols represent experimental data for the fracture force of individual GeNWs at various radii. For GeNW radii <18 *nm* the adhesion force to the surface is greater than the fracture force. Hence, upon loading the NW cannot overcome adhesion to move around the support pulley. Radii between ~ 20 – 33 *nm* show intermediate adhesion characteristics by which a percentage of NWs may have the strength to overcome the bound state upon loading. Beyond 33 *nm* radius the NWs have a fracture force greater than the bound state force, meaning NWs >30 *nm* in radius can overcome adhesion and move across the pulley without fracturing. Figure 18 (b, c) show f-d curves for two un-clamped 9 *nm* and 70 *nm* radius NWs, (b) and (c)

respectively, representative of two systems where one NW should be clamped by the surface and one should overcome the adhesion before fracture. Figure 18 (b) shows a small NW with a 9*nm* radius. The f-d curve shows typical elastic-brittle behaviour, even though the NW was not clamped at the trench edges. Hence, surface adhesion itself acts to clamp the NW. However, the 70 *nm* radius NW, figure 18 (c), showed unusual f-d behaviour. From figure 18 (a) a radius >33 *nm* falls above the critical radius to overcome surface adhesion. Instead of fracturing like their smaller counterparts, the larger NWs can slip when the applied force overcomes surface adhesion. The saw tooth behaviour in figure 18 (c) is due to the NW re-adhesion to the surface. Hence the AFM tip must dislodge the NW repeatedly during the course of the lateral drive.

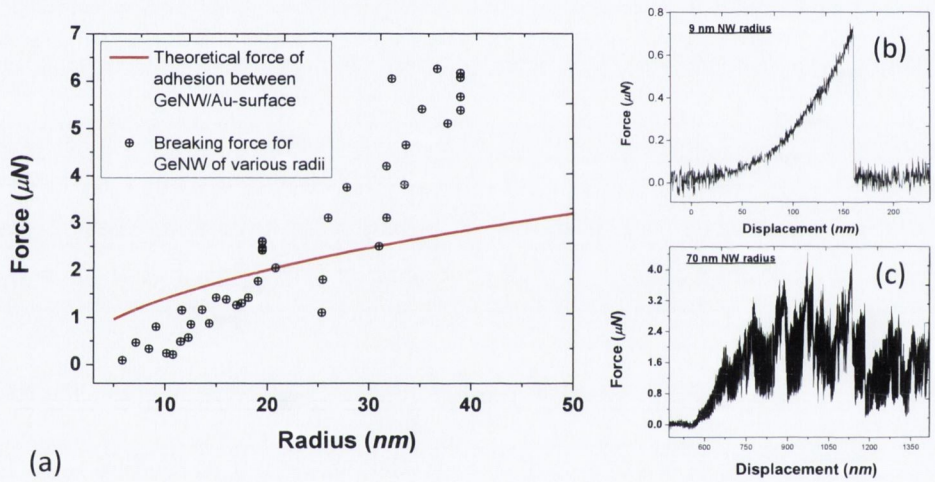

Figure 18: (a) Theoretical adhesion force of a germanium cylinder to a gold surface as a function of cylinder radius, red curve. The circular symbols are experimental data for the breaking force of GeNWs at various radii. (b) f-d curve for a substrate clamped GeNW showing double-clamped behaviour as expected. (c) An un-clamped GeNW slipping across a surface upon loading from an AFM tip.

On this basis we were limited to reliably measuring NWs >33 *nm* in radius. We could further reduce the measurable dimensions by reducing the width of the NW support region, hence decreasing the surface interaction area. However, this was not attainable as a 500 *nm* support region was required to fabricate the support pulley.

As well as studying the uniaxial mechanical properties of individual NWs it was envisaged we could apply a similar experimental system to probing the electromechanical properties of individual NWs, under uniaxial tension. In the next

section we describe an experimental approach to measuring the electromechanical properties of individual GeNW.

3.4 Electromechanical measurements on Germanium nanowires: Challenges with semiconducting nanowires

3.4.1. Electromechanical measurements of GeNWs using the "pulley system" mechanics

We proposed to measure the 4-point resistance of an individual GeNW whilst mechanically loading the wire using the "pulley system" approach. A schematic of the experimental set-up is shown in figure 19; an individual GeNW was placed in contact with the top surface of four lithographically defined Au electrodes, including the support pulley. The NW was pinned to electrodes 1, 2 and 4 by W-EBID to ensure a good electrical contact. Contact to electrode 3 was established during the loading process as the NW moved around the support pulley. It was envisaged that the AFM tip would load the NW between electrodes 3 and 4, inducing tension in the NW section between 2 and 3. The 4-point measurement and uniaxial deformation would give the strain dependent electrical properties of the GeNW.

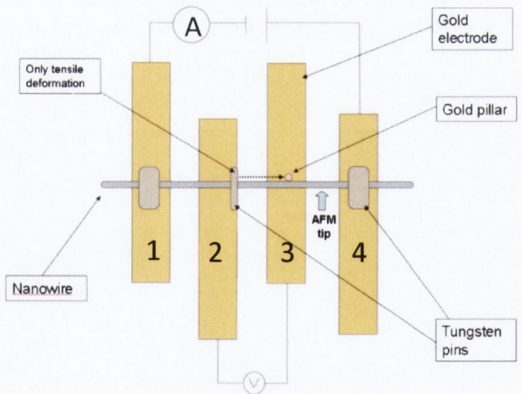

Figure 19: Schematic for the "pulley system" electromechanical set-up

However, there were major limitations to the technique;

- We were limited to NWs > 33 *nm* in radius due to surface adhesion issues
- As the NW was loaded around the support pulley, the electrical contact changed as the force between the pulley and NW increased. The contact resistance changed in response to the load, making it impossible to elucidate if any change

in resistance or resistivity during the loading process was a function of the NW or simply of the NW/pulley interaction.

In the next section we discuss the electromechanical properties of GeNWs in terms of the lateral-AFM 3-point bending mechanical technique.

3.4.2. Electromechanical measurements on GeNWs using the 3-point bending technique

To overcome unpredictable contact resistance during the loading process, an alternative technique was devised to electromechanically probe individual NWs. This involved measuring the electrical properties via 4-point resistance measurement, and the mechanical properties via the lateral AFM 3-point bending technique, outlined in chapter 2. The electromechanical technique is described extensively in chapter 2. Here, we will discuss the results and challenges in measuring the electromechanical properties of GeNWs.

Figure 20 shows the experimental results for a 27 *nm* radius GeNW. An SEM image of the suspended GeNW contacted with four Au electrodes is shown in figure 20 (a). The voltage was sourced, V_s, and the current was measured, I_m, across the outer electrodes 1 and 4. The voltage across the specimen, V_m, was measured across the inner electrodes 2 and 3. The 4-point IV characterisation, shown in figure 20 (b), gives a resistance of 112 $M\Omega$. Comparing the 2-/4-point resistance gave a contact resistance of >5 $G\Omega$. A large contact resistance was expected as the NW-surface was coated in a poorly conductive GeO_x oxide. We found the resistivity to be 0. 14 *Ohm m*, a reasonable value given that the NWs were un-doped. The force-displacement (f-d) and resistance-displacement curves are shown in figure 20 (c), lower and upper panels respectively. The Young's modulus, E, and strength, σ, were found to be 179 *GPa* and 6 *GPa* respectively, given by the red fit of the generalised model (equation 1) to the black curve in figure 20 (c), lower panel. As the NW was displaced there was no observed change in resistance, figure 20 (c) upper panel. This was more than likely a result of the poor signal to noise (75 – 125 $M\Omega$ noise), rather than a direct reflection of the NW behaviour as other reports have shown massive changes in resistance as a function of strain for individual GeNWs[27].

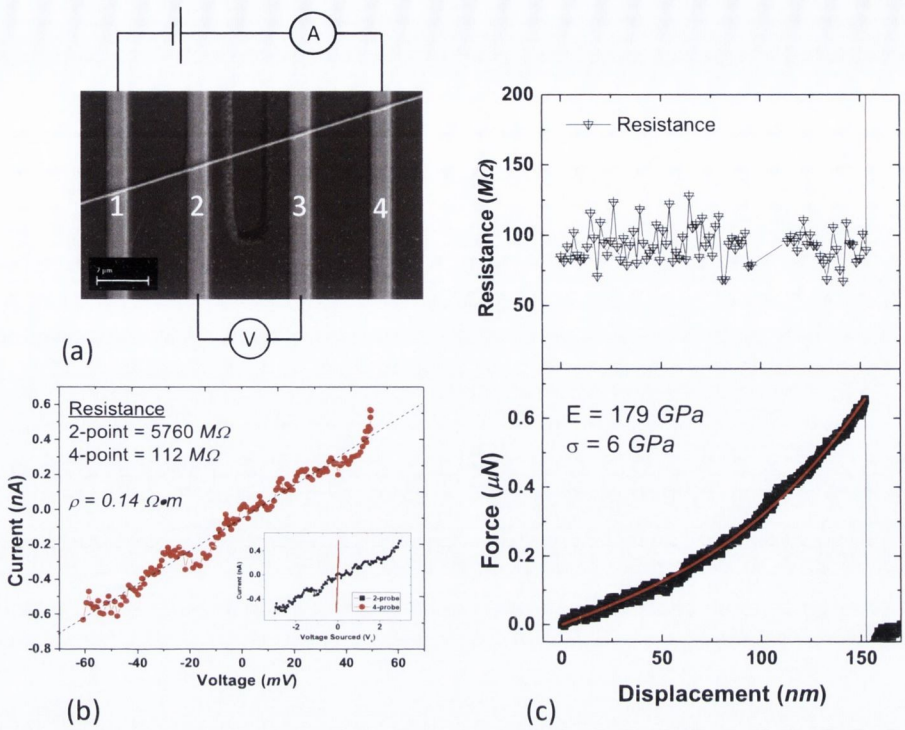

Figure 20: (a) SEM image of a GeNW contacted by four EBL defined Au electrodes. The voltage was sourced and the current was measured across the outer electrodes 1 and 4. The voltage drop across the specimen was measured across the inner electrodes 2 and 3. (b) Typical 4-point IV curve of a GeNW, inset shows both 2- and 4-point measurements. (c) Upper panel shows the change in resistance as a function of displacement, the lower panel showing the f-d curve, black data, with the red fit of equation 1 describing the mechanical properties.

The high resistance observed in un-doped GeNWs was at the limit of the tools resistance measurement capabilities, due to the small currents and voltages measured. Working near the limit of the tools capabilities introduced large levels of noise into the data, shown in figure 20 (c) upper panel; giving noise levels over tens of $M\Omega$. Hence, even a very large change in resistance of several $M\Omega$ would be completely obscured by noise. This result prompted us to measure the electromechanical properties of metallic nanowire systems, silver and nickel.

Being good conductors, the measured voltage and current were $x10^3$ larger than that of semiconducting NWs, resulting in routine resistance measurement sensitivity of 0.01 Ω. Generally Ag and Ni NWs were easier to handle as the synthetic dispersion was cleaner, with a better size distribution. This resulted in more accurate and reliable mechanical and electrical characterisation, as well as electromechanical characterisation. In addition, the electromechanical properties

of metallic NWs are actually very important for applications in transparent, flexible conducting electrodes and NEMS devices. In chapters 3 and 4 we extensively describe the electromechanical properties of individual AgNWs, comparing our results with the same measurement on individual NiNWs.

3.5 Conclusion

The mechanical properties of germanium nanowires between 10 – 80 *nm* in diameter were mechanically tested using the lateral-AFM 3-point bending method. Large scatter in the values of the measured Young's modulus and strength was observed for NWs below 25 *nm* in diameter. In order to probe the scatter in the data an extensive HRTEM study was performed, which then showed the NWs to display a high density of stacking faults and non-uniform oxide thickness along their length. As a result the TEM/AFM based mechanical analysis technique was developed. Individual GeNWs were pinned on a silicon nitride TEM grid and mechanically interrogated using the lateral-AFM 3-point bending method. Subsequently, the NWs were imaged using HRTEM. The atomic structure of the NW, combined with the modulus and strength from the AFM provided insights into the effects of stacking faults on their mechanical properties. As the TEM/AFM technique would not be suitable for electromechanical measurements, a "pulley" based mechanical loading system using an AFM tip was devised to measure the uniaxial deformation of individual GeNWs. Although we demonstrated the ability of an individual GeNW to slide around a support pulley, it was not suitable for electromechanical measurements as the support-pulley/NW contact resistance would evolve with the applied load, as well as, NW dimension limitations (must be >33 *nm* in radius) due to surface adhesion. As such a 4-point electrical measurement coupled with the lateral-AFM 3-point bending method was devised to measure the electromechanical properties of GeNWs. However, its implementation was limited by the high resistance of the un-doped NWs and the inability to measure small resistance changes (noise over tens of $M\Omega$) due to the very small currents involved. In light of this we instead measured the electromechanical properties of metallic NWs as the measured voltage and current were $x10^3$ larger than that of semiconducting NWs, resulting in routine resistance measurement sensitivity of 0.01 Ω.

This chapter has given an insight into the development of the mechanical and electromechanical technique showing the current limitations within semiconducting systems. We would envisage that improving the technique would yield the desired signal to noise for measuring semiconducting NWs in the future. In the next chapter we describe electromechanical measurements on individual silver nanowires in terms of their strain dependent electrical properties.

3.6 References

1. Xia, Y., et al., *One-Dimensional Nanostructures: Synthesis, Characterization, and Applications.* Advanced Materials, 2003. **15**(5): p. 353-389.
2. Lieber, C.M., *Nanoscale science and technology: Building a big future from small things.* MRS Bull., 2003. **28**(7): p. 486-491.
3. Cui, Y., et al., *Nanowire Nanosensors for Highly Sensitive and Selective Detection of Biological and Chemical Species.* Science, 2001. **293**(5533): p. 1289-1292.
4. Wortman, J.J. and R.A. Evans, *Young's Modulus, Shear Modulus, and Poisson's Ratio in Silicon and Germanium.* Journal of Applied Physics, 1965. **36**(1): p. 153-156.
5. Roundy, D. and M.L. Cohen, *Ideal strength of diamond, Si, and Ge.* Physical Review B, 2001. **64**(21): p. 212103.
6. Tabib-Azar, M., et al., *Mechanical properties of self-welded silicon nanobridges.* Applied Physics Letters, 2005. **87**(11): p. 113102-113102-3.
7. Sohn, Y.-S., et al., *Mechanical Properties of Silicon Nanowires.* Nanoscale Research Letters, 2010. **5**(1): p. 211-216.
8. Kim, Y.-J., et al., *Exploring Nanomechanical Behavior of Silicon Nanowires: AFM Bending Versus Nanoindentation.* Advanced Functional Materials, 2011. **21**(2): p. 279-286.
9. Wu, X., et al., *Synthesis and Electrical and Mechanical Properties of Silicon and Germanium Nanowires.* Chemistry of Materials, 2008. **20**(19): p. 5954-5967.
10. Ngo, L.T., et al., *Ultimate-Strength Germanium Nanowires.* Nano Letters, 2006. **6**(12): p. 2964-2968.
11. Smith, D.A., et al., *Young's Modulus and Size-Dependent Mechanical Quality Factor of Nanoelectromechanical Germanium Nanowire Resonators.* The Journal of Physical Chemistry C, 2008. **112**(29): p. 10725-10729.
12. J. J. Wortman, R.A.E., *Young's Modulus, Shear Modulus, and Poisson's Ratio in Silicon and Germanium.* Journal of Applied Physics, 1965. **36**: p. 153.
13. V. G. Lyuttsau, Y.M.F., I. L. Svetlov, Sov. Phys. Crystallogr, 1966. **10**: p. 707.
14. Wen, B., J.E. Sader, and J.J. Boland, *Mechanical Properties of ZnO Nanowires.* Physical Review Letters, 2008. **101**(17): p. 175502.
15. Jang, J.E., et al., *Nanoelectromechanical switches with vertically aligned carbon nanotubes.* Applied Physics Letters, 2005. **87**(16): p. 163114-3.
16. Qiliang, L., et al., *Precise Alignment of Single Nanowires and Fabrication of Nanoelectromechanical Switch and Other Test Structures.* Nanotechnology, IEEE Transactions on, 2007. **6**(2): p. 256-262.

17. Husain, A., et al., *Nanowire-based very-high-frequency electromechanical resonator.* Applied Physics Letters, 2003. **83**(6): p. 1240-1242.
18. Feng, X.L., et al., *Very High Frequency Silicon Nanowire Electromechanical Resonators.* Nano Letters, 2007. **7**(7): p. 1953-1959.
19. Koumela, A., et al. *Performances of suspended Silicon Nanowire Resonators for time reference applications*. in *Frequency Control Symposium (FCS), 2012 IEEE International*. 2012.
20. Andzane, J., et al., *Two-Terminal Nanoelectromechanical Devices Based on Germanium Nanowires.* Nano Letters, 2009. **9**(5): p. 1824-1829.
21. Ziegler, K.J., et al., *Bistable nanoelectromechanical devices.* Applied Physics Letters, 2004. **84**(20): p. 4074-4076.
22. Hall, H.H., J. Bardeen, and G.L. Pearson, *The Effects of Pressure and Temperature on the Resistance of p-n Junctions in Germanium.* Physical Review, 1951. **84**(1): p. 129-132.
23. Smith, C.S., *Piezoresistance Effect in Germanium and Silicon.* Physical Review, 1954. **94**(1): p. 42-49.
24. Li, M., *Review of advanced CMOS technology for post-Moore era.* Science China Physics, Mechanics and Astronomy, 2012. **55**(12): p. 2316-2325.
25. Hong, K.-H., et al., *Strain-Driven Electronic Band Structure Modulation of Si Nanowires.* Nano Letters, 2008. **8**(5): p. 1335-1340.
26. Vo, T., A.J. Williamson, and G. Galli, *First principles simulations of the structural and electronic properties of silicon nanowires.* Physical Review B, 2006. **74**(4): p. 045116.
27. Greil, J., et al., *Tuning the Electro-optical Properties of Germanium Nanowires by Tensile Strain.* Nano Letters, 2012. **12**(12): p. 6230-6234.
28. T. Hanrath, B.A., Korgel, Journal of American Chemistry Society, 2002. **124**: p. 1424.
29. Almecija, D., *Ph. D thesis, Mechanical Properties of One-Dimensional Nano-Systems.* 2010.
30. Heidelberg, A., et al., *A Generalized Description of the Elastic Properties of Nanowires.* Nano Letters, 2006. **6**(6): p. 1101-1106.
31. Hanrath, T. and B.A. Korgel, *Influence of Surface States on Electron Transport through Intrinsic Ge Nanowires.* The Journal of Physical Chemistry B, 2005. **109**(12): p. 5518-5524.
32. T. Zhu, J.L., *Ultra-Strength Materials* Progress in Material Science, 2010. **55**: p. 710-757.
33. Bin Wu, A.H., John J. Boland, *Mechanical properties of ultrahigh strength gold nanowires.* Nature Materials, 2005. **4**(525-529).
34. Yong, Z., C. Alberto, and D.E. Horacio, *A thermal actuator for nanoscale in situ microscopy testing: design and characterization.* Journal of Micromechanics and Microengineering, 2006. **16**(2): p. 242.
35. Israelachvili, J.N., *Intermolecular and Surface Forces* Academic Press, 1992.
36. Matijevic, E., *Surface and Colloid Science, vol 8.* john Wiley & Sons, Inc. New York, 1976: p. 29.

Chapter 4: The strain dependent electrical properties of Silver and Nickel Nanowires

4.1. Motivation

Metallic nanowires (NW) have attracted considerable interest as nanoscale interconnects and as both active components in electrical and electromechanical devices[1, 2]. In the drive to implement them into functional devices, their electrical and mechanical properties have been extensively studied. However, their electromechanical behaviour has received much less attention, mainly due to the difficulty in handling these materials and performing nanoscale electrical and mechanical measurements simultaneously. Silver nanowires (AgNW) have received extensive attention in a wide range of applications from *in-vitro* pulmonary inflammation studies[3] to flexible, transparent electronics[4-6].

NEMS have received more and more attention over the past few years. This type of device provides considerably lower leakage than conventional transistor devices[7], making them attractive for on-chip devices to lower power consumption[8]. Nanowire based NEMS constructed from many different types of materials have been studied, however, there remains an important characteristic that is not generally measured for nanowire systems - the effect of strain on transport, known as the electromechanical property. A NEMS device always has a deformable electrical component connecting the source and the drain under the control of a gate. Hence, one or many of the components are being strained while they are electrically active. Moreover, if we consider any NW electrical component, the reduction in NW dimensions means they undergo increased strain as fabricated i. e. the strain imposed on the NW in a device is created by its surroundings. In order to implement nanowires into functional devices it is imperative that these electromechanical properties are understood.

In 2012 Loh *et al*[9] published an extensive review on NEM contact switches. In terms of NEMS, many different device architectures have been fabricated to produce different functionalities. Figure 1 reviews a few of the most common architectures.

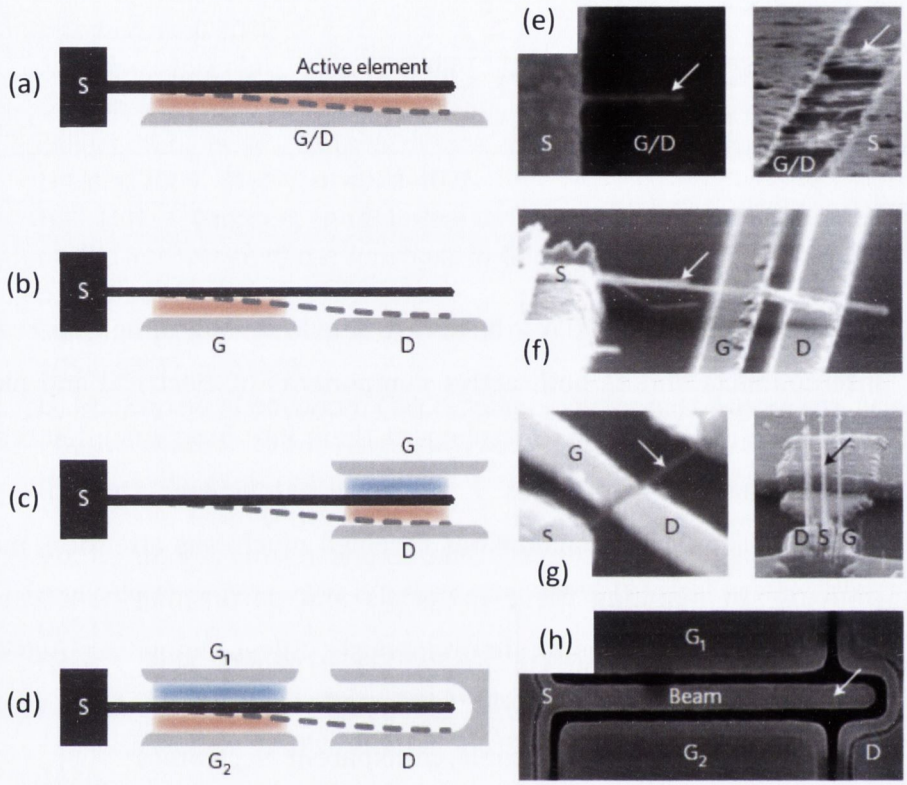

Figure 1: Review of the most common NEMS structures: (a-d) schematics showing the source, drain, gate and active element for different structures. (e-h) show SEM images of the real devices depicted in the schematics. The white arrows highlight the active element [9-15].

In two-terminal devices a single opposing electrode is used as a gate, *G*, and a drain, *D*. The dual *G/D* electrode controls the device by pulling the active element into contact. Figure 1 (a) shows a schematic of several two terminal NEMS device. The SEM images in figure 1 (e) show two terminal CNT NEMS devices[10, 11]. Figure 1 (b-d) and (f-h) show more complex structures, where the gate and drain are separate electrodes[12], Figure 1 (b, f). The gate and drain may sandwich the active element, as shown in figure 1 (c, g)[13, 14], or multiple gates may control the active element[15], figure 1 (d, h). Simply by its definition, no matter how a NEMS structure is designed, fabricated or functioned, there is always a deformable component. We can see from figure 1 that the active element, indicated by the white arrow, in each of the devices must bend to contact the drain electrode in order for the device to function. Hence,

it is extremely important to electromechanically characterise the active element in terms of bending and not simply under tensile deformation, as this does not generally reflect NEMS functionality. Other reports have focused on measuring the electromechanical properties of NW systems under purely tensile conditions[16-19].

In 2013 Hongjiang *et al*[19] measured the electromechanical properties of Cu and SiC NW using an *in-situ* SEM tensile device. The Cu NW was mounted onto the tensile device by a micromanipulation needle. Good electrical contact between the CuNW and the metallic leads was ensured by Pt-EBID pinning, figure 2 (a).

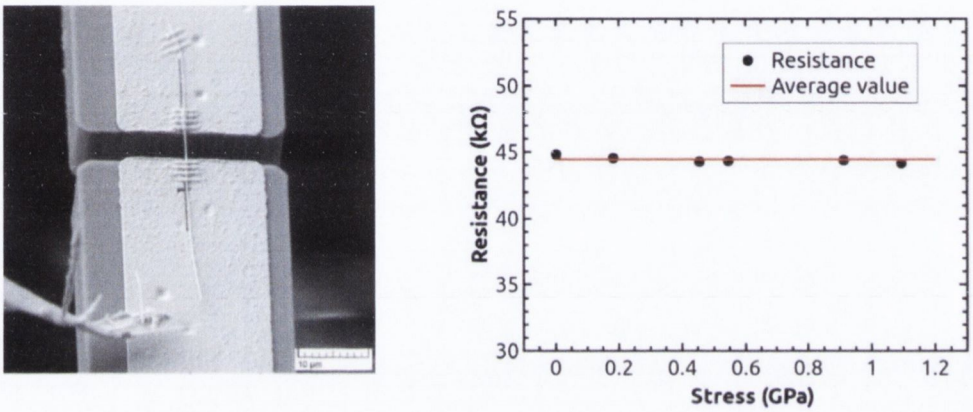

(a) (b)

Figure 2: The electromechanical properties of a Cu NW. (a) SEM image of the Cu NW mounted on to the tensile device. The NW bridges the two electrical contacts, secured by Pt-EBID. (b) change in resistance with increasing stress for an individual Cu NW [19].

Figure 2 (b) shows the change in resistance of a 220*nm* diameter CuNW with applied stress. The Cu NW shows no change in resistance with stress, albeit within the limits of a much reduced resistance sensitivity measurement. Rather importantly, a 2-point electrical measurement approach was applied. As such, the true resistance of the nanowire cannot be measured during loading. Moreover, the electrical contacts to the NW also act as the mechanical clamps. Hence, the contribution of strain to the resistance at the NW/contact junction cannot be quantified nor measured. In earlier reports by Espinosa *et al*[16, 20] presented an improved 4-point MEMS based tensile stage, however, no experimental results were presented.

Conductive AFM (C-AFM) methods have been used to perform 2-point electrical strain measurements on individual NW systems[21, 22]. In this type of C-AFM a

conductive AFM tip is used to bend an individual NW and measure the electrical properties as a function of load. This type of measurement is not ideal for 2 reasons;

1. It's a 2-point electrical measurement,
2. The contact force, and hence the resistance, between the AFM tip (also acting as one of the electrical contacts) and the NW constantly changes during loading.

The AFM based technique we have developed, described in chapter 2, allows us to measure the 4-point resistance as a function of strain under both bending and tensile loading conditions.

In this chapter the strain dependent electrical properties of AgNWs are presented and compared to the same measurement on nickel nanowires. We discuss an electromechanical approach to estimating the Poisson's ratio and gauge factor of individual nanowires. We first describe the synthesis and structure of Ag and Ni NWs. The strain dependent electrical properties are then described and analysed in terms of a new generalised model.

4.2. Nanowire Synthesis and Structure

4.2.1 Silver nanowire synthesis and structure

The AgNWs used for this study were purchased from Seashell Technology[23, 24]. NWs are synthesised by the solution based polyol process. There have been many reports on the polyol process synthesis of silver nanomaterials[25-29]. Here, the main aspects of the synthetic process are described.

Polyol synthesis of silver nanowires involves the reduction of silver nitrate ($AgNO_3$) by anhydrous ethylene glycol. The liberated silver atoms produce the nanostructure. The polyol serves as a solvent for the silver compound as well as the reaction. An organic protective agent, polyvinylpyrrolidone (PVP), is added to the reaction solution to coat and stabilise the nanostructure during the synthesis process, helping to avoid severe agglomeration. The nanowires are synthesised at temperatures between 130 – 140 °C, resulting in diameters between 40 - 95 *nm*, lengths between 5 – 15 μm and aspect ratios >50.

The structure of the Ag NW's has been studied using HRTEM. The NW's have a [011] FCC structure, with a fivefold twin running along their length[30]. Figure 3 (a) shows a cross section of a single Ag NW prepared by FIB milling. The five twinned planes are indicated with a dashed line for clarity. The diffraction pattern confirms the fivefold twin, shown in figure 3 (b). Figure 3 (c) shows a schematic of the unit cell crystallographic directions, with figure 3 (d) showing a schematic of the fivefold symmetry running along the length of the wire. TEM analysis also shows the PVP coating the NW surface, highlighted by the blue circle in figure 4 (a). The Fast Fourier Transform (FFT) in figure 4 (b, c) show the crystal structure within the red and green boxes indicated on the TEM image in figure 4 (a).

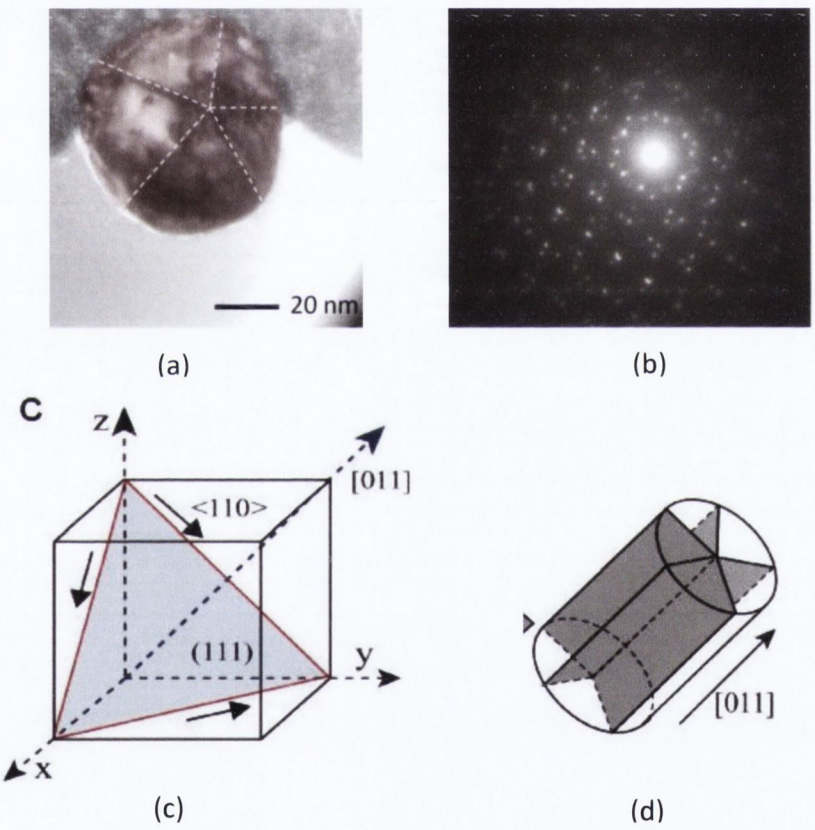

Figure 3: (a) Cross section TEM image of an Ag NW, (c) diffraction pattern showing the fivefold symmetry, (c) schematic of the unit cell crystallographic directions and (d) a schematic of the fivefold twin running along the NW's length[30, 31].

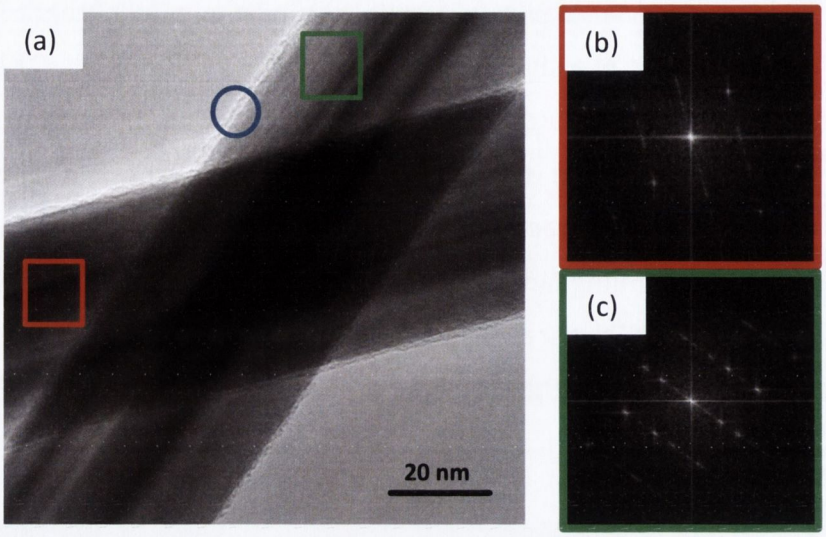

Figure 4: (a) TEM of two crossed Ag NW's. The blue circle highlights the amorphous PVP coating. (b) shows a FFT of the region highlighted by the red box in (a). (c) shows the FFT of the region within the green box in (a).

The NWs are dispersed in isopropanol and stirred for 30 *sec* before they are drop-cast on to the pre-patterned substrate. Although our main interest lies in AgNWs, a direct comparison is made to the same measurements on NiNWs. In the next section the synthesis and structure of nickel nanowires is described.

4.2.2 Nickel nanowire synthesis and structure

The nickel nanowires (NiNW), purchased from Nanomaterials.it[31], were synthesised by template directed electrodeposition. The template consists of anodised-aluminium-oxide (AAO) coated on one side with an Au layer which acts as the cathode during the electrodeposition step. The high density, ordered, and high aspect ratio pores in the AAO template are ideal for NW synthesis. The AAO template was placed in a Ni salt electrolyte with an inert metal anode. A potential difference induced between the cathode and the anode results in the electrodeposition of Ni, from the Ni salt, into the pores in the AAO. The NWs grow within the pores in the AAO, resulting in high aspect ratio NWs. The NWs were released from the AAO template as follows; 30 % HNO_3 was used to remove electrodeposited Ni from the backside of the Au coating. Gentle exfoliation using an Au etchant (Ge8148) was used to remove the Au back contact. The AAO matrix was removed by immersing the

template in 3M NaOH for 24 *hrs*. The NWs were rinsed in deionised water and dispersed in IPA.

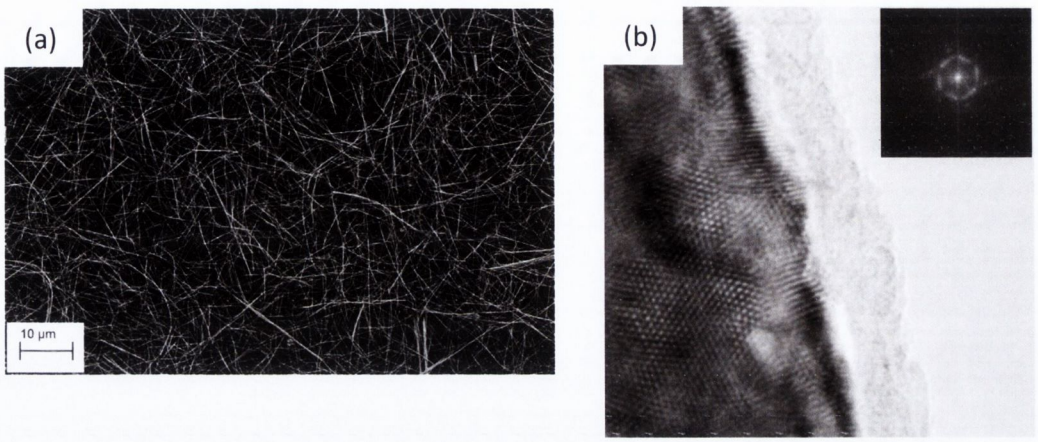

Figure 5: (a) SEM image of NWs after removal from the AAO template. (b) HRTEM image of an individual nickel nanowire. The NW is polycrystalline with a 4 – 8 nm surface oxide. Inset is a FFT showing a typical diffraction pattern for a polycrystalline material. (5 nm scale bar)

The structure of the NiNWs was studied by SEM and HRTEM. Figure 5 (a) shows a SEM image of the wires after AAO removal. The removal process is non-destructive as the NWs appear to have a relatively smooth surface as well as maintaining the high aspect ratio of the AAO pores. Figure 5 (b) shows a HRTEM image of an individual NiNW. The NWs are polycrystalline with a surface oxide thickness between 4 – 8 *nm*. The FFT inset, taken from the core of the NW in the image, shows a typical diffraction pattern for a polycrystalline material. Polycrystalline NiNWs were an ideal comparative material against the single crystal AgNWs, where both are highly pure metals exhibiting similar electrical and mechanical characteristics in their bulk form. The only substantial difference between both NWs is the crystal structure; hence, we can directly compare the electromechanical properties between single crystal and polycrystalline NWs.

In the next section results on the strain dependent resistance, Poisson's ratio and gauge factor of AgNW are presented, making direct comparisons with the same measurement on NiNW. Firstly, we outline the electrical and mechanical properties of both materials.

4.3. Results

4.3.1 Mechanical and Electrical properties of individual Ag NW

Here, the mechanical and electrical properties of AgNWs are presented. The mechanical properties were measured using the lateral-AFM 3-point bending technique and the electrical properties were measured by the 4-point resistance method, both described in chapter 2. Figure 6 (a) shows a typical AFM image of a suspended pentagonal Ag NW contacted with four Ag-electrodes ~500 *nm* wide. Figure 6 (b) shows a typical force-displacement (F-d) curve for the pentagonal Ag NW which was analysed using a generalised model that accounts for both bending and tensile deformation [32];

$$F_{center} = \frac{192EI}{L^3} f(\alpha)\Delta z_{center} \quad (1)$$

where F is the applied force, E is Young's modulus, I is the areal moment of inertia, Δz_{center} is the lateral displacement and the $f(\alpha)$ term accounts for tensile deformation along the nanowire. A full description of the mechanical model is described in the appendix. The red curve in figure 6 (b) is the fit of equation 1 to the data (black curve). The elastic modulus was found to be 86 ± 10 *GPa* for this 90 *nm* diameter nanowire. Generally, we found E to be between 40 - 160 *GPa* for individual pentagonal Ag NW's agreeing with previously reported values[33-35]. Figure 6 (c) shows a typical 4-point IV for an individual suspended pentagonal Ag NW, the inset shows both 2- and 4-point measurements. The voltage was sourced and the current was measured across the outer electrodes 1 and 4, the voltage was measured across the inner electrodes 2 and 3, shown in figure 6 (a). As expected the 2-point measurement is dominated by the contact resistance. The NW is ohmic with a resistance, $R = 15.5\,\Omega$. In general, $R \sim 15$ -70 Ω, depending on the diameter and length of the NW, with $\rho \sim 17 - 35$ nΩ m. Figure 6 (d) shows the NW resistivity increases with decreasing radius, consistent with the general trend in the literature [36]. In addition, the resistance and resistivity values agree with previously reported measurements on similar nanowires[30].

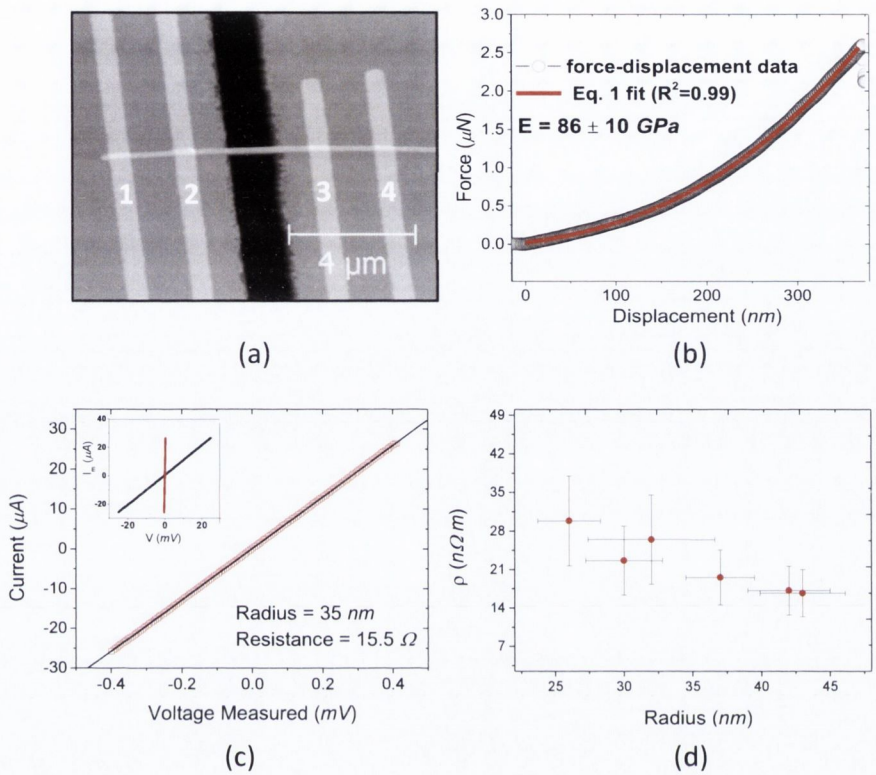

Figure 6: (a) AFM image showing an individual suspended Ag NW spanning a trench contacted with 4 silver electrodes. (b) A typical f-d curve for an Ag NW, showing elastically brittle behaviour and a fit to equation 1 (red curve). The elastic modulus was found to be 86 ± 10 GPa, the black data shows the residuals to the fit (c) 4-point IV characterisation of an individual Ag NW, 2- and 4-point inset. The linear fit gives a resistance of 15.5 Ω, and (d) the resistivity as a function of NW radius.

The mechanical and electrical properties of NiNWs are outlined in the next section.

4.3.2 Mechanical and Electrical properties of individual Ni NW

The mechanical and electrical properties of NiNWs were measured by the lateral-AFM 3-point bending technique and the electrical properties were measured by the 4-point resistance method, similar techniques to that used for AgNWs and are both described in chapter 2. Figure 7 (a) shows a typical force-displacement curve for an individual 28 *nm* radius NiNW. In contrast to AgNW which underwent brittle failure, characteristic elastic and plastic deformation for a polycrystalline NiNW was observed. The region between 0 – 85 *nm* is the elastic region where the NW

undergoes reversible deformation. The yield point, at ~90 *nm* displacement, is the force at which the NW yields, beyond which plastic deformation was observed. Complete fracture of the NW occurred at ~130 *nm* displacement. The red curve in figure 7 (a) is a fit of equation 1 to the filled symbols, giving E = 154 *GPa* and σ = 6.9 *GPa*. The force-displacement behaviour observed in this study is consistent with other reports on individual NiNWs[37].

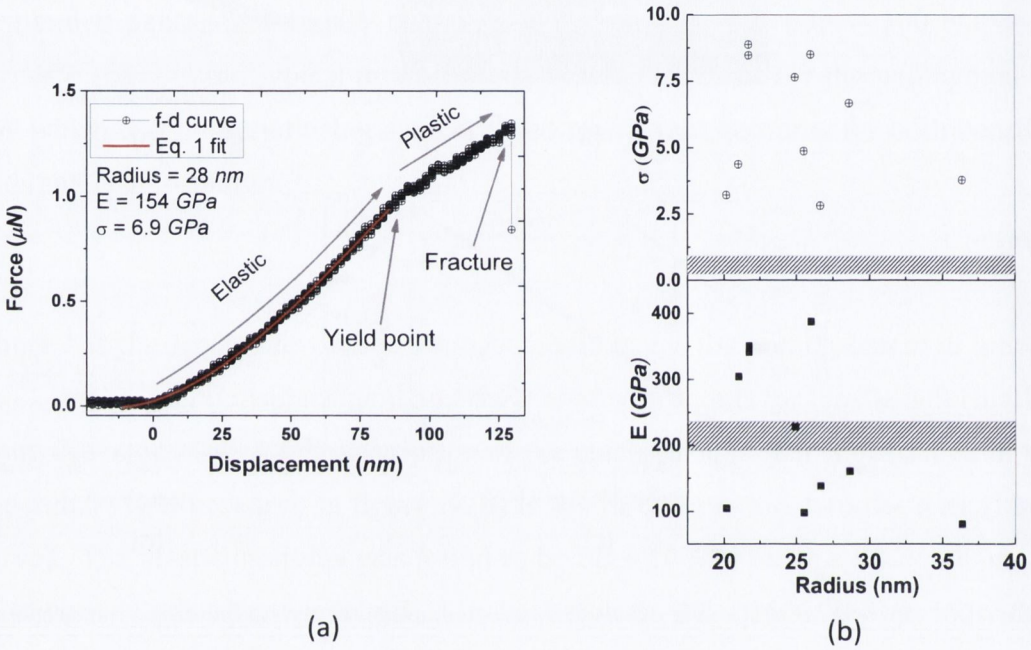

Figure 7: (a) Typical force-displacement curve for a 28 nm radius NiNW showing elastic and plastic deformation components. (b) The Young's modulus, lower panel and yield strength, upper panel as a function of NW radius for several NiNWs.

Several NWs were tested in the same manor and analysed using our model. Figure 7 (b) shows the Young's modulus, lower panel, and strength, upper panel, for NiNWs of radii between 20 – 38 *nm*. The hashed region in the lower panel represents the Young's modulus for bulk electroplated nickel (190-236 *GPa*)[38-41], with the hashed region in the upper panel representing the yield strength of bulk electroplated nickel (0. 28-0. 93 *GPa*)[39, 41, 42]. Large scatter was observed mainly due to uncertainties in the model stemming from uncertainty in the oxide thickness. The surface oxide was generally between 4-8 *nm* thick. The model assumes a cylindrical uniform NW. Ni/NiO NWs may behave like core shell systems depending on the NW diameter and oxide thickness, introducing larger errors into the estimated modulus and strength. Similar scatter was observed for the yield strength, figure 7 (b) upper panel. There

have been few reports on the direct measurement of the mechanical properties of NiNWs, however, Peng *et al*[43] and Uchic *et al*[44] have found the strength of single crystalline NiNWs and Ni-pillars to be on the order of 1 – 3 *GPa* for diameters between 80 *nm* – 1.2 *μm*. The yield strength observed in this study was found to be as high as 8. 4 *GPa* for NWs with a 48 *nm* diameter, which may be a result of increased strength with reduction in lateral dimensions, given by the relation $\sigma \propto r^{-\alpha}$, analogous to the "Hall-Petch" relationship[45].

The electrical properties of NiNWs were characterised by the 4-point resistance method. However, NiNWs display an unusual physical phenomenon known as resistive switching (RS), meaning a number of electrical forming steps must be performed before the 4-point measurement possible. The RS mechanism is not pertinent in this report, however we will outline the RS process for clarity.

RS is a physical phenomenon where a dielectric suddenly changes its resistance upon the application of a strong electric field, the change in resistance being non-volatile and reversible. A filamentary switching mechanism has been shown to be the major switching process in metal oxide RS systems[46]. This mechanism involves the formation and rupture of conductive filaments (CF) across the insulator in a metal-insulator-metal (MIM) structure; in our case NiNW core-NiO-Ag top contact that comprises each of the four contacts in our experiments. The CF formation and rupture are responsible for the massive change in resistance observed[47], and shown in our case in figure 8 (b, c). The CF is formed by applying a potential between contacts 1&2 and 3&4, see figure 8 (a), i.e. across the NiO layer (the oxide surrounding the NW), between the Ni core and a contacting Ag electrode. Nickel interstitials are created by the dissociation of NiO under electric field, induced by the high potential. It is likely that this only occurs in localised areas where the oxide interface is thinnest. When the potential is high enough the Ni interstitials agglomerate and form a CF between the NiNW core and the Ag electrode, known as the FORM process[47-49], resulting in the formation of an ohmic contact.

Figure 8 (a-c) outlines the CF forming process. Figure 8 (a) shows a schematic of the NW contacted with four blue electrodes labelled 1-4. Firstly, the area designated as "FORM 1" was made conductively active across electrodes 1 and 2 by the forming process, given by the IV curve in figure 8 (b). Between 0 – 2.8 *V* the NW was in the

high-resistance state as there were no CFs at the NW/contact-1 or NW/contact-2 junctions. At a threshold voltage of 2.8 V the resistance has an abrupt decrease to the low resistance state. Here, the current is limited by a set compliance current of 500 nA. The NW remained in the low resistance state, signifying that a non-volatile CF had formed. The same procedure was applied to the "FORM 2" section between electrodes 3 and 4, given by the IV curve in figure 8 (c). We see the same characteristics as figure 8 (b) but with a higher compliance current of 10 μA. The higher compliance current was necessary for the NW to remain in the high resistance state at 0 V, more than likely due to a slightly thicker oxide at one, or both, electrodes 3 and 4. After the forming process standard 4-point electrical characterisation could be performed, given by the 2- and 4-point IV curve shown in figure 8 (d). The voltage was sourced and the current was measured across the outer electrodes 1 and 4, the voltage was measured across the inner electrodes 2 and 3. The IV curve displays typical linear behaviour observed in metals, showing that the forming process produces secure metallic filaments between the Ag electrode and NiNW core. Typically the 4-point resistance was found to be between 60 – 200 Ω, depending on the dimensions of the NW, with resistivities between 70 – 190 $n\Omega\, m$ comparable with the bulk value (69 $n\Omega\, m$).

Combining the electrical and mechanical measurements allows us to measure the electromechanical properties of individual NWs. In the next section we discuss the results on the $\Delta z/L$ dependent resistance, Poisson's ratio and gauge factor of individual AgNWs, comparing the result with the same measurement on NiNWs, crystalline and polycrystalline systems respectively.

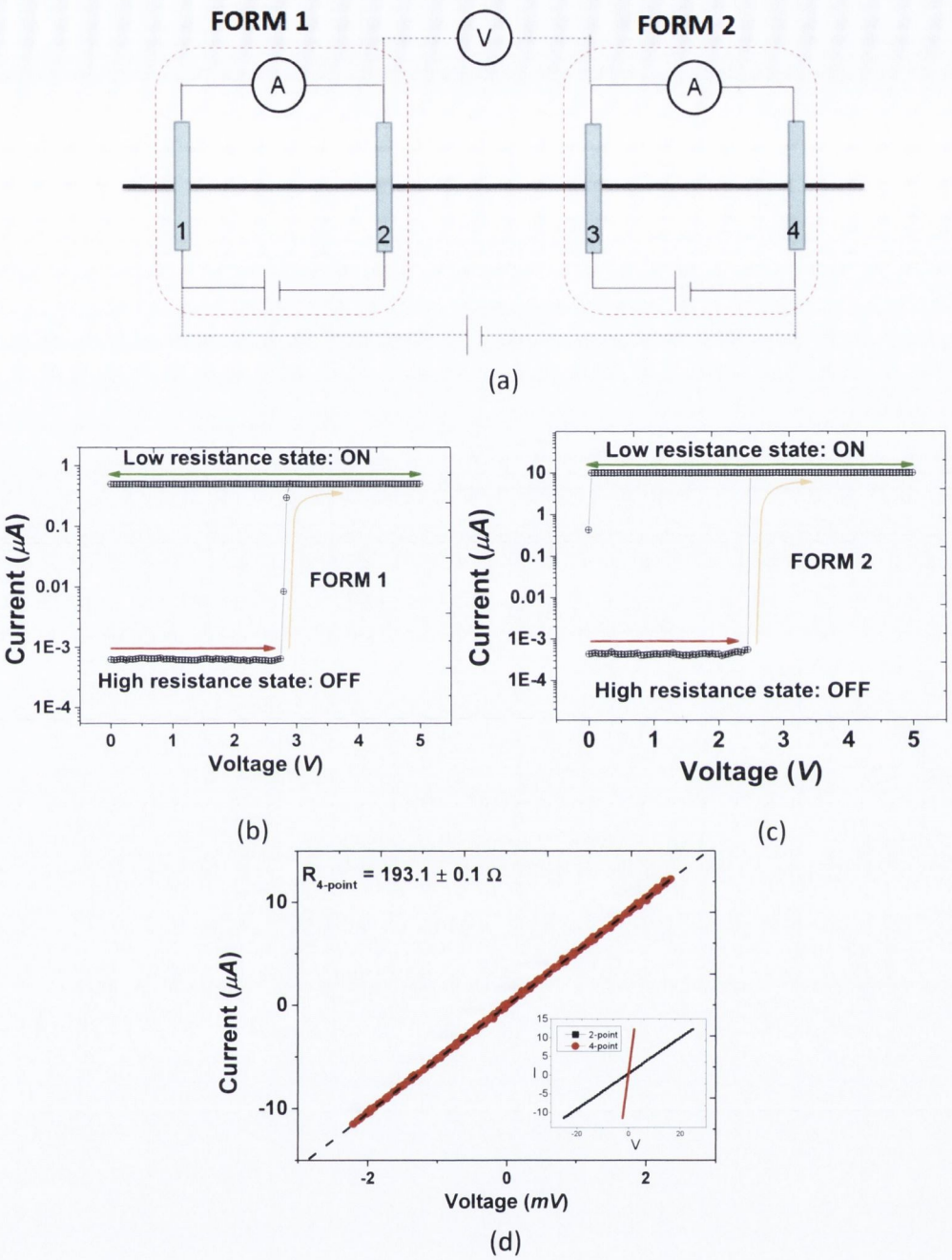

Figure 8: (a) Schematic of an individual nanowire contacted with four blue contacts. The NW is first formed across electrodes 1 and 2 (FORM 1), then across electrodes 3 and 4 (FORM 2). The 4-point measurement was then performed by sourcing the voltage and measuring the current the outer electrodes 1 and 4, and measuring the voltage was measured across the inner electrodes 2 and 3. (b, c) IV curves for the FORM 1 and FORM 2 steps respectively, showing the characteristic change from the high resistance to low resistance state in an RS system (d) 4-point IV curve for an individual NiNW. Inset is the 2- and 4-point curves

4.3.3 Strain dependent resistance, Poisson's ratio and Gauge factor for AgNW and NiNW

The following measurements were performed using the electromechanical technique described extensively in chapter 2. The relative resistance change, ΔR/R, as function of $\Delta z/L$ (Δz is the NW displacement from its normal axis and L is the length) was studied for NiNWs and AgNWs of diameters between 50 – 90 nm. Figure 9 shows a typical set of electromechanical experimental data. The F-d curve for each NW was recorded simultaneously with the 4-point measured current (I_m) and measured voltage (V_m). Figure 9 (a) shows a typical force curve, I_m and V_m curve as a function of displacement for an individual pentagonal AgNW of radius 32 *nm* with a $V_s = 25\ mV$ source voltage. The NW was elastically loaded and unloaded, shown by the F-d curve in the lower panel of figure 9 (a). The F-d curve is non-linear and symmetric about the dashed line indicating full elastic recovery after loading. The Young's modulus, E, given by the red line fit to equation 1 yields 95 ± 12 GPa, greater than the bulk modulus for silver (83 *GPa*), but within the range of previously reported values for pentagonal AgNWs[33].

The expected force dependence on displacement is evident, with no plastic deformation. This is evident from the definite and sharp change in force as the AFM tip reverses direction from the loading to the unloading cycle. During loading I_m (Figure 9 (a) middle panel) decreases by ~1% to a minimum at the point of maximum load, and then recovers to the previous unloaded value. Conversely, V_m increases by ~0. 9% during loading (figure 9 (a) upper panel) to a maximum corresponding to the maximum load. I_m and V_m completely recover to the unloaded value. We note no increase in resistance is observed without loading, i.e. any current-induced heating of the NW had no measurable effect on its resistivity and the original resistance was always recovered after unloading. Figure 10 (a, b) shows change in resistance at varying values of V_s as a function of time for 39 *nm* and 32 *nm* radii AgNWs. It is clear there was no change in resistance over time or as a function of V_s. Hence, any observed change in resistance was a direct property of the NW under investigation. Figure 9 (b), upper panel, shows the change in resistance as a function of displacement. R increases by ~0.9% at the maximum load.

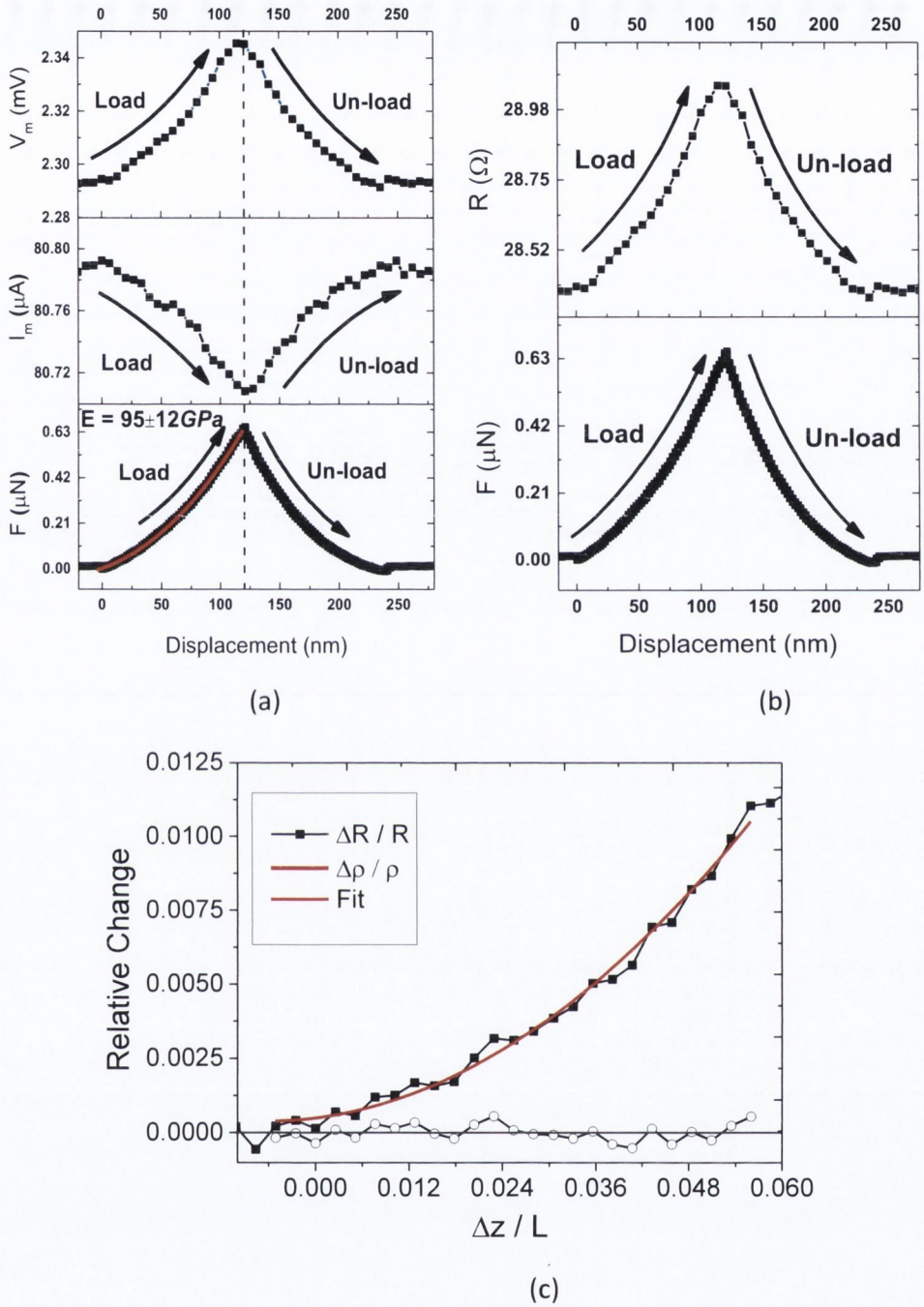

Figure 9: (a) Force, F, measured current, I_m, and measured voltage, V_m as a function of displacement for an individual 37 nm pentagonal AgNW, (b) the resistance, R, as a function of displacement. R is calculated by Ohm's law, V=IR. (c) The relative change in resistance and resistivity as a function of $\Delta z/L$ *($\Delta z/L$ was calculated by the displacement divided by the clamped nanowire length) for an individual 37 nm Ag NW.*

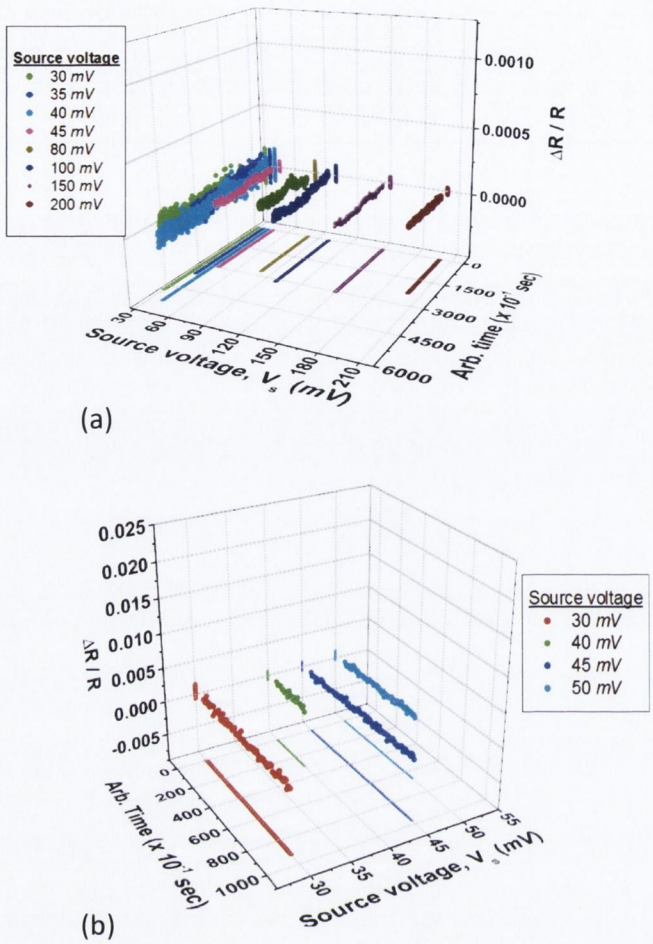

Figure 10: (a) The relative change in resistance as a function of time and source voltage for a 39 nm radius AgNW and a 32 nm radius NW (b). There was no observed change in the resistance as a function of time or source voltage.

The relative change in resistance, $\Delta R/R$, as a function of $\Delta z/L$, was analysed in terms of a new model that accounts for bending and tensile deformations. The $\Delta R/R$ term was experimentally derived from the resistance change divided by the initial resistance prior to mechanical manipulation. The $\Delta z/L$ term is given by the nanowire displacement, Δz_{center}, divided by the length, L, of the clamped nanowire. Our model predicts;

$$\frac{\Delta\rho}{\rho} = \frac{\Delta R}{R} - 2(1+2\nu)\left(\frac{\Delta z_{centre}}{L}\right)^2 \qquad (2)$$

where ρ is resistivity and ν is Poisson's ratio, the full derivation is provided in the appendix. Figure 9 (c) shows measured values as ΔR/R as a function of $\Delta z/L$ for a 37 *nm* radius NW and the quadratic dependence (filled squares) with $\Delta z/L$ predicted by equation 2 is clearly seen. Δρ/ρ is essentially the residual following the fit of ΔR/R

to the quadratic term in equation 2 and is shown as the black circles in figure 9 (c). As expected for a metal NW, ρ does not change with increasing $\Delta z/L$ so that the observed resistance change is fully accounted for by the increased NW length and the reduction in cross-section during loading. The ratio of the longitudinal to lateral strain is the Poisson's ratio v, and this method therefore provides a means to estimate the Poisson's ratio in addition to the gauge factor (GF) for an individual nanomaterial. GF is defined as the relative change in resistance as a function of strain, equation 3;

$$GF = \frac{\Delta R}{R} \Big/ \varepsilon = 1 + 2v \tag{3}$$

On further inspection, equation 2 can be derived in terms of the true strain, ε, where $\varepsilon = \Delta L/L = 2(\Delta z/L)^2$. Hence, the GF is given by $1+2v$, showing that the Poisson's ratio and the gauge factor are directly related.

To test the robustness of our approach and the ability of equation 2 to recover the Poisson's ratio, we characterised bulk cylindrical metal wires (phosphor bronze, copper and silver) 0.125-0.05 *mm* in diameter using a macroscopic version of the 3-point bending geometry, a photograph of the apparatus is shown in figure 11 (a). A typical curve for the relative change in resistance as a function of $\Delta z/L$ for each of the bulk wires tested using our macro method is shown in figure 11 (b-d). We found the value of Poisson's ratio to be 0.34 ± 0.12 for phosphor bronze (bulk = 0. 33), 0.36 ± 0.15 for copper (bulk = 0. 355), and 0.38 ± 0.19 for silver (bulk = 0. 37). In all instances the experimental values for Poisson's ratio agree closely with the corresponding bulk value, which validates both the experimental approach and the model used herein.

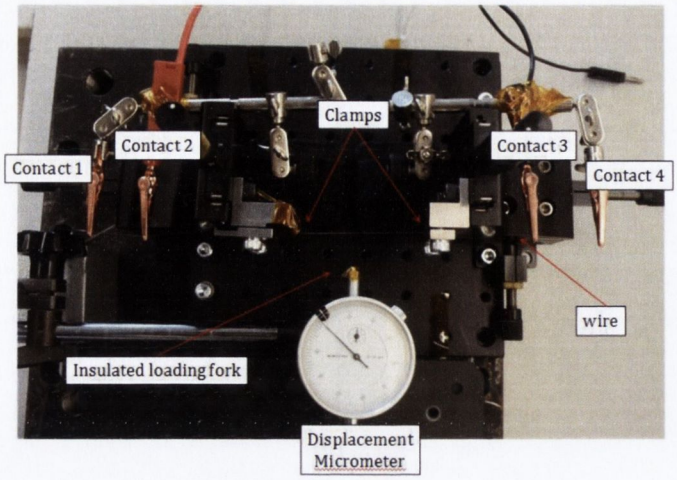

(a)

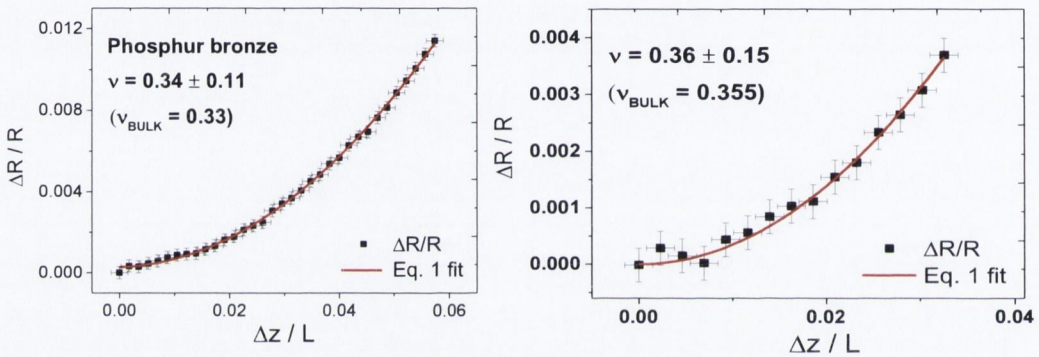

(b) (c)

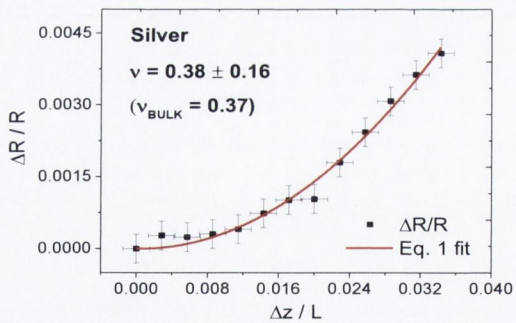

(d)

Figure 11: (a) Photograph of the bulk wire 3-point bending and 4-point electrical apparatus. The wire is mechanically clamped and then loaded using a calibrated micrometer. Electrical contact is achieved via four crocodile clips. (b) The relative change in resistance as a function of Δz/L for an individual 125 μm diameter phosphor bronze wire. The fit to Eq 2 is given by the red curve showing the model can be applied from macro to nanoscale materials. (c) The relative change in resistance as a function of Δz/L for an individual 100 μm diameter Cu wire. The fit to Eq 2 is given by the red curve. (d) The relative change in resistance as a function of Δz/L for an individual 50 μm diameter Ag wire. The fit to Eq 2 is given by the red curve.

Several AgNWs were analysed using our AFM based approach and figure 12 (a) shows GF vs. nanowire radius for all of the AgNW nanowires tested. We find GF to range between 1.17 – 2.19 for individual pentagonal Ag NWs between 26-42 *nm* in radius, equivalent to that of conventional metal strain gauges[50] (conventional metal strain gauges show GF's of 2). Figure 12 (a) shows that the GF displayed little dependence on the NW radius. The GF was found to increase slightly with reducing nanowire lateral dimensions, although a definite trend was not observed. The Poisson's ratio can be estimated by evaluating the quadratic coefficient $2(1+2\nu)$ in equation 2. Figure 12 (b) shows the estimated value for ν across all the AgNW specimens measured. The bulk value of ν for Ag[51] is 0.37, denoted by the dashed line in figure 12 (b).

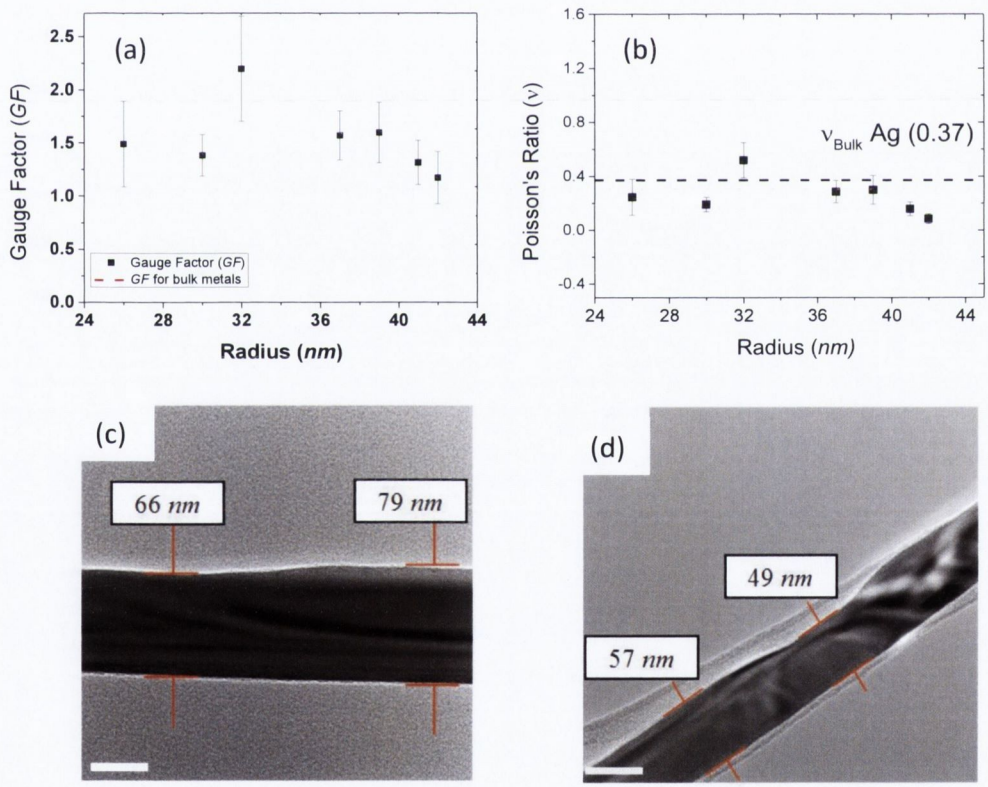

Figure 12: (a) The GF as a function of NW radius for each pentagonal Ag NW tested (26-42 nm radius). (b) Poisson's ratio, v, for NW of various radii (26-42 nm radius), the dashed line depicting the bulk value for Ag (0.37). (c, d) TEM images of Ag NW's showing the change in radius along their length. Such structural differences account for the large scatter in mechanical, electrical and electromechanical data. The scale bar in (b, c) is 40 nm.

From figure 12 (b) AgNWs displays large variations in ν both from the bulk value and among different wires. To probe the origin of the wide spread we performed identical measurements on NiNWs.

Figure 13 (a) shows an AFM image of an individual suspended NiNW contacted with four silver electrodes. The measurement procedure and sample arrangement is identical to those performed on AgNWs. The relative change in resistance as a function of $\Delta z/L$ on an individual 40 *nm* radius NiNW is shown in figure 13 (b). The measured values of ΔR/R, given by the filled symbols in figure 13 (b), displays the expected quadratic dependence with $\Delta z/L$ predicted by equation 2; similar to the curve observed for the same measurement on AgNWs. The values of $\Delta\rho/\rho$, given by the hollow circular symbols, showed no dependence on $\Delta z/L$, again similar to the behaviour observed for AgNWs. In figure 13 (b) the red curve is a fit of equation 2 to the filled symbols. The estimated values of Poisson's ratio for a range of NiNWs, calculated from fitting equation 2 to the data, is shown in figure 13 (C). We found that the estimated values of Poisson's ratio for NiNWs was between 0.3 – 0.33. A value for the *GF*, shown in figure 13 (d), of individual NiNWs, given by 1+2ν, was found to be ~1.60 ± 0.12, comparable with that measured for AgNWs.

Interestingly, the value of Poisson's ratio for individual NiNWs closely reflects the bulk value (the value for the bulk Poisson's ratio for nickel[52] is 0.31). We saw in figure 5 (b) that the NiNWs had a polycrystalline crystallographic structure throughout the NWs length and width; hence, the contribution to Poisson's ratio is spread over multiple crystallographic directions, mimicking the bulk material. This bulk like behaviour was reflected in the estimated values of Poisson's ratio measured for all of the individual NiNWs tested. In contrast the AgNWs studied were highly ordered single crystals along their length, displaying five-fold pentagonal twinning, figures 3 and 4. Large variations in the values for Poisson's ratio were observed between AgNWs with similar dimensions as seen in figure 12 (a).

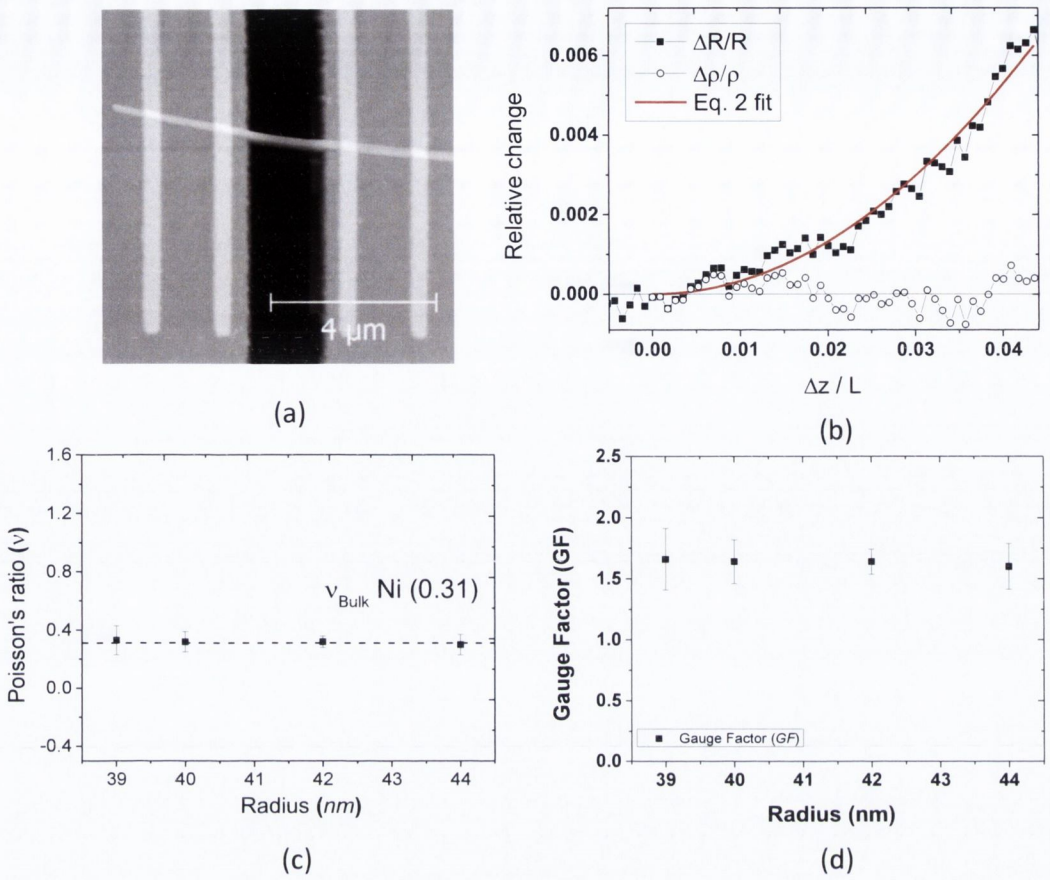

Figure 13: (a) AFM image of an individual 44 nm radius NiNW contacted with four Ag electrodes. (b) The relative change in resistance and resistivity as a function of Δz/L for the 44 nm NiNW, the red curve is a fit of the equation 2 to the filled symbols. Values of Poisson's ratio and the gauge factor were extrapolated from the fit. (c) Poisson's ratio, v, for NiNWs of various radii (39-44 nm radius), the black dashed line depicting the bulk value of v for Ni (0.31). (d) GF for for each NiNW tested, given by 1+2v.

To further probe the origin of the variations in the data presented in figure 12 (a, b), we measured Poisson's ratio and *GF* for two individual 32 *nm* and 39 *nm* radius pentagonal Ag NWs under repeated loading conditions and as a function of current density. Figure 13 shows the experimental data and measured values of *v* and *GF* for two individual Ag NWs under increasing current loads. Figure 14 (a) shows ΔR/R vs. Δz/L at four different current density levels for the 32 *nm* pentagonal Ag NW. As expected, the four curves fall on top of each other demonstrating that the resistance change is independent of current density, consistent with a highly metallic NW. The red curve is a fit of equation 2 and yields an averaged value for Poisson's ratio of 0.54 ± 0.14. Figure 14 (b) shows both Poisson's ratio and the gauge factor, calculated using equations 2 and 3 respectively, for each of the individual loading and current

density experiments. There is no significant dependence on current density. The *GF* was found to be 2.19 ± 0.21, with little scatter observed. Both Poisson's ratio and GF are independent of the current loading, as expected. Figure 14 (c) shows ΔR/R vs. Δz/L for current density between 16 - 105 A/m^2 for the 39 *nm* pentagonal Ag NW. The fit of equation 3 to the data yields a Poisson's ratio of 0.29 ± 0.13, consistent with the limited scatter in figure 14 (d).

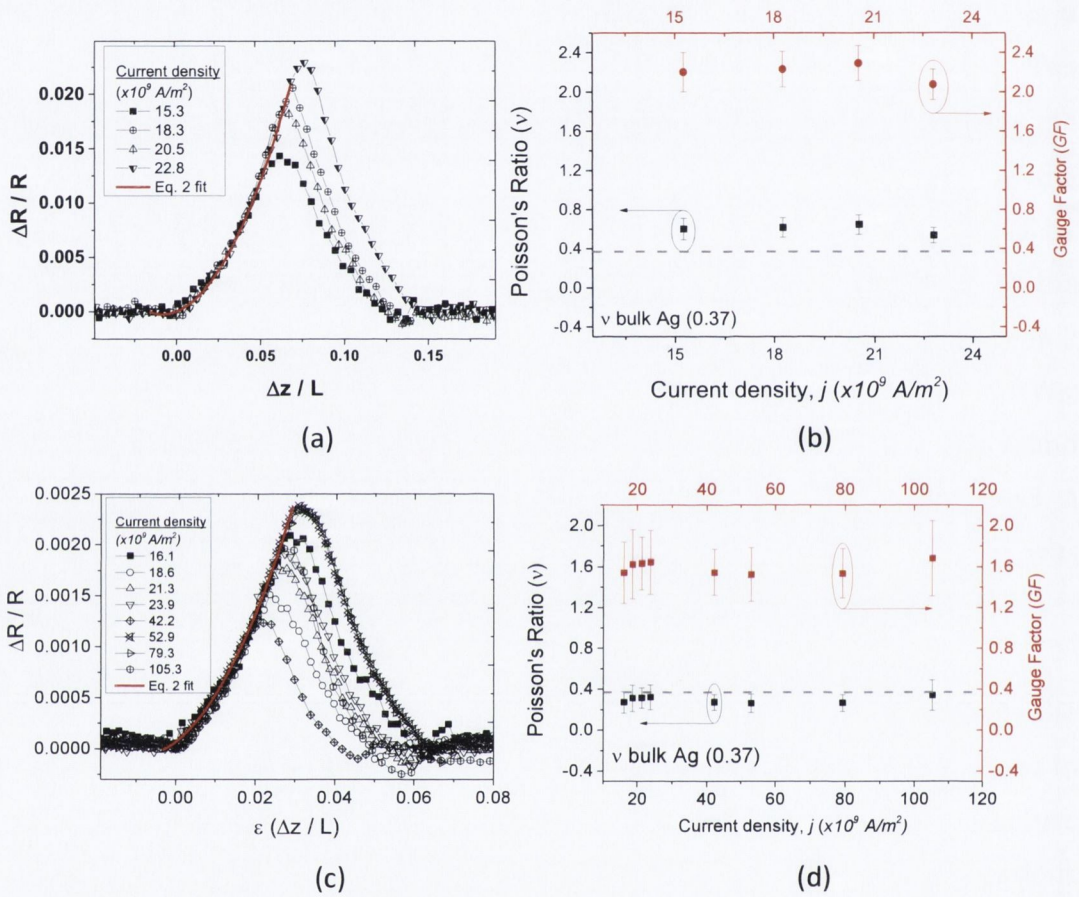

***Figure 14**: (a) The change in resistance as a function of Δz/L for an individual 32 nm radius Ag NW (E = 133±12 GPa) under increasing current loads. (b) Values of Poisson's ratio, v, and GF at increasing current density for the 32 nm radius Ag NW referred to in (a), calculated from equations 2 and 3 respectively. The black dashed line represents v for bulk silver (0.37), (c) The change in resistance as a function of Δz/L for an individual 39 nm radius Ag NW (E = 102±9 GPa) under increasing current loads, calculated from equations 3 and 4 respectively, and, (d) Values of Poisson's ratio, v, and GF at increasing current density referred to in (c). Again the black dashed line represents v for bulk silver (0.37).*

The *GF* for the 39 *nm* diameter Ag NW was found to be 1.59 ± 0.31. Both Poisson's ratio and *GF* are significantly different for the two Ag NWs despite the similarity in radius (32 *nm* and 39 *nm*). However, repeated experimental measurement on individual AgNWs reproducibly shows similar values for both Poisson's ratio and *GF.* Therefore, the scatter in the data shown in figures 12 (a, b) is not an artefact of the experimental method, but rather a fundamental property of individual Ag NW, supported by our TEM analysis, figure 12 (c, d). The Young's modulus, *E*, of the 32 *nm* and 39 *nm* Ag NWs examined were 133 ± 12 *GPa* and 102 ± 9 *GPa* respectively The Young's modulus and Poisson's ratio are related by the shear modulus, *G*, where $G = E/2(1+\nu)$, giving values for *G* of 41 ± 11 *GPa* and 39 ± 11 *GPa* for a 32 *nm* and 39 *nm* Ag NW respectively, the shear modulus for bulk silver being 30 *GPa*.

We found the value of ν to vary between 0.09 – 0.54 for individual Ag NWs, showing no obvious dependence on the NW radius. For isotropic materials the value of Poisson's ratio is strictly bound between -1 and 0.5. However, for anisotropic materials there are no such bounds. Poisson's ratio for crystalline solids can vary widely depending along which axis is being strained[53]. For example, in a body centred cubic (BCC) structure, strain along the (110) direction with a dimension change in the $(1\bar{1}0)$ can yield ν approaching -1, but the dimension change along the (001) direction can yield a value for ν approaching 2. Pentagonally twinned Ag NW are single crystalline, with the [011] axis along their length[33]. Also, the NWs have a FCC structure, common in metals. Here, the AFM tip strains the NW along the long axis, as the wire lays perpendicular across the trench. This corresponds to the (011) axis. The axis of dimension change is then $(0\bar{1}1)$. Baughman *et al*[54] reported that the change in ν for an FCC structure in the $(0\bar{1}1)$ direction, with a (011) strain, is zero. Although this is not consistent with our results, it is also important to realise that the NWs are not perfect i.e. from wire to wire the crystal structure, orientation and defect concentration can vary considerably, as well as dimensional changes along the wires length, figure 11 (c, d). These types of material imperfections may have a huge effect on the measured Poisson's ratio and indeed the mechanical properties, as has been seen before[55].

4.4. Conclusion

In conclusion the dependence of resistance and resistivity on $\Delta z/L$ was shown for pentagonal AgNWs between 50 – 90 *nm* in diameter, comparing characteristics with the same measurement on NiNWs. We have developed a generalised model to describe the relationship between the changes in resistance and resistivity for an elastic nanowire under strain. We found that individual AgNW resistance increases with $\Delta z/L$, by up to 2.3% at 1.1% strain. The GF for individual Ag NW was found to be between 1.17 – 2.19, comparable to that of bulk metals, and with the value of GF found for NiNWs (1.60-1.64), displaying no obvious dependence on nanowire dimensions. A novel electromechanical method for measuring the Poisson's ratio of nanoentities has been established. Using this method we found the Poisson's ratio for AgNWs to lie between 0.05 – 0.54, displaying large deviations from the bulk value. The value of Poisson's ratio for two NiNWs was found to be comparable to the bulk value. The values for Poisson's ratio and gauge factor were found to be independent of current density. We have shown the values for Poisson's ratio and the *GF* are reproducible under repeated interrogation on individual Ag NWs, showing the robustness of the method. Moreover, we have displayed the importance of measuring the full range of mechanical properties of each nanowire, as properties such as Poisson's ratio are generally assumed that of the bulk value and we have shown that single crystal nanowires can deviate substantially from the bulk value. AgNWs are of importance due to their potential applications as electrical interconnects, in NEMS devices and as transparent flexible electronics. These results are of critical importance in understanding how individual NWs behave under strain and provide an in-depth method to measure electromechanical properties.

4.5. References

1. Bin Wu, A.H., John J. Boland, *Mechanical properties of ultrahigh strength gold nanowires.* Nature Materials, 2005. **4**(525-529).
2. Espinosa, H.D., R.A. Bernal, and M. Minary-Jolandan, *A Review of Mechanical and Electromechanical Properties of Piezoelectric Nanowires.* Advanced Materials, 2012. **24**(34): p. 4656-4675.
3. Schinwald, A., Chernova, T., Donaldson, K., *Use of silver nanowires to determine thresholds for fibre length-dependent pulmonary inflammation and inhibition of macrophage migration in vitro.* Particle and Fibre Toxicology, 2012. **9**(47).

4. Xu, F. and Y. Zhu, *Highly Conductive and Stretchable Silver Nanowire Conductors.* Advanced Materials, 2012. **24**(37): p. 5117-5122.
5. Lee, M.-S., et al., *High-Performance, Transparent, and Stretchable Electrodes Using Graphene–Metal Nanowire Hybrid Structures.* Nano Letters, 2013. **13**(6): p. 2814-2821.
6. Akter, T. and W.S. Kim, *Reversibly Stretchable Transparent Conductive Coatings of Spray-Deposited Silver Nanowires.* ACS Applied Materials & Interfaces, 2012. **4**(4): p. 1855-1859.
7. http://www.itrs.net/links/2009ITRS/Home2009.htm, 2009.
8. Dadgour, H.F. and K. Banerjee, *Hybrid NEMS-CMOS integrated circuits: A novel strategy for energy-efficient designs.* Computers & Digital Techniques, IET, 2009. **3**(6): p. 593-608.
9. Loh O. Y., E.H.D., *Nanoelectromechanical contact switches.* Nature Nanotechnology, 2012. **7**(5): p. 283-295.
10. Ward, J.W., et al. *A nonvolatile nanoelectromechanical memory element utilizing a fabric of carbon nanotubes*. in *Non-Volatile Memory Technology Symposium, 2004*. 2004.
11. Loh, O., et al., *Carbon-Carbon Contacts for Robust Nanoelectromechanical Switches.* Advanced Materials, 2012. **24**(18): p. 2463-2468.
12. Axelsson, S., et al., *Theoretical and experimental investigations of three-terminal carbon nanotube relays.* New Journal of Physics, 2005. **7**(1): p. 245.
13. Cha, S.N., et al., *Fabrication of a nanoelectromechanical switch using a suspended carbon nanotube.* Applied Physics Letters, 2005. **86**(8): p. 083105-3.
14. Qiliang, L., et al., *Silicon nanowire electromechanical switches for logic device application.* Nanotechnology, 2007. **18**(31): p. 315202.
15. Dadgour, H.F., et al. *Design and analysis of compact ultra Energy-Efficient logic gates using laterally-actuated double-electrode NEMS*. in *Design Automation Conference (DAC), 2010 47th ACM/IEEE*. 2010.
16. Espinosa, H.D., R.A. Bernal, and T. Filleter, *In Situ TEM Electromechanical Testing of Nanowires and Nanotubes.* Small, 2012. **8**(21): p. 3233-3252.
17. He, R. and P. Yang, *Giant piezoresistance effect in silicon nanowires.* Nat Nano, 2006. **1**(1): p. 42-46.
18. Yong-Jae Kim, K.S., In-Chul Choi, In-Suk Choi, Won il Park, Jae-il Jang, *Exploring Nanomechanical Behavior of Silicon Nanowires: AFM Bending Versus Nanoindentation.* Advanced Functional Materials 2011. **21**: p. 279-286.
19. Hongjiang, Z., et al., *In situ SEM electromechanical characterization of nanowire using an electrostatic tensile device.* Journal of Physics D: Applied Physics, 2013. **46**(30): p. 305501.
20. Espinosa, H.D., Bernal R. A., *Microelectromechanical Device and System.* WO 2011/053346 A1, 2011.
21. Xin, X., et al., *An improved AFM cross-sectional method for piezoelectric nanostructures properties investigation: application to GaN nanowires.* Nanotechnology, 2011. **22**(10): p. 105704.
22. Wang, Z.L. and J. Song, *Piezoelectric Nanogenerators Based on Zinc Oxide Nanowire Arrays.* Science, 2006. **312**(5771): p. 242-246.
23. http://www.seashelltech.com/.
24. Wang. Y., D.J.C., *Methods for the production of silver nanowires.* 12/2011 US 7,922,787 B2, 2011.

25. Wiley, B., et al., *Shape-Controlled Synthesis of Metal Nanostructures: The Case of Silver.* Chemistry – A European Journal, 2005. **11**(2): p. 454-463.
26. Wiley, B., et al., *Polyol Synthesis of Silver Nanoparticles: Use of Chloride and Oxygen to Promote the Formation of Single-Crystal, Truncated Cubes and Tetrahedrons.* Nano Letters, 2004. **4**(9): p. 1733-1739.
27. Ducamp-Sanguesa, C., R. Herrera-Urbina, and M. Figlarz, *Synthesis and characterization of fine and monodisperse silver particles of uniform shape.* Journal of Solid State Chemistry, 1992. **100**(2): p. 272-280.
28. Sun, Y., et al., *Polyol Synthesis of Uniform Silver Nanowires: A Plausible Growth Mechanism and the Supporting Evidence.* Nano Letters, 2003. **3**(7): p. 955-960.
29. Sun, X.M. and Y.D. Li, *Cylindrical Silver Nanowires: Preparation, Structure, and Optical Properties.* Advanced Materials, 2005. **17**(21): p. 2626-2630.
30. Kolesnik, M.M., et al., *Resolving In Situ Specific-Contact, Current-Crowding, and Channel Resistivity in Nanowire Devices: A Case Study with Silver Nanowires.* Small, 2011. **7**(20): p. 2873-2877.
31. http://www.nanomaterials.it/.
32. Heidelberg, A., et al., *A Generalized Description of the Elastic Properties of Nanowires.* Nano Letters, 2006. **6**(6): p. 1101-1106.
33. Bin Wu, A.H., John J. Boland, John E. Sader, XiaoMing Sun, YaDong Li, *Microstructure-Hardened Silver nanowires.* Nanoletters, 2006. **6**(3): p. 468-472.
34. Jing, G.Y., et al., *Surface effects on elastic properties of silver nanowires: Contact atomic-force microscopy.* Physical Review B, 2006. **73**(23): p. 235409.
35. Li, X., et al., *Nanoindentation of Silver Nanowires.* Nano Letters, 2003. **3**(11): p. 1495-1498.
36. Kuhn, K.J., *Considerations for Ultimate CMOS Scaling.* Electron Devices, IEEE Transactions on, 2012. **59**(7): p. 1813-1828.
37. Celik, E. and et al., *Mechanical characterization of nickel nanowires by using a customized atomic force microscope.* Nanotechnology, 2011. **22**(15): p. 155702.
38. Majjad, H., et al., *Dynamic determination of Young's modulus of electroplated nickel used in LIGA technique.* Sensors and Actuators A: Physical, 1999. **74**(1–3): p. 148-151.
39. Namazu, T. and S. Inoue, *Characterization of single crystal silicon and electroplated nickel films by uniaxial tensile test with in situ X-ray diffraction measurement.* Fatigue & Fracture of Engineering Materials & Structures, 2007. **30**(1): p. 13-20.
40. Mazza, E., S. Abel, and J. Dual, *Experimental determination of mechanical properties of Ni and Ni-Fe microbars.* Microsystem Technologies, 1995. **2**(1): p. 197-202.
41. Ebrahimi, F., et al., *Mechanical properties of nanocrystalline nickel produced by electrodeposition.* Nanostructured Materials, 1999. **11**(3): p. 343-350.
42. Thompson, A. and H. Saxton, *Structure, strength, and fracture of electrodeposited nickel and Ni–Co alloys.* Metallurgical Transactions, 1973. **4**(6): p. 1599-1605.
43. Peng, C., et al., *Strain rate dependent mechanical properties in single crystal nickel nanowires.* Applied Physics Letters, 2013. **102**(8): p. -.
44. Uchic, M.D., et al., *Sample Dimensions Influence Strength and Crystal Plasticity.* Science, 2004. **305**(5686): p. 986-989.
45. Pande, C.S. and K.P. Cooper, *Nanomechanics of Hall–Petch relationship in nanocrystalline materials.* Progress in Materials Science, 2009. **54**(6): p. 689-706.

46. Kwon, D.-H., et al., *Atomic structure of conducting nanofilaments in TiO2 resistive switching memory.* Nat Nano, 2010. **5**(2): p. 148-153.
47. Park, G.-S., et al., *Observation of electric-field induced Ni filament channels in polycrystalline NiO[sub x] film.* Applied Physics Letters, 2007. **91**(22): p. 222103-3.
48. Kim, D.C., et al., *Electrical observations of filamentary conductions for the resistive memory switching in NiO films.* Applied Physics Letters, 2006. **88**(20): p. 202102-3.
49. Jung, K., et al., *Temperature dependence of high- and low-resistance bistable states in polycrystalline NiO films.* Applied Physics Letters, 2007. **90**(5): p. -.
50. Yamada, T., Hayamizu, Y., Yamamoto, Y., Yomogida, Y., Izadi-Najafabadi, A., Futaba, D. N., Hata, K., *A stretchable carbon nanotube strain sensor for human-motion detection.* Nature Nanotechnology, 2011. **6**(5): p. 296-301.
51. Wilson, J.S., *Sensor Technology Handbook.* Elsevier Inc., 2005: p. 621.
52. Frick, C.P., et al., *Size effect on strength and strain hardening of small-scale [111] nickel compression pillars.* Materials Science and Engineering: A, 2008. **489**(1–2): p. 319-329.
53. Ting, T.C.T. and T. Chen, *Poisson's ratio for anisotropic elastic materials can have no bounds.* The Quarterly Journal of Mechanics and Applied Mathematics, 2005. **58**(1): p. 73-82.
54. Baughman, R.H., et al., *Negative Poisson's ratios as a common feature of cubic metals.* Nature, 1998. **392**(6674): p. 362-365.
55. Wu, B., et al., *Microstructure-Hardened Silver Nanowires.* Nano Letters, 2006. **6**(3): p. 468-472.

Chapter 5: Current Induced Stiffening of Individual Silver Nanowires and Nickel Nanowires

5.1 Motivation

The dependence of a materials transport properties on strain has been a huge area of interest for the past 60 years or so, mainly due to applications in electronic devices. In the 1950s the influence of strain on the mobility of intrinsic silicon was first investigated[1, 2], and since the early 1990s researchers have introduced strain into silicon devices to enhance their performance[3, 4]. Even in silicon nanowires (Si NW), strain induced mobility enhancement has been demonstrated[5, 6]. However, the reciprocal effect has not been studied, i.e. whether charge flow can influence the mechanical properties of nano structures.

In 2009, Lasagne *et al*[7] studied the coupling between charge transport and mechanics in single-walled carbon nanotube (SWCNT) mechanical resonators at low temperatures. In this paper, the motion of an individual suspended SWCNT is voltage driven using an alternating voltage $[V_g^{AC}\cos(2\pi ft)]$ applied to the gate, generating an electrostatic force on the SWCNT. The induced motion was detected by a mixing signal across the source and the drain $[V_{SD}^{AC}\cos[2\pi(f+\delta f)t]]$. Figure 1 (a) shows the SWCNT differential conductance as a function of the source-drain voltage and constant gate voltage, V_g^{DC}. Figure 1 (b) shows the mixing current from the drain as a function of the driving frequency and V_g^{DC}. The frequency of the red lobes goes up and down when increasing V_g^{DC}, with the same period as the conductance in, figure 1 (a), showing that the mechanics and the charge transport in the device are correlated. Moreover, the frequency of the red lobes shifts continuously over the full range of V_g^{DC}. This is caused by mechanical tension in the beam as electrostatics bends the beam.

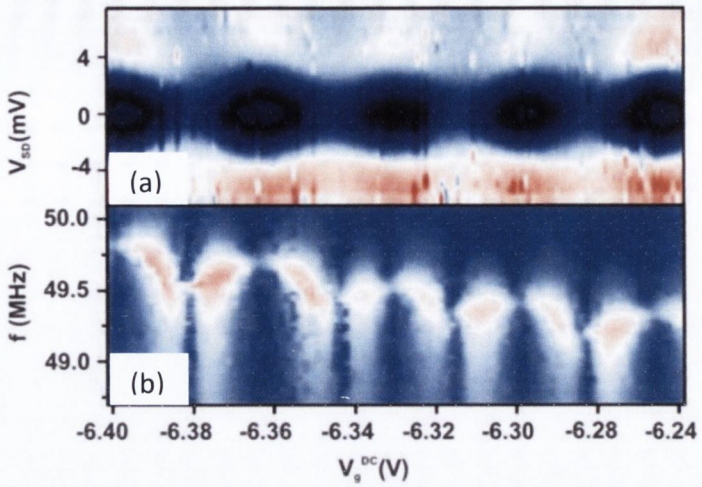

Figure 1: Electronic and mechanical properties of the SWCNT device at 4 K. (a) The differential conductance as a function of source-drain voltage and gate voltage. (b) Mixing current from the drain as a function of driving frequency and gate voltage [7]

The mechanical dependence on charge has also been demonstrated in graphene. In 2013, Hao *et al*[8] studied the effect of electric charge on the mechanical properties of graphene under tensile loading. The authors applied molecular dynamics methods to calculate the Young's modulus as a function of charge residing on the graphene's surface. It was found that the Young's moduli, for both armchair (figure 2 (a)) and zigzag (figure 2 (b)) graphene, decreased with the increase of electric potential and net electric charges on the graphene.

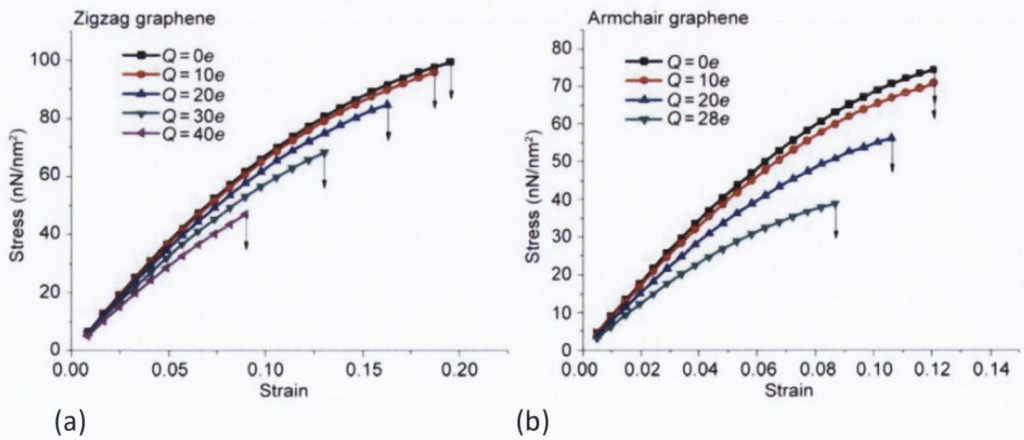

Figure 2: The relationship between tensile stress and longitudinal strain for zigzag, (a), and armchair, (b), graphene under increasing charge conditions [8]

The authors did not discuss the mechanism for the charge induced softening, but did refer to bond lengthening at the sheet edges resulting in decreased strength. This effect may also be the cause of the observed reduction in modulus.

In terms of metallic NW's little is known about the effect of charge transport on the mechanical properties, in particular the Young's modulus. An increased surface-to-bulk-atom ratio, charge trapping and nanoscale heating/cooling may cause interesting effects in NW mechanics as charge flows through a specimen. In chapter 3, the dynamic nature of NEMS devices was discussed in terms of characterising a materials electrical reaction under the influence of a mechanical load. Similarly, an understanding of the mechanical reaction under an electrical load is equally, if not more, important. We have seen that the mechanical response of CNTs and graphene can change in the presence of charge[7, 8]. In a NEMS device this type of reaction could bring benefits and drawbacks. For example, if the active element stiffens during charge flow, it may pull-off the drain electrode, switching the device off unexpectedly. However, if charge flow has the opposite effect, and relaxes the active element, it may automatically pull-off when the charge flow is relieved, creating a relatively low power device.

Silver nanowires (AgNW) have received much interest in biological applications and as flexible, transparent conductive electrodes[9-12]. Potential applications as interconnects have also been explored and Ag NW may prove useful as the active components in NEMS devices. In this chapter the dependence of Young's modulus, E, on the current density is investigated for individual, suspended silver nanowires and the results compared with the same measurement on nickel nanowires (NiNW).

5.2 Current Induced Stiffening in Silver Nanowires

5.2.1 The dependence of Young's modulus on current load: Repeatedly loading a Silver nanowire at its centre point under a single current load.

In the following sections the experimental approach was the same as that of chapter 4 and previously described in chapter 2. As a first approach an individual Ag NW was loaded at its centre point multiple times under two electrical loading conditions; (1) no current load and (2) steady state current load. In both cases the NW was

elastically loaded and released by a user controlled AFM tip. First the NW was mechanically loaded, and the f-d curve recorded, with no current passing through the wire. Secondly, using the electrical technique described in chapter 2, a voltage was sourced, V_s, across the NW inducing a measured current.

- The amount of current allowed to pass through the NW was calibrated by performing IV characterisation on an electrical probe station. From Ohm's law, $V=IR$, the current was voltage controlled by accurately measuring the resistance of the specimen prior to the electromechanical experiment.

Rather importantly, the specimen area was imaged between each mechanical interrogation to correct for any piezo drift in the AFM scanners, although only small amounts of drift on the order of 20 nm, was observed between experiments.

Figure 3 shows the results for repeated elastic centre loads on an individual 33 *nm* radius AgNW. Figure 3 (a) shows an AFM image of the individual AgNW suspended above a pre-defined trench, contacted with 4 silver electrodes. The trench is the dark region running the length of the image. The 4 contact silver electrodes run parallel either side of the trench, with the NW perpendicular to the trench. Importantly, the NW bridges over the trench and does not sag to any great degree, based on the AFM height image. For example, if the NW sagged into the trench, the area where the NW goes across the trench would be dark, as the dark sections signify a lower height. It is clear that the area of the NW moving across the trench is bright, equivalent to that of the surrounding substrate.

An example of the f-d curves for both conditions is shown in figure 3 (b). The red curve represents the f-d curve in the open state i. e. no current flow. The f-d curve with 32 μA flowing through the wire is represented by the black curve. In the case where there is no stiffness change both curves would overlap, but we observe a small discrepancy. Firstly, the black curve reaches a maximum force of ~300 nN similar to that of the red curve. However, the black curve reaches its maximum force at lower displacement than the red curve. This behaviour was observed as the AFM tip approaches and retracts during the loading cycle. Applying the generalised mechanical model for a double-clamped elastic NW;

$$F_{center} = \frac{192EI}{L^3} f(\alpha)\Delta z_{center} \quad (1)$$

discussed in chapter 2 and derived in the appendix, the Young's modulus was calculated. We found the NW's modulus increases by ~20 %, from 123 ± 9 *GPa* to 148 ± 11 *GPa*, on the application of 32 μA.

Figure 3 (c) shows the change in elastic modulus with current flow performed over multiple trials on the same NW, elastically loaded at its centre point. Here, the red data represents the open state, the black data representing a current flow of 34 μA passing through the NW. On each trial the modulus is found to increase by between 10 – 15 %, shown in figure 3 (d). The average increase in E is 13 %.

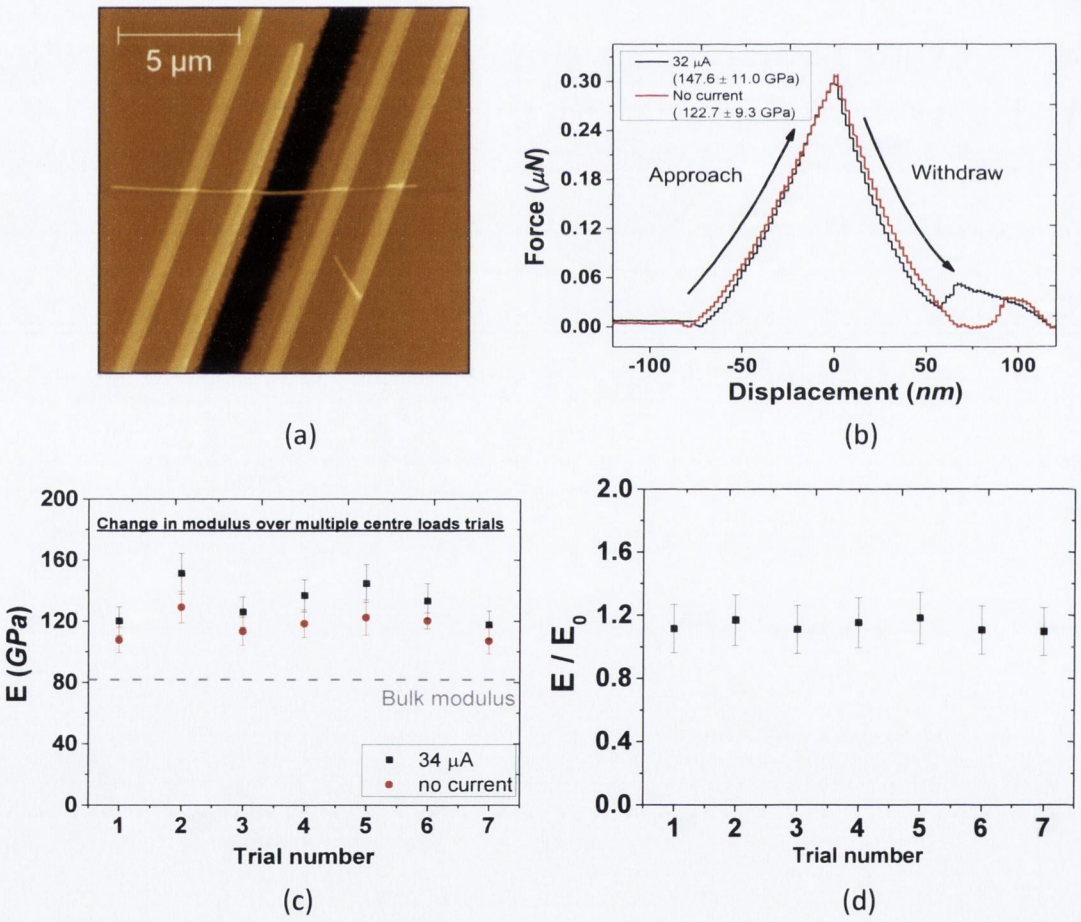

Figure 3: (a) AFM image of a AgNW, on a SiO_2 substrate, (b) f-d curves with current, black, and without current, red, (c) Young's modulus as a function of applied current over multiple centre loading trials and (d) The relative change in modulus with the application of current for each of the trials

To probe this phenomenon further we measured the Young's modulus dependence on increasing current density for several individual AgNWs, comparing the results to the same measurement performed on NiNWs. We saw in chapter 4 that NiNWs have a polycrystalline structure. In contrast, AgNWs are single crystal providing ideal comparative systems. In the next section we discuss the results.

5.2.2 The dependence of Young's modulus on increasing current density for individual AgNWs, comparing the result with NiNWs.

The experimental technique applied here is the same as that in the last section. However, the current density, j, is reported rather than current. The current density normalises the current with respect to cross sectional area, $j = I/A$. Hence, it allows us to directly compare NWs of different radii and electrical resistance under a universal parameter.

Figure 4 displays the results for an individual 34 *nm* radius AgNW elastically loaded under increased current densities. Figure 4 (a) shows the set of force-displacement curves under increased current density. It is clear from figure 4 (a) that the curvature of each f-d curve increases, and hence the stiffness increases, with each incremental increase in current density, j. Applying the generalised model, equation 1, to each f-d curve gives the elastic modulus, E. Figure 4 (b) shows the elastic modulus as a function of current density. A stark increase in modulus was observed, from $E = 93\ GPa$ at zero current density to $E = 218\ GPa$ at the highest current density. Figure 4 (c) shows the change in modulus, E/E_0, as a function of current density. E is the measured elastic modulus and E_0 is the elastic modulus at zero current density. Again, there is a clear trend as the modulus increases with the amount of charge that is passed through; hence, an increase in the current density acts to stiffen the NW.

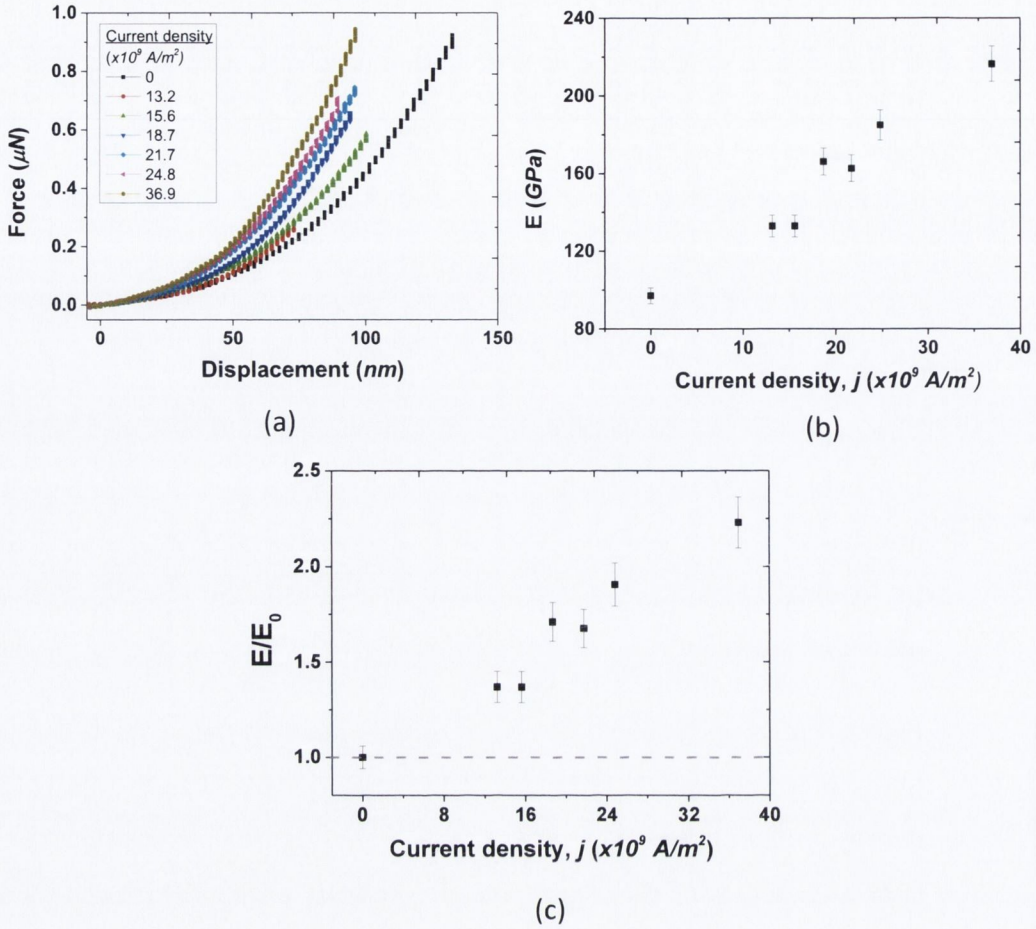

Figure 4: (a) Force-displacement curves as function of current density loading for an individual 34 nm radius AgNW, (b) the change in modulus as a function of voltage load. There was >x2 increase in the modulus observed and (c) the change in modulus as a function of current density showing clear stiffening behaviour with increased current density.

Several AgNWs between 32 - 39 *nm* in radius were analysed using this technique. Figure 5 shows the change in elastic modulus as a function of current density for each NW studied. A general trend towards current induced stiffening was observed across all the specimens examined. The scatter in the data makes it difficult to elucidate an exact analytical dependence for the modulus change as a function of increasing current density. From figure 5, it was found that a simple $y=Ax^2$ curve described the data approximately, where the constant A was found to be 1.4×10^{-3}; hence the equation $E/E_0 \approx 10^{-3} j^2$ approximately describes the relationship between the change in modulus and increasing current density, where the units of j are $\times 10^9$ A/m^2.

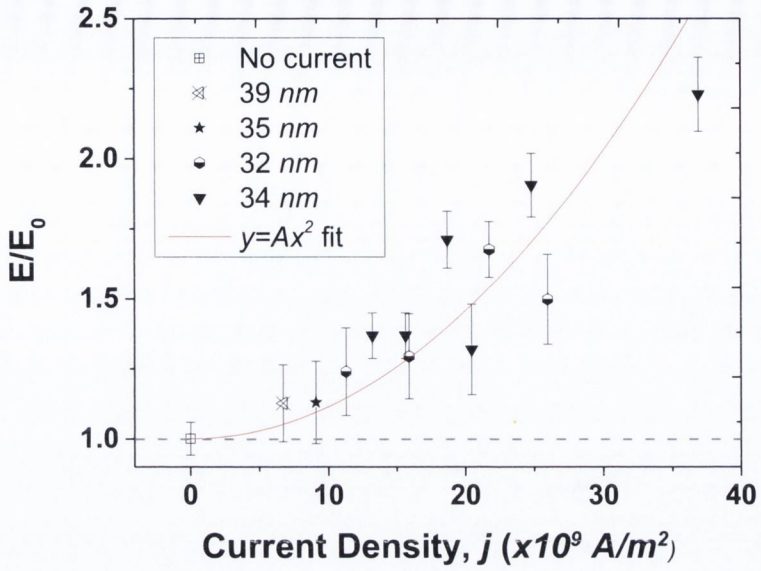

Figure 5: The change in modulus as a function of increasing current density for several individual AgNWs between 32 – 39 nm radius. A clear trend towards current induced stiffening was observed.

Figure 6 shows the current density dependent modulus of an individual 40 *nm* radius NiNW. There was no evident increase in modulus observed for NiNWs at current densities comparable to that of the identical measurement on AgNWs, shown in figure 5. As we discussed in chapter 4 the crystallographic structure of NiNWs is polycrystalline, whereas AgNWs are single crystals with five-fold twinning along their length.

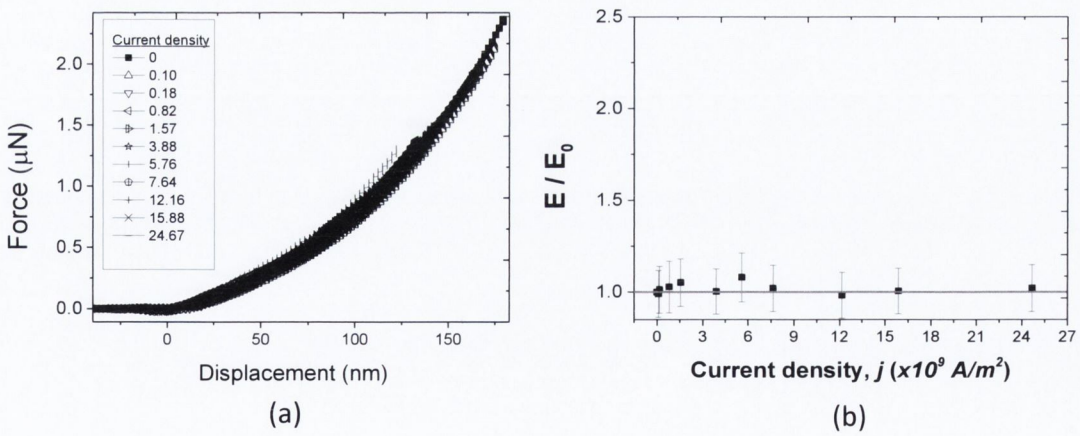

Figure 6: (a) Force-displacement curves as function of current density loading for an individual 40 nm radius NiNW, (b) the change in modulus as a function of increasing current density for an individual 40 nm radius NiNW. There was no observed change in modulus with increasing current density as we observed for AgNWs.

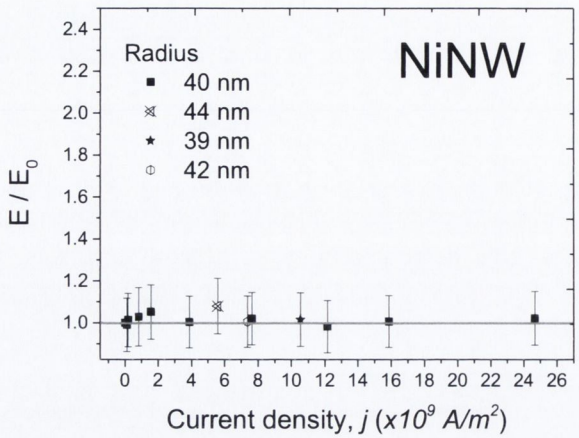

Figure 7: The change in Young's modulus as a function of current density for each NW tested.

Several NiNWs were tested using this method, shown in figure 7. There was no appreciable change in stiffness as a function of current density across all of the NiNWs tested, in contrast to the stiffening effect observed in AgNWs, shown in figure 5.

The results presented for both AgNWs and NiNWs are somewhat surprising. Firstly, the individual NWs could support large current densities, on the order of 10^9 A/m^2. The change in temperature with time, dT/dt, at such current densities is large according to some reports[13]. According to Fangohr *et al*[13] dT/dt can be estimated, assuming no losses, in terms of the specific heat capacity, C, current density, j, conductivity, σ and density, ρ_D [13];

$$\frac{dT}{dt} = \frac{j^2}{\rho C \sigma} \tag{2}$$

Using the material parameters for silver ($C = 230$ J/KgK, $j = 10^9$ A/m^2, $\sigma = 5.9 \times 10^7$ $(\Omega m)^{-1}$, $\rho_D = 10{,}490$ kg/m^3) the change in temperature with time is calculated;

$$\frac{dT}{dt} = \frac{j^2}{\rho C \sigma} = 7 \times 10^3 \, K/s$$

From this equation the temperature should increase by 7024 K/s, at 10^9 A/m^2 and even as much as 10^6 K/s at the maximum current density applied, see figure 4 (c). [Importantly, equation 2 does not account for thermal losses to the environment (the environment being the air surrounding the NW, the substrate beneath it and the metal contacts)]. The melting point of silver is 1235 K. By this estimation the

NW should melt in a fraction of a second. However, NW melting has never been observed. In fact, if we monitor the resistance of an individual NW with time, the resistance remains constant showing only slight local deviation due to noise, discussed in detail in chapter 4.

The opposite effect has also been reported, where current induces cooling rather than heating[14, 15]. Horsefield *et al*[15] studied the effect of power dissipation in nanoscale conductors. Using classical, semi-classical and quantum models the following relationship was predicted by each of the models;

$$w \approx 4j\left(\frac{m}{M}\right)\left(K_e - 2K_{atom}\right) \tag{3}$$

Where w is the electrical power, j is the current, m is the mass of the impingent electron, M is the mass of the atom, and K_e and K_{atom} are the kinetic energies of the electron and atom respectively. The power is composed of two competing terms. If the excess energy of the electrons, K_e, exceeds the average atomic kinetic energy, K_{atom}, (i. e. $K_e > K_{atom}$) the net power transferred to the atom is positive, leading to heating. But if $K_e < K_{atom}$ the net power transferred is negative, leading to cooling. Making several approximations, both kinetic energy terms can be calculated, shown in figure 8. The approximations made in the kinetic energy calculations were as follows; the average atomic velocity of silver was equal to the longitudinal sound velocity in bulk silver[16], the voltage potential experienced by each electron was equal, assuming the voltage across the wire was equal to the source voltage. We found the K_{atom} term to be two orders of magnitude greater than K_e, showing no overlap within the voltage limits used in this study. From this model only cooling events occur. Indeed, the modulus for bulk silver has been shown to increase linearly with decreasing temperature[17], although not to the extent observed here, which may be due to the nanoscale dimensions of the wire.

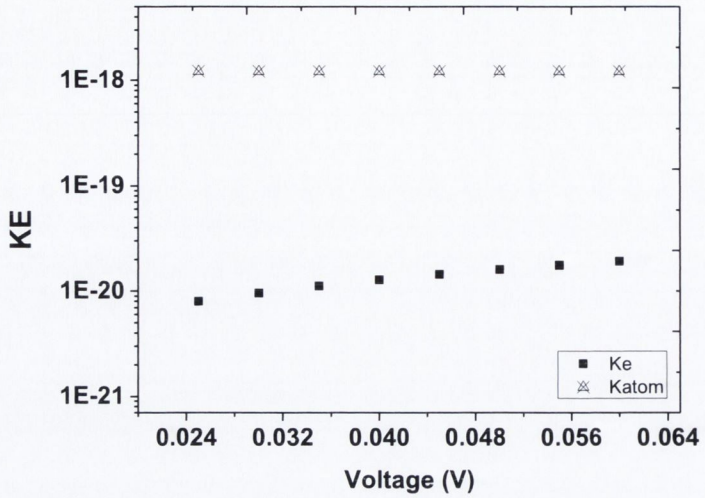

Figure 8: The Kinetic energy, KE, for both the atom and electron. The KE of the atom is two orders of magnitude greater than the KE of the electro, resulting in cooling effects dominating.

Further experimental measurement and computational modelling are required to probe this mechanism. We intend on performing identical measurements on gold nanowires (AuNWs) that have the same pentagonally twinned structure as AgNWs. As well as AuNWs, copper nanowires (CuNWs) are an ideal candidate for analysis using this technique, mainly due to their application in microelectronics. These experiments will be performed as part of future work.

5.3 Conclusion

In conclusion, individual Ag NW's were elastically loaded multiple times, at their centre point, under increasing current densities. The Young's modulus, E, displayed a square dependence with increasing current density, j. A greater than two fold increase in modulus was observed at the maximum current density applied. The stiffening effect was not observed under the same measurement on NiNWs, which may be due to differences in the NW crystallographic structure. It was also observed that single NWs could support current densities > 10^9 A/m^2, for prolonged periods of time (>20 *mins*), showing no fatigue or ill effects from heating.

The mechanism involved in the stiffening mechanism is not understood and requires further experimentation and computational modelling. In order to verify the results we intend in performing a similar type of measurement using an AFM based nanoindentation method.

This type of nanoscale measurement has not been presented before, mainly due to the difficulty in performing the measurement. As such, the results presented herein are of major importance in understanding the fundamental properties of metal NWs, and their implementation into functional devices such as interconnects and NEMS. Indeed, we have shown that AgNWs with a pentagonally twinned crystal structure can be mechanically controlled by controlling the magnitude of current density passing through them.

5.4 References

1. Hall, H. H. , J. Bardeen, and G. L. Pearson, *The Effects of Pressure and Temperature on the Resistance of p-n Junctions in Germanium.* Physical Review, 1951. **84**(1): p. 129-132.
2. Smith, C. S. , *Piezoresistance Effect in Germanium and Silicon.* Physical Review, 1954. **94**(1): p. 42-49.
3. Welser, J. , J. L. Hoyt, and J. F. Gibbons. *NMOS and PMOS transistors fabricated in strained silicon/relaxed silicon-germanium structures.* in *Electron Devices Meeting, 1992. IEDM '92. Technical Digest. , International.* 1992.
4. Welser, J. , J. L. Hoyt, and J. F. Gibbons, *Electron mobility enhancement in strained-Si n-type metal-oxide-semiconductor field-effect transistors.* Electron Device Letters, IEEE, 1994. **15**(3): p. 100-102.
5. Hashemi, P. , et al. *Electron transport in Gate-All-Around uniaxial tensile strained-Si nanowire n-MOSFETs.* in *Electron Devices Meeting, 2008. IEDM 2008. IEEE International.* 2008.
6. Nguyen, V. H. , et al. , *Performances of Strained Nanowire Devices: Ballistic Versus Scattering-Limited Currents.* Electron Devices, IEEE Transactions on, 2013. **60**(5): p. 1506-1513.
7. Lassagne, B. , et al. , *Coupling Mechanics to Charge Transport in Carbon Nanotube Mechanical Resonators.* Science, 2009. **325**(5944): p. 1107-1110.
8. Hao, P. , Y. Gao, and Y. Zhou, *The effect of electric charge on the mechanical properties of graphene.* Science China Physics, Mechanics and Astronomy, 2013. **56**(6): p. 1148-1156.
9. Schinwald, A. , Chernova, T. , Donaldson, K. , *Use of silver nanowires to determine thresholds for fibre length-dependent pulmonary inflammation and inhibition of macrophage migration in vitro.* Particle and Fibre Toxicology, 2012. **9**(47).
10. Xu, F. and Y. Zhu, *Highly Conductive and Stretchable Silver Nanowire Conductors.* Advanced Materials, 2012. **24**(37): p. 5117-5122.
11. Lee, M. -S. , et al. , *High-Performance, Transparent, and Stretchable Electrodes Using Graphene–Metal Nanowire Hybrid Structures.* Nano Letters, 2013. **13**(6): p. 2814-2821.
12. Akter, T. and W. S. Kim, *Reversibly Stretchable Transparent Conductive Coatings of Spray-Deposited Silver Nanowires.* ACS Applied Materials & Interfaces, 2012. **4**(4): p. 1855-1859.

13. Fangohr, H. , et al. , *Joule heating in nanowires.* Physical Review B, 2011. **84**(5): p. 054437.
14. Eunan, J. M. , N. T. Tchavdar, and D. Daniel, *Current-assisted cooling in atomic wires.* Journal of Physics: Condensed Matter, 2009. **21**(19): p. 195304.
15. Andrew, P. H. , et al. , *Power dissipation in nanoscale conductors: classical, semi-classical and quantum dynamics.* Journal of Physics: Condensed Matter, 2004. **16**(21): p. 3609.
16. Narvaez, G. A. , J. Kim, and J. W. Wilkins, *Effects of morphology on phonons in nanoscopic silver grains.* Physical Review B, 2005. **72**(15): p. 155411.
17. Smith, D. R. F. , F. R. , *Low-Temperature Properties of Silver.* J. Res. Natl. Inst. Stand. Technol. , 1995. **100**(2).

Chapter 6: Conclusion and Future Work

In this thesis we have probed the mechanical and electromechanical properties of individual nanowire systems. The mechanical properties of germanium nanowires between 10 – 80 *nm* in diameter were mechanically tested using the lateral-AFM 3-point bending method. Large scatter in the values of the measured Young's modulus and strength was observed for NWs below 25 *nm* in diameter. In order to probe the scatter in the data an extensive HRTEM study was performed and found the NWs to display a high density of stacking faults and non-uniform oxide thickness along their length. As a result the TEM/AFM based mechanical analysis technique was developed. Individual GeNWs were pinned on a silicon nitride TEM grid and mechanically interrogated using the lateral-AFM 3-point bending method. Subsequently, the NWs were imaged using HRTEM. The atomic structure of the NW, combined with the modulus and strength from the AFM provided insights into the effects of stacking faults on their mechanical properties. As the TEM/AFM technique would not be suitable for electromechanical measurements, a "pulley" based mechanical loading system using an AFM tip was devised to measure the uniaxial deformation of individual GeNWs. Although we demonstrated the ability of an individual GeNW to slide around a support pulley, it was not suitable for electromechanical measurements as the support-pulley/NW contact resistance increased with the applied load, as well as, limitations related to the NW dimensions (must be > 33 *nm* in radius) and consequent surface adhesion. As such a 4-point electrical measurement coupled with the lateral-AFM 3-point bending method was devised to measure the electromechanical properties of GeNWs. However, its implementation was limited by the high resistance of the un-doped NWs and the inability to measure small resistance changes (noise over tens of $M\Omega$) due to the very small currents involved. In light of this we instead measured the electromechanical properties of metallic NWs as the measured voltage and current were $x10^3$ larger than that of semiconducting NWs, resulting in routine resistance measurement sensitivity of 0.01 Ω.

The dependence of nanowires resistance and resistivity as a function of $\Delta z/L$ was shown for pentagonal AgNWs between 50 – 90 *nm* in diameter, comparing characteristics with the same measurement on NiNWs. We have developed a generalised model to describe the relationship between the changes in resistance and resistivity for an elastic nanowire under strain. We found that individual AgNW resistance increases with $\Delta z/L$, by up to 2.3% at 1.1% strain. The GF for individual AgNW was found to be between 1.17 – 2.19, comparable to that of bulk metals, and with the value of GF found for NiNWs (1.60-1.64), displaying no obvious dependence on nanowire dimensions. A novel electromechanical method for measuring the Poisson's ratio of nanoentities has been established. Using this method we found the Poisson's ratio for Ag NW to lie between 0.05 – 0.54, displaying large deviations from the bulk value. The value of Poisson's ratio for individual NiNWs was found to be comparable to the bulk value. The values for Poisson's ratio and gauge factor were found to be independent of current density. We have shown the values for Poisson's ratio and the *GF* are reproducible under repeated interrogation on individual Ag NWs, showing the robustness of the method. Moreover, we have displayed the importance of measuring the full range of mechanical properties of each nanowire, as properties such as Poisson's ratio are generally assumed that of the bulk value and we have shown that single crystal nanowires can deviate substantially from the bulk value.

The Young's modulus of individual AgNWs was measured as a function of increasing current densities. The Young's modulus, E, displayed a non-linear dependence with increasing current density, j, although the exact mechanism is not known. A greater than two fold increase in modulus was observed at the maximum applied current density. The stiffening effect was not observed under the same measurement on NiNWs, which may be due to differences in the NW crystallographic structure. It was also observed that single NWs could support current densities > $10^9\ A/m^2$, for prolonged periods of time (>20 *mins*), showing no fatigue or ill effects from heating.

These types of nanoscale measurements have not been presented before, mainly due to the difficulty in nanomaterial placement and measurement. As such, the results presented herein are a major step forward in understanding the fundamental properties of metal NWs, and their implementation into functional

devices such as interconnects and NEMS. Indeed, we have shown that the particular crystal structure of the nanowire is critical in controlling electromechanical properties.

This work will be continued in several respects. Having established a collaboration with Prof. Stefano Sanvito within CRANN, Density Function Theory (DFT) calculations will be performed to probe the origins of the observed current induced stiffening in AgNWs. To date, DFT calculations have shown axial compression along the length of the NW resulting from bond length shortening at the twinned planes, the shortened bonds denoted by the grey links in figure 1 (a). From figure 1 (a) it is also clear that bond length shortening around the core of the NW results in a radial core compression coupled with induced surface tension.

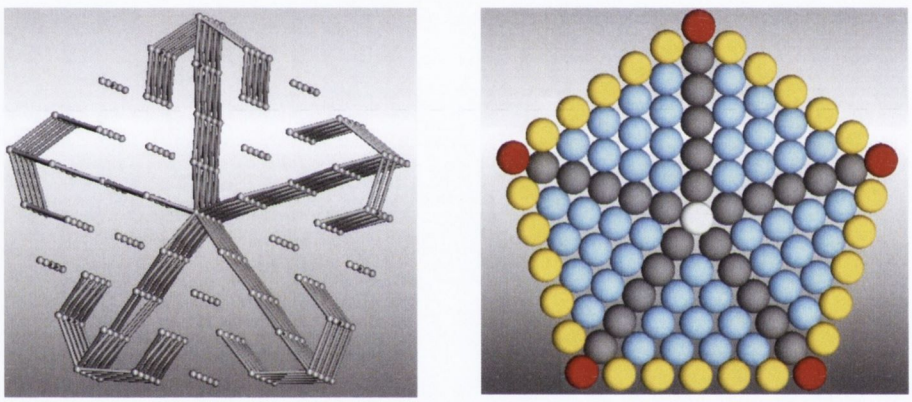

(a) (b)

Figure 1: DFT calculations on an AgNW cross section. (a) Shows the shortest bonds in the system leading to axial and radial compression. (b) Shows the density of states and charge density. The red area shows the greatest charge density and the blue areas the least.

Figure 1 (b) shows the distribution of the density of states across the NW cross section. Using DFT it was found that the maximum charge density resides at the corner atoms of the 5-fold symmetric structure, denoted by the red circles in figure 1 (b). The pentagonal surfaces and twinned planes displayed the next most charge dense region with the blue area showing the least charge rich area. Hence, favourable transport occurs along these select regions in the structure. Further calculations will be performed in the future. To complement the DFT calculations further experimentation will be performed on pentagonally twinned gold nanowires by a continuing PhD student.

In addition to current induced stiffening effects in NWs, the strain dependent electrical properties of individual NW junctions will be investigated. In this project an individual NW junction will be suspended above a pre-fabricated trench and contacted with four electrodes. The junction will be strained using an AFM tip whilst simultaneously measuring the change in transport characteristics. Figure 2 (a) shows a schematic of the experimental setup. An AFM image of a AgNW suspended junction device is shown in figure 2 (b). Preliminary results have shown the viability of the experiments.

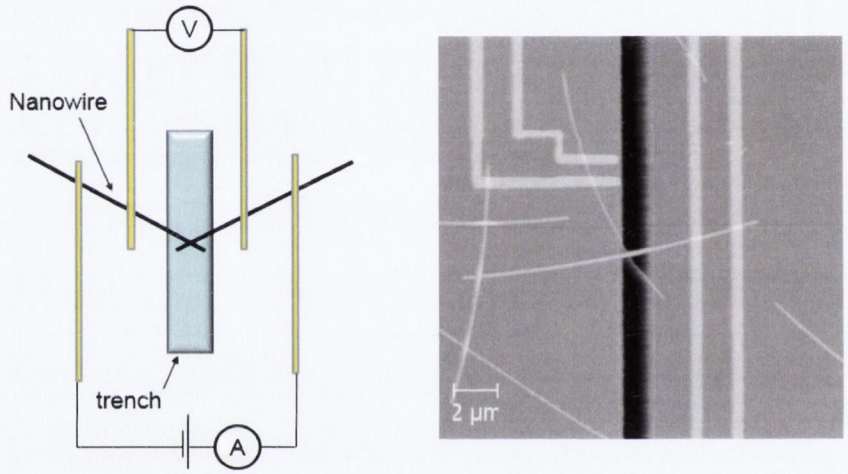

(a) (b)

Figure 2: (a) Schematic of an individual suspended NW junction contacted with four electrodes. (b) AFM image of a AgNW suspended junction contacted with four lithographically defined electrodes.

Using the techniques developed throughout this thesis and monitoring such effects of individual NW junctions will, for the first time, give a valuable insight into the fundamental mechanisms that govern flexible, transparent, conductive nanowire electronics.

List of publications

Soon Jung Jung, Tarek Lutz, Alan P. Bell, Eoin K. McCarthy, John J. Boland, *"Free-Standing, Single-Crystal Cu3Si Nanowires"*, Crystal Growth & Design, **2012**, 12 (6).

Peter N. Nirmalraj, Allen T. Bellew, Alan P. Bell, Jessamyn A. Fairfield, Eoin K. McCarthy *et al*, *"Manipulating Connectivity and Electrical Conductivity in Metallic Nanowire Networks"*, Nanoletters, **2012**, 12 (11).

Eoin K. McCarthy, Allen T. Bellew, John E. Sader, John J. Boland, *Poisson's ratio of individual Nanowires*, Nature Materials, under review, **2014**.

Eoin K. McCarthy, John E. Sader, John J. Boland, *Current Induced Stiffening in Pentagonally Twinned Silver Nanowires*, UK & Ireland patent filed (GB1320028.2), **2013.**

Allen T. Bellew, Alan P. Bell, Eoin K. McCarthy, Jessamyn A. Fairfield, John J. Boland, *Programmable Nanowire Networks: Transparent Memory Applications*, Nanoletters-under review, **2013**.

Appendices

Mathematical models

Young's modulus determination from the generalised model

Young's modulus is obtained normally from a measurement of the beam displacement as a function of the applied load. For a clamped-clamped beam used here, the resulting curve is described by the following well-known equation;

$$F_{center} = \frac{192EI}{L^3} \Delta z_{center} \tag{1}$$

Where F_{center} is the applied force, E is the Young's modulus, I is the areal moment of inertia ($I=\pi r^4/4$), L is the beam length and Δz is the beam displacement from the normal axis. Importantly, this equation predicts a linear relationship between the applied load and the resultant displacement, requiring that measurements also exhibit this property. However, as the beam is displaced, an axial tensile force is inherently induced due to the stretching of the beam. This force affects the total stress experienced by the beam, leading to an enhancement of its rigidity as the beam is loaded causing non-linearities in the measured force-displacement curves.

To begin we note that the governing beam equation that accounts for the effects on in plane forces is given by;

$$EI\frac{d^4w}{dx^4} - T\frac{d^2w}{dx^2} = F_{center}\delta(x - \tfrac{L}{2}) \tag{2}$$

Where w is the deflection of the beam, x is the spatial coordinate along the beam length, T is the tension along the beam, and δ is the Dirac delta function. Note that $\Delta z_{center} = w(L/2)$. The tension, T, is determined from the strain along the axis of the beam, and is given by;

$$T = \frac{EA}{2L}\int_0^L \left(\frac{dw}{dx}\right)^2 dx \tag{3}$$

Equations 2 and 3 are solved according to the usual clamped boundary conditions at both ends of the beam. i.e;

$$w = \frac{dw}{dx} = 0 \qquad \text{at } x = 0 \text{ and } L \tag{4}$$

Solving equations 2 - 4 gives the required solution where;

$$F_{center} = \frac{192\,E\,I}{L^3} f(\alpha) \Delta z_{center} \tag{5}$$

Where,

$$f(\alpha) = \frac{\alpha}{48 - \dfrac{192 \tanh(\sqrt{\alpha}/4)}{\sqrt{\alpha}}} \tag{6}$$

Where α is related to the maximum deflection Δz_{center} by the following transcendental equation;

$$\frac{\alpha \cosh^2(\sqrt{\alpha}/4)}{2 + \cosh(\sqrt{\alpha}/2) - 6\dfrac{\sinh(\sqrt{\alpha}/2)}{\sqrt{\alpha}}} \left(1 - 4\frac{\tanh(\sqrt{\alpha}/4)}{\sqrt{\alpha}}\right)^2 = \Delta z_{center}^2 \left(\frac{A}{I}\right) \tag{7}$$

We note that if $f(\alpha) \geq 1$ so that inclusion of the tensile force increases the effective rigidity of the beam. Also, α is related to the tension in the beam by;

$$\alpha = \frac{T L^2}{E I}$$

and is the ratio of axial stresses to due extension and bending.

While equations 5-7 present an exact analytical solution, it is complex in nature, requiring the numerical solution of a transcendental equation. To overcome this limitation, we note that the solution to equation 7 possesses the following asymptotic solutions;

$$\alpha = \begin{cases} \frac{12}{5}\varepsilon - \frac{3}{875}\varepsilon^2 & , \quad \varepsilon \to 0 \\ 2\varepsilon & , \quad \varepsilon \to \infty \end{cases} \tag{8}$$

Where,

$$\varepsilon = \Delta z_{center}^2 \left(\frac{A}{I}\right) \tag{9}$$

An appropriate and explicit expression for α is then obtained by constructing a Padé approximate using equation 8 i.e.

$$\alpha = \frac{6\varepsilon(140+\varepsilon)}{350+3\varepsilon} \tag{10}$$

which exhibits a maximum error of only 2.1% over the entire range of. Equations 5, 6, and 10 give the generalized form we seek and enable the applied force to be determined for any beam displacement.

Equation 9 indicates that the solution presented in equation 1 is valid provided the displacement is less than the radius of the beam. As the displacement is increases to a value greater than the beam radius, the solution becomes progressively more non-linear with respect to the displacement, leading finally to a cubic dependence on displacement. Thus, an approximate solution can be obtained by superimposing the small and large deflection limits, i.e;

$$F_{center} = \frac{192\,E\,I}{L^3}\Delta z_{center}\left(1 + \frac{A}{24\,I}\Delta z_{center}^2\right) \tag{11}$$

a result that exhibits a maximum error of 18%.

Important notes:

(1) Beam theory is used to analyse these measurements. This inherently assumes that the stresses are uniaxial and hence that the beam is much longer than it is wide. This restriction must be reflected in the experimental set up. Failure to comply can result in complex stress distributions in the rod, leading to failure of the theoretical framework.

(2) The induced in-plane tensile stress also has obvious implications to the determination of the maximum tensile stress, the standard formula for which only assumes that bending, and not stretching, is occurring.

(3) To determine maximum tensile strength, such tensile stretching forces must be included!

Relationship between Resistance and Resistivity Changes in a Nanowire under Normal Loading;

This model was developed in collaboration with Prof. John E. Sader, University of Melbourne. Essentially, the changes in the NW volume during deformation; increases in length and decreases in cross sectional area both contribute to an increase in the NW resistance. We start firstly by considering the contribution due to bending according to classical Euler-Bernoulli beam theory- this applies to high aspect ratio NW. All strain components vary linearly with z, the coordinate normal to the load direction. These do not contribute to the relationship between the measured net change in R and ρ because they balance symmetrically across the thickness. Their total average effect over the beam volume is zero, due to their

linear dependence on z. Bending by definition does not change the volume of a beam. However, shear deformation will be present for a beam of finite thickness-to-length ratio, and is expected to yield a non-zero contribution. This will induce a net strain of $\left(\left[\frac{h}{L}\right]^4 \Delta z/h\right)$, where Δz is the beam displacement, h is the thickness and L is the length, which for a long and narrow beam will be smaller than any contribution due to stretching.

We now consider the effect due to stretching. As the beam deflects normal to its long axis, strain develops along the beam due to stretching:

$$e_{xx} = \frac{1}{2L}\int_0^L \left(\frac{dw}{dx}\right)^2 dx \qquad (1)$$

where w is the deflection normal to the beam axis. This induces strains in two orthogonal directions:

$$e_{yy} = e_{zz} = -\nu e_{xx} \qquad (2)$$

where ν is Poisson's ratio.

It was shown by Ngo et al[1] in 2006 that the relationship between the induced uniaxial tensile force, T, due to stretching and the centre beam deflection, Δz_{centre}, is well approximated by:

$$\frac{TL^2}{EI} = \frac{6\varepsilon(140+\varepsilon)}{250+3\varepsilon}, \qquad (3)$$

where

$$\varepsilon = \Delta z^2\left(\frac{A}{I}\right), \qquad (4)$$

and I is the areal moment of inertia of the cross section, and A is its area.

From Hooke's law, it follows that the strain along the beam axis is given by:

$$e_{xx} = \left(\frac{I}{AL^2}\right)\frac{6\varepsilon(140+\varepsilon)}{250+3\varepsilon} \qquad (5)$$

Equations (2) and (5) completely describe the strain tensor in the beam as all other strain components are zero.

The resistance, R, is related to the resistivity, ρ, by

$$R = \frac{\rho L}{A} \tag{6}$$

It directly follows that the relationship between the change in resistance, ΔR, and the change is resistivity, Δρ, is

$$\frac{\Delta R}{R} = \frac{\Delta \rho}{\rho} + \frac{\Delta L}{L} - \frac{\Delta A}{A} \tag{7}$$

This can be written in terms of the strain tensor components:

$$\frac{\Delta \rho}{\rho} = \frac{\Delta R}{R} - e_{xx} + e_{yy} + e_{zz} \tag{8}$$

Substituting equations (2) and (5) into equation (8) results in:

$$\frac{\Delta \rho}{\rho} = \frac{\Delta R}{R} - (1+2\nu)\left(\frac{I}{AL^2}\right)\frac{6\varepsilon(140+\varepsilon)}{240+3\varepsilon} \tag{9}$$

Equation (9) allows the relative change in resistivity, Δρ/ρ, to be determined from the measured change in resistance, ΔR/R, the centre displacement and the beam dimensions. The equation also directly relates ΔR/R to the strain term. Equation (9) is the general equation that describes the beam under arbitrary displacement conditions. If we consider the case where Δz_{centre} is much smaller than the beam radius, then equation (9) simplifies:

$$\frac{\Delta \rho}{\rho} = \frac{\Delta R}{R} - \frac{12(1+2\nu)}{5}\left(\frac{\Delta z_{centre}}{L}\right)^2 \tag{10}$$

Thus, the resistance and resistivity are related by the square of the beam displacement. If Δz_{centre} is greater than the beam radius, i.e. in the case of large beam deflection, we again obtain a quadratic dependence with strain, albeit with a slightly different coefficient:

$$\frac{\Delta\rho}{\rho} = \frac{\Delta R}{R} - 2(1+2\nu)\left(\frac{\Delta z_{centre}}{L}\right)^2 \qquad (11)$$

Shear deformation induces a correction of higher order in the thickness-to-length ratio correction, however, this should only be observable at very small deflections, i.e.

$$\frac{\Delta z_{centre}}{a} < \left(\frac{a}{L}\right)^2 \qquad (12)$$

Measurements are performed well away from this limit, so shear deformation effects does not affect the theory.

Appendix references;

1. Ngo, L.T., et al., *Ultimate-Strength Germanium Nanowires.* Nano Letters, 2006. **6**(12): p. 2964-2968.